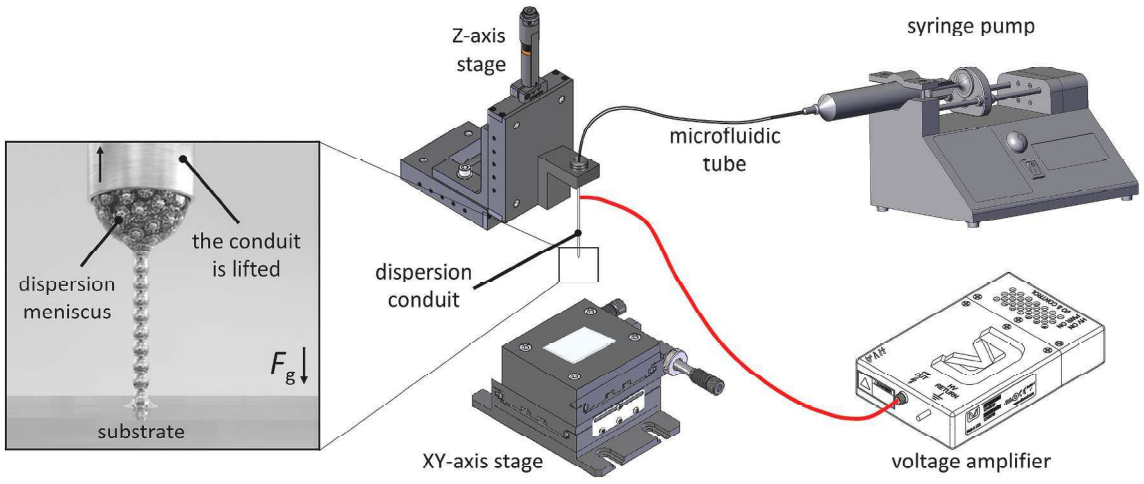

Fig. 1. Schematic diagram of the experimental setup, which included a syringe pump for dosing dispersion into the dispersion conduit, a motorized stage for vertical translation of the conduit, and a manual stage for XY directional translation of a substrate. The high-voltage bipolar amplifier supplied a signal to either the conductive substrate or the conductive dispersion conduit. The meniscus with a slightly truncated semicircular shape was achieved through precise dosing of the dispersion. In all experiments, the substrate surface was oriented perpendicular to the vertically mounted conduit.

2.2. Materials and sample preparation

Silicone oils (Rhodorsil Oils 47; with different viscosities in the range of 10–1000 mPa·s at 25°C, density 0.96–0.97 g·cm^{-3} at 25°C, electrical conductivity of 5–10 pS·m^{-1}, and relative permittivity 2.8) were used to prepare dispersions with various microparticles. Several types of microparticles were employed: solder microparticles of $Sn_{63}Pb_{37}$ and SAC305 with diameters of 100, 150, 200, 250, 300 and 400 μm (±3% tolerance), with densities 8.4 g·cm^{-3} for $Sn_{63}Pb_{37}$ and 7.4 g·cm^{-3} for SAC305 (sourced from PMTC, Taiwan, *via* Reball, Poland); stainless-steel particles with a diameter of 200 μm (±10% tolerance) and a density of 7.8 g·cm^{-3} (Cospheric LLC, USA, SSMMS-7.8); and Ag-coated glass particles with a diameter of 100 μm (±15% tolerance) and a density of 2.5 g·cm^{-3} (Cospheric LLC, USA, SLGMS-AG-2.5).

2.3. Numerical simulations

To estimate the attractive force (F_e) between a charged spherical particle and the surface of a flat substrate, we employed the *Electrostatics* interface of COMSOL Multiphysics using a two-dimensional axisymmetric model. To reconstruct the full three-dimensional system, the model geometry was revolved 360° around the vertical axis. The geometry, shown in Fig. 4a, includes a section of the conduit, a hemispherical volume that approximates the dispersion meniscus, and a significantly smaller sphere positioned partially on the edge of the hemisphere—mimicking a microparticle located at the meniscus surface. The surrounding medium was modelled as air with a relative permittivity close to unity, while the flat substrate block was treated as a dielectric with a relative permittivity of 4. In the simulations, the substrate thickness was varied from 0 to 30 mm. A zero-thickness substrate corresponds to a grounded conductor, whereas a 30 mm-thick substrate approximates an ungrounded dielectric with no nearby electrical ground.

A DC electric potential in the range of 1–4 kV was applied to the particle, the hemispherical meniscus, and the conduit. The bottom boundary of the simulation domain was grounded, while the dielectric substrate remained electrically floating. The entire domain was enclosed within a thin Infinite Element Domain to approximate open boundary conditions. A stationary study was performed, with zero-charge (Neumann) boundary conditions to the outer edges.

The attractive force F_e acting on the particle was calculated by integrating the z-component of the Maxwell Stress Tensor over the particle surface. This procedure allowed for a precise determination of the net force as a function of the particle–substrate separation h (ranging from 1 to 3000 μm) and the applied voltage. Based on the simulation results, the distance h corresponding to a constant target force was interpolated for each voltage, which enabled the construction of distance–voltage curves at fixed force thresholds.

2.4. Experimental configuration and protocol for particle chain formation

Preparation for the particle chain formation experiment involved several steps: lowering the conduit toward the substrate (Fig. 2a); forming a meniscus of dispersed microparticles at the conduit outlet (Fig. 2b); and applying a high voltage to establish a connection between the dispersion meniscus and the substrate (Fig. 2c). Once this connection was achieved, the actual experiment began: the desired voltage was set, and the conduit was vertically translated at a controlled speed. During meniscus formation, we aimed to achieve a consistent and well-controlled shape (Fig. 2b) to ensure reproducible initial conditions. This was accomplished using a precision syringe pump to regulate the flow rate, while monitoring the meniscus at the capillary outlet with a digital microscope. The meniscus typically developed over several seconds, and once it reached the desired geometry, the pump was stopped.

To identify optimal experimental conditions, we conducted preliminary tests addressing the influence of ambient parameters, the optimal meniscus shape and liquid volume, as well as the electrical parameters required to establish a connection between the dispersion meniscus and the substrate. The results of these tests are presented in the first part of the Results section.

3. Results and discussion

3.1. Force balance during chain initiation

To understand the fundamental conditions required to initiate chain formation—that is, to establish a connection between the dispersion meniscus and the substrate (see Fig. 2c)—we begin by analysing the force balance acting on the first particle at the meniscus. Two types of capillary bridges are involved. The first, referred to as *Type I*, forms between an individual particle and the liquid–air interface (*i.e.*, the meniscus). This capillary bridge emerges when a particle is partially withdrawn from the liquid, generating a restoring capillary force (F_{sp}) directed back toward the meniscus. This force effectively traps the particle at the interface. As long as the net downward force—comprising gravity (F_g) and buoyancy (F_g)—remains smaller than the capillary

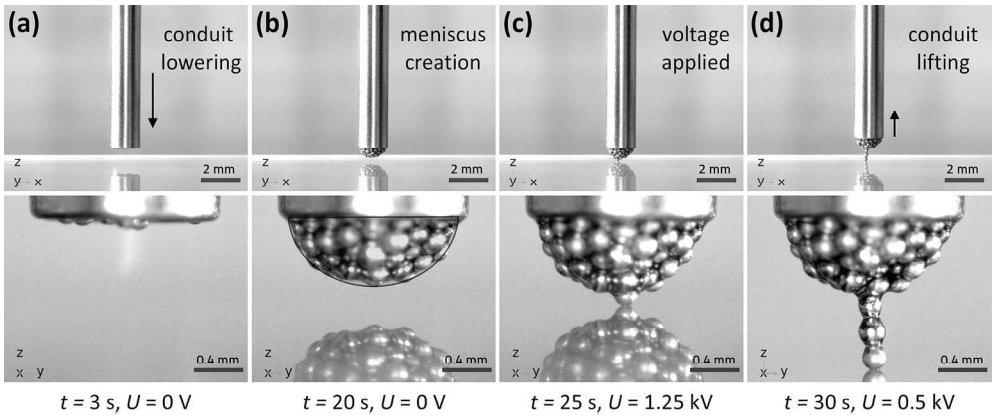

Fig. 2. Illustration of the preparation and initiation process for the particle chain experiment. **(a)** Lowering the conduit toward the substrate. **(b)** Creating a meniscus of dispersed microparticles at the capillary outlet by dispensing the dispersion at a controlled flow rate (here, 0.01 μL/s). The meniscus is shaped into a truncated semicircle, as indicated by the overlaid contour. **(c)** Applying a brief voltage pulse (here, 1.25 kV) to establish a connection between the dispersion meniscus and the substrate, pulling a single particle from the meniscus to initiate contact with the substrate surface. **(d)** Adjusting the voltage to the desired value (here, 0.5 kV) and raising the conduit to initiate the chain formation. See also the corresponding **Movie S1**, which demonstrates this process as well as an alternative approach to the preparation and initiation of the particle chain experiment.

force, the particle remains confined at the meniscus (Fig. 3a). Upon application of additional energy in the form of an electric field, the capillary force barrier can be overcome, allowing the bridge to stretch (Fig. 3b) and eventually transition into a *Type II* interparticle bridge (Fig. 3c), enabling detachment and chain formation.

The capillary restoring force depends on the geometry of the meniscus and the particle's local environment. While analytical estimates exist for isolated particles at planar interfaces [15], the situation is more complex in the presence of neighbouring particles embedded within a curved meniscus. However, to simplify the system in our analysis, we will describe the capillary force acting on a single spherical particle, ignoring multi-particle interactions. Generally, for a spherical particle in a perfectly wetting liquid (a reasonable assumption for the nonpolar liquids and particles used in this study), the capillary force scales approximately linearly with the particle radius r, according to $F_{sp} \propto 2\pi r\gamma$ where γ is the liquid's surface tension. These *Type I* bridges also promote axial stacking by directing incoming particles toward the centre of the meniscus. As additional particles are introduced above a partially extracted one, they experience a net capillary force that drives them toward the centre of the meniscus. This force can be decomposed into two components: a vertical ($F_{\gamma|y}$ $2\pi r\gamma\cos\alpha$) and horizontal ($F_{\gamma|x}$ $2\pi r\gamma\sin\alpha$) components, where α is the inclination angle of the interface. The horizontal component favours one-by-one vertical alignment and suppresses lateral aggregation [17].

As the particle is extracted from the meniscus, a structural transition occurs. The *Type I* capillary bridge (between the particle and the liquid–air interface) undergoes a transition into an interparticle capillary bridge, referred to here as a *Type II* bridge (see Fig. 3c). Notably, the presence of *Type II* capillary bridges enables the particle chain to remain mechanically stable even after the electric field is switched off. Moreover, these *Type II* bridges provide attractive interactions between neighbouring microparticles, enabling the chain to exhibit elastic behaviour under low levels of compressive strain. These features will be discussed in more detail in later sections.

Cohesive interactions within the meniscus: In addition to capillary forces, weak cohesive interactions between neighbouring particles may arise from van der Waals forces, particularly in densely packed regions of the meniscus. Although such forces are always present between neutral bodies, their magnitude depends on particle size, surface separation, and the dielectric properties of the medium. In nonpolar liquids, such as the oils used in our experiments, these interactions are significantly attenuated by the interfacial layer that limits close contact

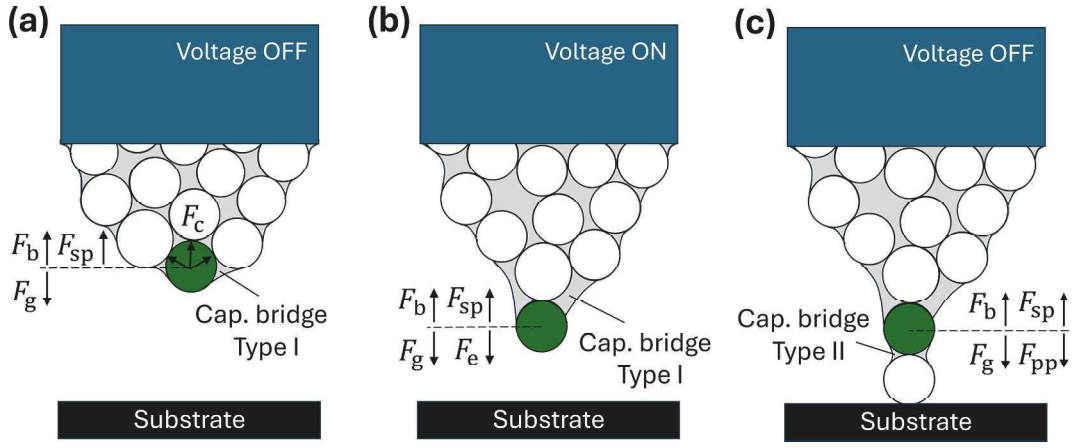

Fig. 3. Schematic illustration of the forces acting on a microparticle during the initiation of chain formation. (**a**) A particle partially immersed in the dispersion meniscus forms a *Type I* capillary bridge with the liquid–air interface. The particle is stabilized by a capillary restoring force (F_{sp}), that counteracts gravity (F_g) and may be assisted by buoyancy (F_b) and weak cohesive forces (F_c) arising from van der Waals interactions between closely packed neighbouring particles within the meniscus. (**b**) After voltage application, (F_e) acts downward, opposing the capillary restoring force and promoting the particle's extraction from the meniscus. (**c**) As the particle detaches, the *Type I* bridge elongates and transforms into a *Type II* bridge, stabilizing the growing chain.

between solid surfaces.

As illustrated in Fig. 3a (see F_c), van der Waals forces may still provide a minor cohesive contribution between neighbouring particles, especially in densely packed configurations. These are genuine cohesive forces—distinct from attractive forces induced by external electric fields. The van der Waals force between two identical spherical particles scales approximately linearly with particle radius r assuming constant surface separation. For a typical Hamaker constant $A \approx 10^{-20}$ J and surface separation $D \approx 2$ nm, the resulting cohesive force is on the order of 2 nN for particles with $r = 10$ μm, increasing to approximately 40 nN for $r = 200$ μm. For comparison, the gravitational force acting on a metal sphere of radius $r = 10$ μm is approximately $F_g \approx 3$ nN, while for $r = 200$ μm is approximately $F_g \approx 1.3$ μN. While negligible for larger particles, van der Waals cohesion may become relevant below 20 μm, where gravitational forces decrease rapidly and surface effects dominate—potentially promoting aggregation or hindering particle separation.

Electric forces driving extraction: When voltage is applied to the conduit and a meniscus of the conductive microparticle dispersion forms at its tip (Fig. 3b), the following physical scenario emerges. The bottom particle, in contact with other conductive microparticles electrically connected to the conduit, assumes nearly the same electric potential. As it approaches the substrate—whether conductive or insulating—an electric attraction arises. For conductive substrates, this attraction arises from image charge formation. For grounded conductors, classical image charges can be assumed, leading to a force given by: $F_{e-image} = q^2/(16\pi\varepsilon_0 s^2)$, where $q = 4\pi\varepsilon_0 rU$, is the estimated charge of a conductive spherical particle held at potential U, and s is the distance from the particle center to the substrate. Substituting this into the expression yields the simplified form $F_{e-image} = \pi\varepsilon_0 r^2 U^2/s^2$. While this analytical model is derived from the image-charge method for point charges and adapted here for a conducting sphere by estimating its surface charge, it does not accurately capture the real configuration of the system. In our experimental setup, the particle is partially immersed in a liquid meniscus and located near the edge of a slightly conical conduit. This geometry, along with the dielectric discontinuities and boundary conditions, significantly alters the field distribution and the resulting force. Therefore, this expression can at best provide a rough order-of-magnitude estimate. To evaluate the electrostatic force under realistic experimental conditions, we performed numerical simulations that go beyond the simplified image-charge model and capture the influence of the experimental geometry and dielectric environment.

Fig. 4a shows the electric potential distribution and the simulated geometry, which closely mimics the experimental configuration. The model is based on a finite-element solution of Laplace's equation applied to a system composed of a conductive microparticle placed near the interface between air and a glass substrate, with relative permittivities $\varepsilon_1 \approx 1$ and $\varepsilon_2 = 4$, respectively. The particle is positioned partially inside a hemispherical cavity, serving as a simplified approximation of the meniscus geometry—representing the experimental condition where particles protrude from a liquid meniscus at the capillary tip. The field is computed assuming the conduit, meniscus, and particle are held at a potential U, while the bottom boundary of the domain is grounded. The lower region consists of a dielectric slab of thickness d, which remains electrically neutral and models the glass substrate used in experiments. The simulation yields both the spatial distribution of the electric field and the resulting electrostatic force acting on the particle as a function of its distance h above the substrate surface.

To explore the influence of substrate properties, we varied its thickness d from 30 mm down to 0 mm, thereby spanning a range from a configuration that approximates an ungrounded dielectric substrate (*e.g.*, glass or plastic), to the limiting case of a grounded conductive substrate. Fig. 4b shows a set of simulated force–distance curves for a fixed applied voltage $U = 2$ kV, depicting the vertical component of the electrical force acting on the particle toward the substrate for various values of d.

The results indicate that the attractive force decreases with increasing distance h, approximately following an inverse proportionality in the presented ranges of h. The magnitude of the force is strongly affected by the substrate thickness. For $d \to 0$ mm, corresponding to a conductive substrate, the force is significantly enhanced—particularly at short distances—due to the strong image-charge-like polarization of the substrate. In contrast, when d is large (*e.g.*, 30 mm), the field lines are less focused near the substrate surface, leading to a much weaker attractive force.

In Fig. 4b, two horizontal lines were added at force values of 5 μN and 12 μN. These values serve as reference capillary forces acting on a single 200-μm particle at the air–silicone oil interface. Specifically, the 12 μN force reflects the typical capillary force for a single particle in this system, while the 5 μN force approximates the reduced capillary force in

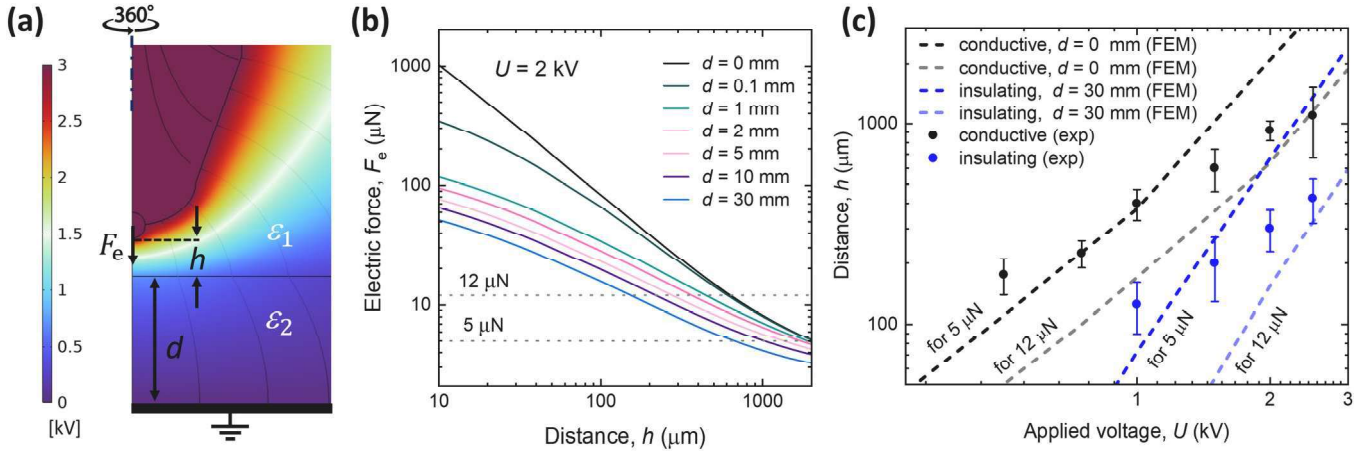

Fig. 4. Numerical simulation and experimental validation of the electrostatic interaction between a charged spherical particle and a flat substrate. **(a)** Geometry of the 2D axisymmetric model used in COMSOL. The upper domain ($\varepsilon_1 = 1$) represents air, and the lower domain ($\varepsilon_2 = 4$) simulates a dielectric slab (glass) of thickness d. The gap between the particle and the dielectric is denoted as h. The system is revolved 360° to reconstruct the 3D configuration. **(b)** Simulated electric force F_e as a function of separation distance h for various dielectric thicknesses d at a fixed potential $U = 2$ kV. The dashed lines at 5 μN and 20 μN mark reference levels corresponding to typical capillary forces at the air–silicone oil interface: for a single particle (~10 μN) and for a particle surrounded by neighbours (~5 μN). **(c)** Distance h at which the attractive electric force equals 5 μN or 12 μN, plotted against the applied voltage U for $d = 0$ mm and $d = 30$ mm. Experimental data points (black for conductive substrates and blue for insulating substrates) indicate the critical distance at which the abrupt extraction of the bottom particle from the meniscus and its contact with the substrate occurred.

a dense arrangement of neighbouring particles. This reduction arises because the local meniscus geometry and capillary interactions are significantly altered in such configurations, leading to a smaller resulting capillary force acting on any given particle, as demonstrated in [40]. For these two reference forces, the plots in Fig. 4c were prepared, illustrating the critical distances at which the electric force equals the reference capillary forces.

Additionally, Fig. 4c includes experimental data points that show the measured distances h at which abrupt extraction of the bottom particle from the meniscus and its subsequent contact with the substrate occurred for various applied voltages. Two series of experiments were performed: one with a conductive substrate (copper) and another with a non-conductive substrate (glass). The results confirm the numerical trends and highlight the critical role of the substrate's electrical properties in enhancing or diminishing the attractive interaction.

Fig. 4 can thus serve as a reference for estimating the threshold voltage required to initiate chain formation, as suggested in Fig. 2c. For example, when a particle with a diameter of 200 μm is located approximately 400 μm above the substrate, the estimated initiation voltage is approximately 1 kV for a grounded conductor, and 2.5 kV for an insulating substrate.

3.2. Meniscus shape and liquid volume

To further understand the parameters affecting extraction, we next investigated how the preparation conditions of the dispersion meniscus could influence chain formation. Our hypothesis was that both the meniscus shape and the amount of dispersing liquid would significantly impact the success rate of particle extraction. To test this, we conducted two sets of experiments.

First, we assessed the effect of liquid content around the particle cluster by conducting tests under three conditions: dry, semi-dry, and wet menisci, as shown in Fig. 5a. For each condition, ten trials were performed using solder particles (200 μm) suspended in oil (150 mPa·s). The results, presented in Fig. 5b, show that the wet meniscus condition yielded the highest success rate (particle structure formed with a minimum 25 particles), particularly at lower voltages.

In the second set of experiments, we investigated the effect of meniscus shape on the extraction process. Three different aspect ratios (h:w) of the meniscus were tested, ranging from a wide, shallow meniscus (h:w = 1:4) to a more symmetric meniscus (h:w = 1:1), as illustrated in Fig. 5c. The corresponding success rates are shown in Fig. 5d, which indicate that at higher voltages, the meniscus shape is less critical than at lower voltages. However, since our experiments span a wide voltage range, the optimal meniscus shape for extraction appears to be a slightly truncated half-sphere, with an h:w ratio of approximately 1:3. Ideally, this ratio should remain within the range of 1:4 to 1:2 for consistent results.

Based on these findings, we will use a meniscus shape with an aspect ratio close to 1:3 and maintain wet conditions in subsequent experiments to optimize extraction repeatability. The wet conditions were defined as having a dispersing liquid content in the range of 35–45% by volume, corresponding to particle volume fractions of 55–65%. This range is close to the practical limits of dense monodisperse dispersions, between random close packing and the theoretical maximum packing of ordered structures.

While a high liquid content in the meniscus facilitates reliable particle detachment and chain formation, it also introduces a risk of surface wetting. If the meniscus approaches the substrate too closely, uncontrolled deposition may occur, potentially causing a significant portion of the dispersion may collapse onto the surface. This failure mode requires restarting the experiment by reforming the meniscus and removing excess material. To avoid such outcomes, it is essential to maintain a safety gap between the bottom of the meniscus and the substrate. Based on our observations, a distance of at least one particle diameter, and preferably two to three, minimizes the risk of wetting while still enabling chain initiation. However, this design choice entails an important trade-off: increasing the separation distance reduces the electric field strength at the substrate, thereby requiring higher applied voltages to initiate particle extraction.

To support the rational design of the extraction system, we refer to the quantitative relationship between initiation voltage and meniscus–substrate distance established through simulations and experiments (Fig. 4). This enables setting safe operating conditions that minimize

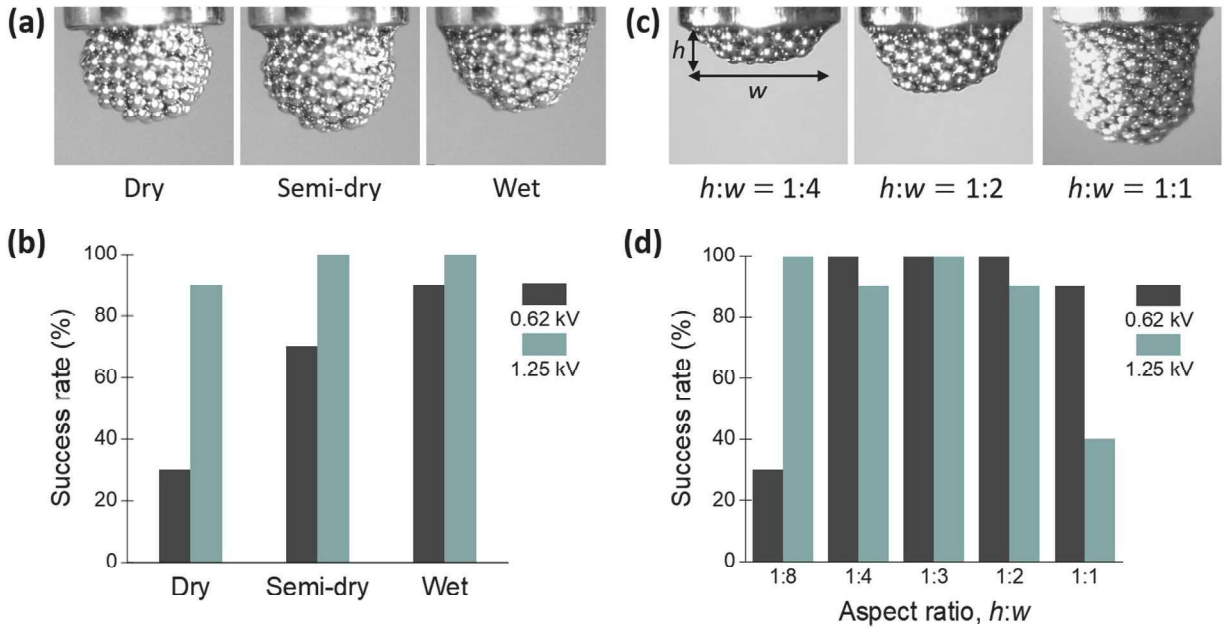

Fig. 5. Influence of meniscus preparation conditions on the success rate of particle extraction. (**a**) Images of dry, semi-dry, and wet meniscus conditions at the conduit outlet. (**b**) Success rates for each meniscus condition (dry, semi-dry, and wet) under applied voltages of 0.62 kV and 1.25 kV, showing higher success with wet conditions. (**c**) Meniscus shapes with different aspect ratios (h:w = 1:4, 1:2, and 1:1) for evaluating the effect of meniscus geometry on extraction success. (**d**) Success rates corresponding to each aspect ratio and voltage condition, indicating that a meniscus with h:w close to 1:3 yields the highest extraction repeatability.

wetting risk without compromising extraction reliability.

3.3. Influence of ambient humidity

During experiments, we observed variability in the chain formation process that could not be fully explained by geometric or electrical parameters alone. We hypothesized that fluctuations in ambient humidity contributed to this inconsistency, as the relative humidity (RH) in the laboratory environment varied between 30% and 55%. To test this hypothesis, we enclosed the critical components of the setup—including the conduit, motorized stages, substrate, and camera—within a sealed glovebag, enabling precise control of the surrounding atmosphere.

We performed a series of tests across a wide humidity range, from 15% to 95% RH. The results showed that chain formation becomes increasingly unreliable above 50% RH, and practically impossible above 55%. Conversely, the process remained stable and repeatable at lower humidity levels, with optimal performance occurring between 15% and 50% RH (see Movie S2). Based on this, all experiments reported in this work were conducted under ambient conditions maintained at 30 ± 10% RH.

3.4. Impact of particle size and voltage on particle chain formation

As the first experiment for particle chain formation, we begin with studies using microparticles with sizes 150 μm, 200 μm, 250 μm, and 300 μm. The choice of the size range is dictated by practical considerations, such as being sufficiently large to allow detailed imaging using a digital microscope, as well as findings from the publications [17,41], which indicate that this size range lies roughly in the middle range of sizes suitable for forming similar structures using the synergistic effects of capillary and electrical interactions.

Fig. 6a illustrates the maximum number of particles forming the chain as a function of the applied electric voltage for solder particles of various sizes. The formation process begins on a non-conductive glass substrate, over 3 cm thick, which rests on the ungrounded metallic surface of the translational stage. This configuration creates a floating substrate system, where neither the glass block nor the metallic stage establishes a direct electrical connection to the ground. This lack of grounding allows the system to operate without a defined reference potential.

It is evident that a threshold voltage is required to initiate chain formation. This requirement arises because gravitational forces alone are insufficient to detach the microparticles from the liquid–air interface; therefore, an external electric field is required to overcome the capillary forces at the liquid meniscus.

The buoyancy force acting on a particle can be expressed as: $F_b = (\rho_{oil} - \rho_{solder})V \cdot g \approx -1$ μN, assuming a particle size of 300 μm and densities of the oil and solder of 970 kg·m^{-3} and 8500 kg·m^{-3}, respectively. The negative buoyancy force confirms that the particle is denser than the oil, causing it to sink naturally under the action of gravity. The capillary force, however, acts to hold the particle at the silicone oil-air interface, representing the primary barrier to detachment. This force is approximated as: $F_{sp} \approx 2\pi r\gamma$, where r is the particle radius and γ is the surface tension of the liquid. Assuming $\gamma = 0.02$N·m^{-1} for silicone oil, and a particle with a radius of 150 μm, the capillary force is calculated as $F_{sp} \approx 19$ μN. This significant force (relative to $|F_b| \approx 1$ μN) highlights the necessity of applying an electric force to overcome it and detach the particle from the liquid surface. This detachment is, in fact, a complex process involving the stretching of the capillary bridge formed between the liquid meniscus and the particle, and its eventual transformation into a capillary bridge between two particles. The detailed dynamics of this transition have been extensively discussed in our previous work [15].

As the voltage increases, longer chains are formed, driven by the enhanced electrical activation of cohesive interactions between particles. The maximum chain length depends on the particle size; for example, 150-μm particles form chains of nearly 70 particles, whereas 300-μm particles reach a maximum of around 20 particles. However, further increases in voltage do not result in longer chains and may even reduce chain length. This reduction is attributed to substrate interaction. As chains grow longer and heavier, maintaining a perfectly vertical alignment becomes increasingly challenging. This misalignment is influenced by several factors: first, it is practically impossible to perfectly align particles one directly above the other; second, the inherent polydispersity in particle sizes and the slight variability in capillary bridge geometry cause deviations from the ideal linear structure, resulting in a gradual tilt of the chain. As the chain becomes heavier, it bends slightly away from the vertical axis, making it easier for the lower portion of the chain to deviate toward the substrate. In this situation, the non-conductive substrate begins to interact with the

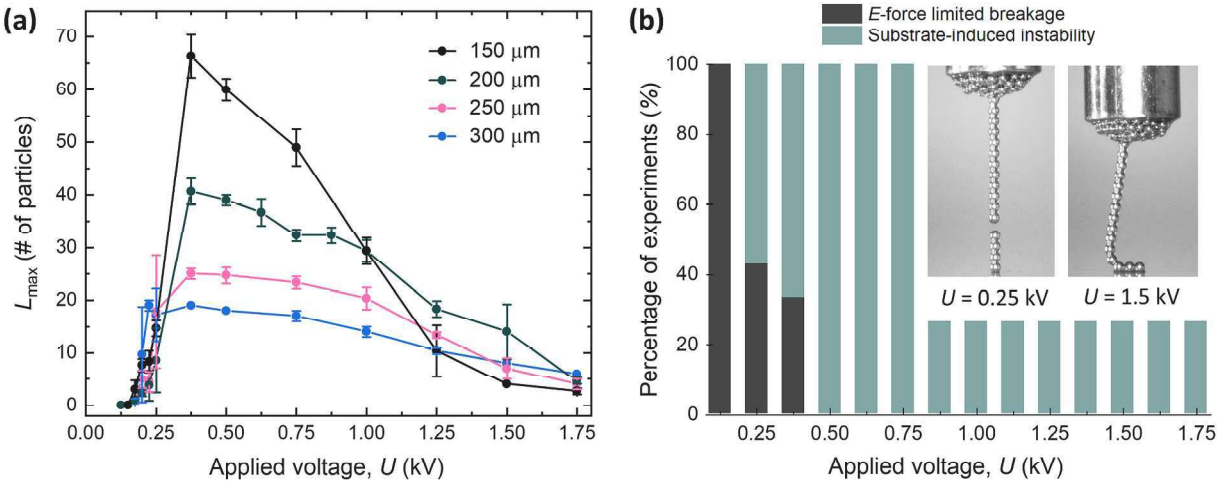

Fig. 6. (**a**) Maximum number of particles forming a chain as a function of applied voltage for solder particles of different sizes. The experiment was conducted using a floating substrate system with a non-conductive glass block resting on an ungrounded metallic stage, eliminating any direct electrical connection to the ground. Smaller particles form longer chains at lower voltages, requiring less force to detach from the liquid meniscus. Electric-force limited breakage occurs only at low voltages (up to 0.4 kV), while at higher voltages, chain length decreases due to substrate-induced instability. Shaded regions indicate variability across experiments. (**b**) Statistical results showing two primary mechanisms limiting the formation of the chain (made of 200-μm solder particles): chain breakage near the meniscus at lower voltages and substrate-induced instability at higher voltages, where the chain unravels onto the substrate. Representative images in the insets further illustrate these scenarios. See also the corresponding **Movie S3.**

particles closest to it. The strongest attractive interaction occurs with the second particle from the substrate, followed by the third, fourth, and so on. If this attractive force is sufficiently strong, the chain 'unravels' onto the substrate. Attempts to lift the conduit with the dispersion meniscus higher result in continued chain formation, but the chain develops in an uncontrolled manner, spreading across the substrate. We define this phenomenon as *substrate-induced instability*, which marks the onset of structural destabilization during chain formation. When the chain is no longer suspended between the initial point on the substrate and the dispersion meniscus but spreads across the substrate, this state is defined as the maximum chain length, and the total number of microparticles is recorded just before this unravelling occurs.

Furthermore, as the voltage increases, the attractive interaction between the chain and the substrate becomes stronger, causing the substrate-induced instability to occur at an earlier stage, when the chain is shorter, thus further limiting the formation of longer chains in these cases. Notably, this effect is more pronounced for smaller particles, as they are easier to extract from the liquid meniscus. Consequently, a smaller magnitude of this attractive interaction is sufficient to induce instability.

Fig. 6b presents statistical data showing the mechanisms that limit chain formation during the experiment with a 200-μm solder particles. The outcomes are categorized into two cases: (i) *electric force-limited breakage*, where the chain breaks due to insufficient electric force; the break typically occurs just below the meniscus or, less frequently, at random points along the chain (as shown in the inset, where the break occurs near the middle); and (ii) *substrate-induced instability*, where the chain unravels upon contact with the substrate. At lower voltages near the threshold, electric force-limited breakage dominates because the electric force is too weak to counteract capillary forces. As the voltage increases, substrate-induced instability becomes the primary limitation, causing the chain to spread uncontrollably onto the substrate. The inset images provide visual examples of both scenarios, illustrating how the chain's behaviour changes with varying voltage conditions (see also the corresponding Movie S3**)**.

3.5. *Critical voltage for substrate-induced instability in inclined particle chains*

The substrate-induced instability occurs when the chain begins to sag. However, this phenomenon can also arise at lower voltages if the straight chain is not perpendicular to the substrate. Fig. 7a presents the results of experiments conducted on chains of equal length (3 mm) formed with different particle sizes (100 μm, 200 μm, and 400 μm). Each chain, initially nearly perpendicular to the substrate surface, was inclined to a specific angle by adjusting the conduit position relative to the substrate. The voltage was then gradually increased (in 50 V steps) until at least two particles were attracted to the substrate. The critical voltage, U_{cr}, marks the onset of this instability. Fig. 7b provides representative images from the experiment. The top row shows chains formed with 200-μm particles, illustrating how the chain makes contact with the substrate at different inclination angles and corresponding critical voltages. The bottom row demonstrates a case where chains with an initial inclination angle of approximately 62° are formed using particles of different sizes. These images highlight how the critical voltage U_{cr} varies depending on the particle size, even for the same inclination angle.

The results indicate that U_{cr} decreases as the inclination angle deviates from 90 °, which is expected since the attractive interaction between the substrate and the chain increases when particles are closer to the substrate surface. Notably, the largest particles (400 μm, pink triangles) exhibit the highest U_{cr} values, whereas the smallest particles (100 μm, black squares) consistently show lower U_{cr} values. A possible explanation for this is that chains formed from larger microparticles are more stable, requiring greater force to bend. Larger microparticles create stronger capillary bridges due to their greater surface area in contact with the liquid. These bridges increase cohesion between particles, making the chain more resistant to deformation. Additionally, the reduced number of connections in chains composed of larger particles enhances their stiffness. Consequently, more force is needed to bend chains composed of larger particles compared to those with smaller particles.

In the log–log plot in Fig. 7a, we marked a line indicating a slope of 2. The intention is not to suggest a specific relationship between U_{cr} and α, but rather to highlight the strong tendency for U_{cr} to decrease as the inclination angle decreases. For a rigid cylinder, this relationship should be weaker. However, the situation here is different. This strong dependence of U_{cr} on the inclination angle α arises from the interplay of electric, gravitational, and capillary forces acting on the flexible chain of

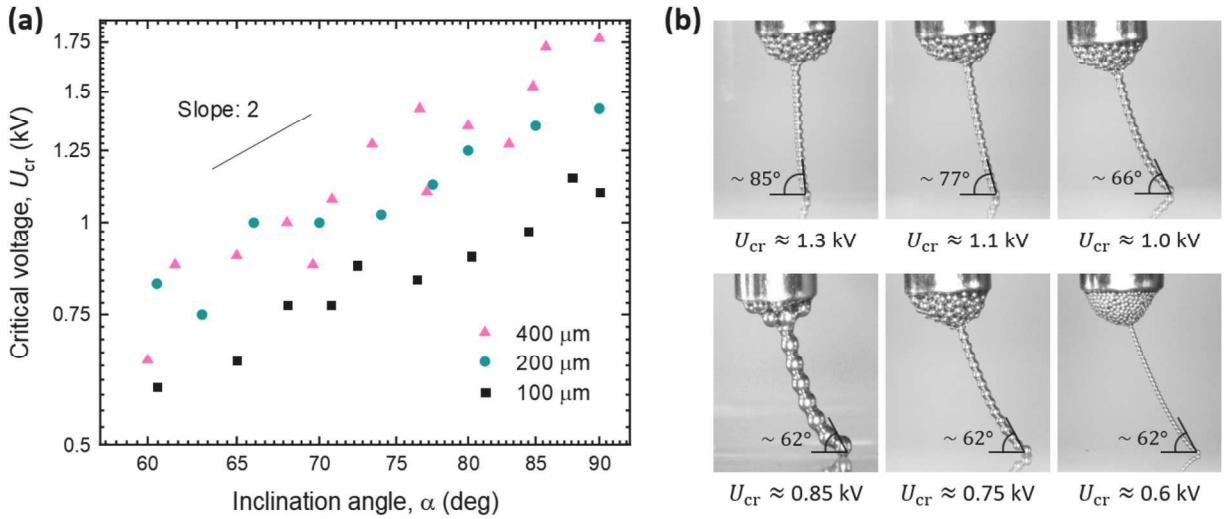

Fig. 7. (**a**) Critical voltage U_{cr} as a function of inclination angle α for chains of different particle sizes. U_{cr} decreases as the inclination angle deviates from 90°, with larger particles requiring higher critical voltages due to stronger attractive forces between particles stemming from capillary bridges and a smaller number of connections affecting the chains stiffness. (**b**) Representative images show chains just before substrate-induced instability occurs. (Top row) For chains made of 200-μm particles, different initial inclination angles require different voltages for instability to occur. (Bottom row) For chains made of different particle sizes at $\alpha \approx 62$ °, smaller particles require progressively lower voltages to contact the substrate. These results highlight the influence of both particle size and inclination angle on substrate-induced instability. See also the corresponding **Movie S4**.

microparticles. When the inclination angle is large, the chain remains more upright, and the gravitational and capillary forces stabilize the structure, requiring a higher electric force — and thus a higher voltage U_{cr} — to pull the chain down to the substrate. As the inclination angle decreases, the lower part of the chain bends closer to the substrate, reducing the distance that the electric force needs to overcome. This geometric change, combined with the flexibility of the chain, allows the microparticles to come into proximity with the substrate more easily, thereby lowering the required voltage to achieve contact. Consequently, the critical voltage U_{cr} decreases significantly with decreasing inclination angle, reflecting the enhanced ease with which the chain can be attracted to the substrate.

3.6. Design implications of substrate geometry and conductivity in chain formation

If a flat substrate induces instability due to attractive interactions with the chain, modifying the substrate's geometry could potentially mitigate this effect. To explore this, we compared a flat substrate with a cylindrical substrate made of similar non-conductive material. The expectation was that a cylindrical substrate—having dimensions comparable to the microparticles (with a diameter 0.75 mm)—would reduce the strength of the attractive interaction, especially at higher applied voltages.

Fig. 8a presents the results of these experiments. The data (black circles) show that chains formed on a cylindrical glass fibre substrate experience weaker substrate-induced interactions, allowing for the formation of longer chains at higher voltages compared to those on a flat substrate (red circles). These findings confirm that altering substrate geometry can effectively reduce substrate-induced instability. A dynamic visualization of this improved chain stability with cylindrical substrates is provided in Movie S5. Furthermore, **Fig. S2** presents the results of an additional experiment designed to further clarify the influence of substrate geometry. In this experiment, a chain of predetermined length was prepared at low voltages, after which the voltage gradually increased until substrate-induced instability occurred. The results clearly show that, across the entire range of chain lengths (from 5 to 38 microparticles), higher voltages are required to induce instability on the cylindrical substrate compared to the flat substrate.

In the next experiment, we used a conductive substrate. Assuming that the chain itself is conductive, the same electrical signal should be present on the substrate. In such a setup, no interaction is expected between the formed chain and the substrate, meaning substrate-induced instability should not occur. And indeed, this is exactly what we observed. The results, shown in Fig. 8a (blue circles), indicate that at higher applied voltages—where chain unravelling onto the substrate was observed for non-conductive substrates—this phenomenon does not occur with the conductive substrate. Instead, the limitation in chain length appears to stem from its weight, with the chain reaching a maximum length of approximately 50 microparticles (for solder particles with a size of 200 μm).

In Fig. 8b, we present an image array that highlights how substrate geometry and conductivity influence chain stability, providing a visual complement to the quantitative data in Fig. 8a. The images show representative outcomes for three substrate configurations—flat insulating, cylindrical insulating, and flat conductive—at applied voltages of 0.75 kV and 1.75 kV. Each image corresponds to a separate experiment, captured at the point where the chain reaches its maximum length due to substrate-induced instability.

For the flat insulating substrate (top row), strong attractive interactions with the glass substrate led to chain unravelling at higher voltages, limiting chain growth. In the case of the cylindrical insulating substrate (middle row), the curved geometry reduces these interactions, enabling longer chains to form before instability sets in. With the flat conductive substrate (bottom row), substrate-induced instability is suppressed because the chain and substrate share the same electric potential, allowing the chain to grow until gravitational forces limit its length.

3.7. Impact of gravity, system configuration, and electrical properties of the substrate

In the experiment, the results of which are presented in Fig. 6a, we observed a clear dependence of the maximum number of particles in a

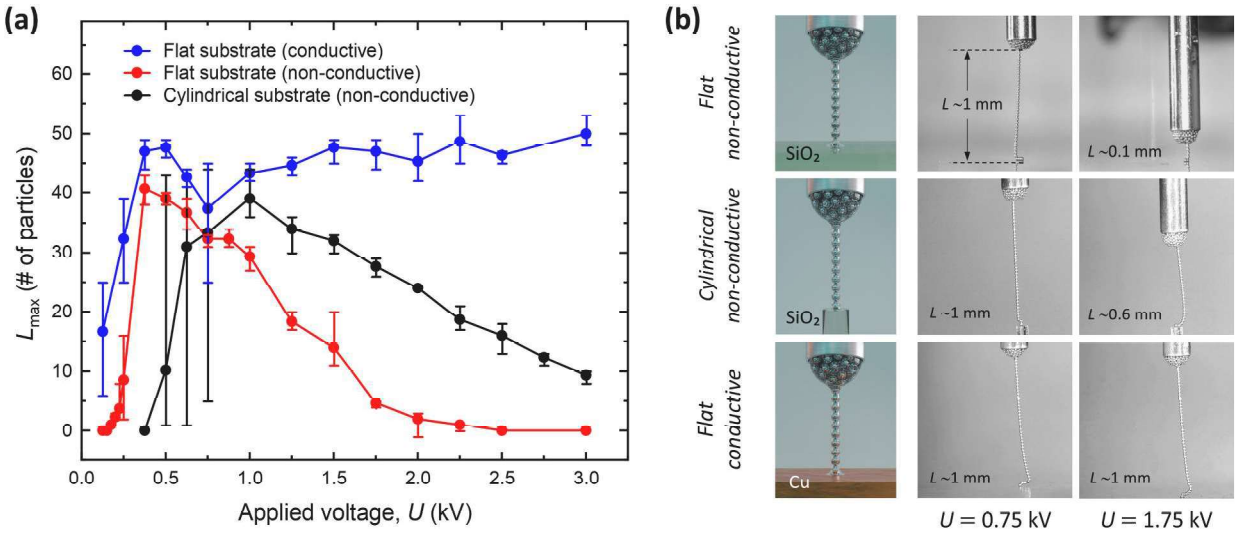

Fig. 8. (**a**) Maximum number of particles in a chain as a function of applied voltage for different substrate types and geometries. The results compare a flat non-conductive substrate (red circles), a cylindrical non-conductive substrate (black circles), and a flat conductive substrate (blue circles). Chains formed on the cylindrical substrate experience weaker interactions with the substrate, enabling longer chains to form at higher voltages than on the flat non-conductive substrate. On the conductive substrate, substrate-induced instability is suppressed, allowing even longer chains to form—limited primarily by their own weight. The data points represent the average values, while the error bars indicate the range encompassing the most extreme experimental values. The chains were made of 200-μm particles. (**b**) Image array showing chain formation for different substrate configurations at applied voltages of 0.75 kV and 1.75 kV. Each image represents a separate experiment, captured at the point of instability where the chain stops growing. The first row contains 3D renders for substrate visualization. See also the corresponding **Movie S5**.

chain on particle size. Due to interactions between the particles and the surface, as well as the emergence of an instability we termed *substrate-induced instability*, the maximum achievable chain length for different particle sizes remained uncertain. In this context, an experiment using a conductive substrate provides more relevant insights, as the chain length in this setup appears to be primarily constrained by its mass. To further investigate this effect, we conducted experiments with particles of two different sizes, 100 μm and 200 μm, with the results shown in Fig. 9a. The data clearly indicate that smaller particles form longer chains across the entire range of tested voltages. In both cases, the chain length reaches a saturation point: 16 mm (160 microparticles) for 100 μm particles and 9 mm (45 microparticles) for 200-μm particles. These lengths correspond to chain masses of 4.96 mg and 11.16 mg, respectively (note: the contribution of capillary bridges was neglected, since their effect accounts for only about 10% of the total mass). The corresponding gravitational forces acting on these chains are 49 μN and 110 μN.

Let us now examine the order of magnitude of the capillary force acting on a single particle at the dispersion meniscus interface. Assuming a simplified model in which a single particle crosses the liquid–air interface (without considering the stretching of the capillary bridge between the particle and the liquid surface [15]), the capillary force can be estimated as $F_{sp} = 2\pi\gamma r$. For the tested particle sizes, this yields values of 45 μN and 90 μN for microparticles with diameters of 100 μm and 200 μm, respectively. Since these capillary forces are lower than the gravitational forces calculated above, they are insufficient to support the full weight of the chain. Once the chain reaches its critical length, *i.e.*, when $F_g > F_{sp}$, the chain no longer remains fully suspended but begins to accumulate on the substrate. Importantly, this process does not involve chain breakage. The system stabilizes at a characteristic chain length, with new particles being continuously added to the upper end of the chain. This phenomenon is illustrated in Movie S6 and visualized in Fig. 9b. In the leftmost image (t = 70 s), the chain remains stable, indicating that the critical length has not yet been reached. Around t = 85 s, the chain spontaneously began to unravel and descend onto the substrate. At this point, the conduit motion was halted; however, chain formation at the dispersion meniscus continued, while the lower portion progressively accumulated on the substrate. The subsequent images show the gradual growth of this particle accumulation, which corresponds to the excess portion of the chain that settles as new particles are continuously added at the meniscus.

The data presented in Fig. 9a,b indicate that the maximum chain length L_{max} depends on particle size and is ultimately limited by the chain's mass. When the chain becomes sufficiently heavy, the

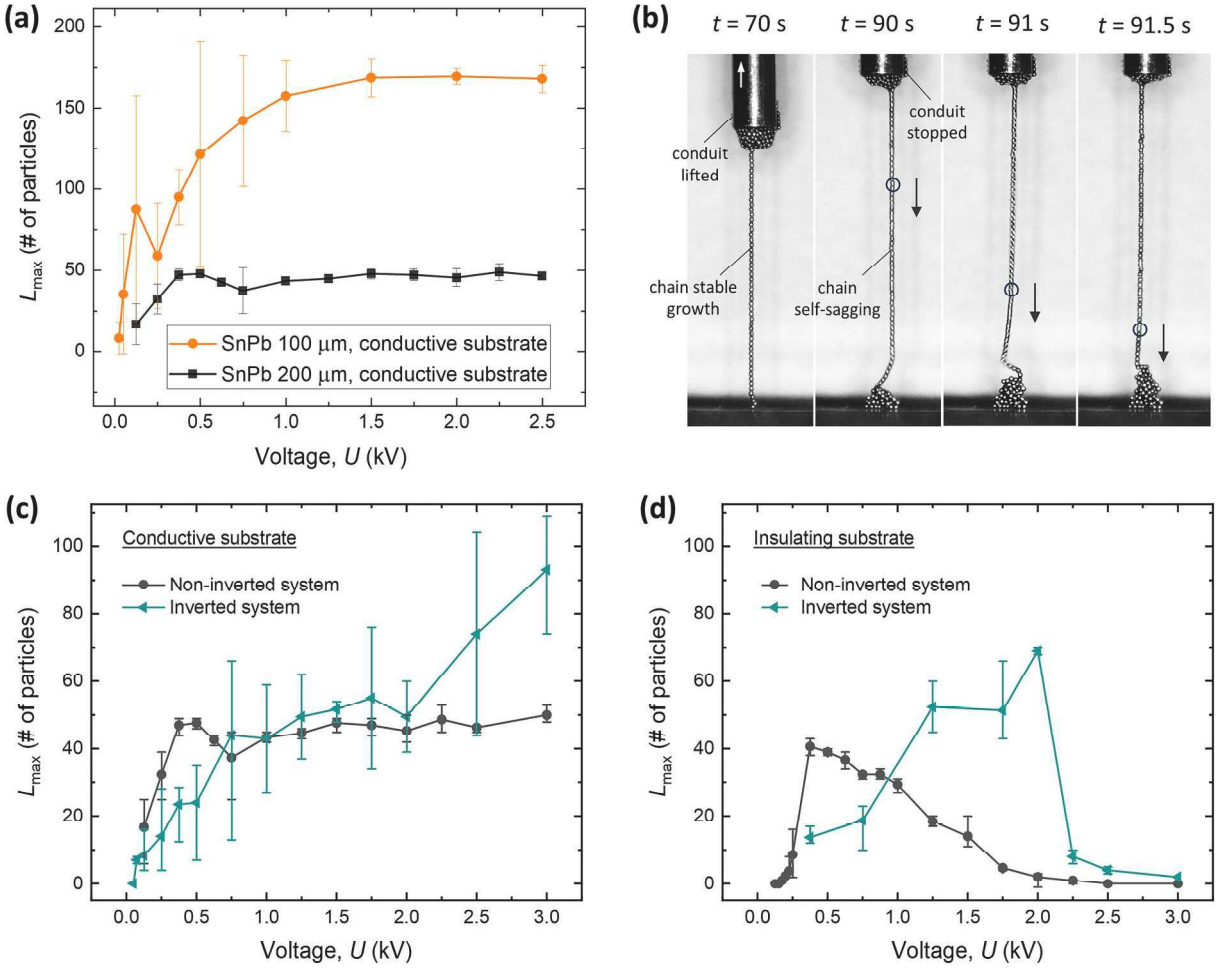

Fig. 9. (**a**) Maximum chain length L_{max} as a function of applied voltage U for solder microparticles with diameters of 100 μm and 200 μm on a conductive substrate. The chain length is limited by the chain's mass, with smaller particles forming longer chains before destabilization. (**b**) Sequential images showing chain behaviour over time: at t = 70 s, the chain remains stable and fully suspended; at t = 90 s, the chain begins to sag and accumulate particles on the substrate. Despite stopping the conduit motion, chain formation continues at the meniscus while the lower portion accumulates on the substrate. (**c**) L_{max} *vs.* U for 200-μm solder particles on a conductive substrate in non-inverted and inverted configurations. In the inverted system (meniscus facing upward), higher voltages are required to initiate chain formation, yet longer chains are produced compared to the non-inverted system. (**d**)) L_{max} *vs.* U for 200-μm solder particles on a non-conductive substrate. In the inverted system, longer chains are formed at intermediate voltages (1–2 kV), yet substrate-induced instability still occurs—albeit at higher voltages than in the non-inverted system.

gravitational force prevents the chain from remaining suspended at the dispersion meniscus. Consequently, new particles added from the meniscus continuously accumulate at the chain's lower end, maintaining a constant chain length.

To further explore this behaviour, we hypothesized that in an inverted system configuration—where the conduit with the dispersion meniscus at its outlet is positioned facing upward while the substrate is placed above it—spontaneous particle extraction from the meniscus against the direction of gravity would be impossible. Consequently, we assumed that an additional driving force would be required to initiate chain formation.

Fig. 9c presents the results for 200-μm particles on a conductive substrate, comparing the inverted and non-inverted systems. The data show that in the inverted system, higher voltages are required to initiate chain formation compared to the non-inverted system. This behaviour supports our hypothesis, suggesting that the upward-facing meniscus introduces a higher energy barrier for particle extraction, as both capillary forces and gravitational pull must be overcome.

Interestingly, in the inverted system, the data suggest that higher voltages enable the formation of longer chains. Although measurement uncertainty introduces some scatter in the data, a general trend indicating a linear dependence between the maximum chain length (L_{max}) and the applied voltage (U) can be observed. The chains in the inverted system typically break at the point of contact between the first particle and the substrate. This occurs because gravitational pulling is strongest at this point, as the chain segment below carries the greatest mass. Additionally, the attractive interaction of the capillary bridge formed between the substrate and the first particle beneath it is weaker than the interactions resulting from the capillary bridges formed between the microparticles themselves.

In the second part of the study, we investigated chain formation on a non-conductive substrate (Fig. 9d). For the inverted system, the chain length exceeded that of the non-inverted system at voltages between 1 kV and 2 kV. However, despite the substrate being positioned above the chain, substrate-induced instability was still observed. The chain eventually curved toward the substrate, albeit at higher voltages compared to the non-inverted system.

In contrast, for the conductive substrate (Fig. 9c), substrate-induced instability was not observed in the inverted system. The chain length continued to increase with voltage. Nevertheless, increasing the voltage indefinitely proved unfeasible, as high voltages led to additional phenomena such as plasma formation near the particles.

At the end of this section, we present results from experiments conducted with materials of different densities. Specifically, we used stainless steel microparticles with a density of 7.8 g·cm^{-3} and glass microparticles coated with a thin layer of silver (less than 1 μm) with a density of 2.5 g·cm^{-3}. The experiments were carried out at low voltages (0.25–0.5 kV), a range in which the longest chains are achieved, and substrate-induced instability is minimal. The same configuration as that used in the experiment presented in Fig. 6 was used, *i.e.*, with a non-conductive, ungrounded glass substrate and voltage applied to the conduit. For each type of microparticle, we selected the result corresponding to the longest chain formed and compared it with previously measured results for solder microparticles with a density of 8.4 g·cm^{-3}.

The longest chain formed was the one that became self-sagging or experienced substrate-induced instability—typically occurring just moments before self-sagging began. In the initial stage of chain formation, the conduit must be actively lifted to elongate the structure, as each particle is drawn from the meniscus and incorporated into the growing chain. However, as the chain increases in length, its mass grows correspondingly, and the gravitational force acting on it eventually exceeds the capillary force that had previously retained the next particle at the fluid–air interface. Once this critical balance is surpassed, the weight of the chain alone becomes sufficient to overcome the capillary retention, causing the next particle to be released and incorporated into the structure without the need for further mechanical elevation of the capillary. From this point on, the process enters a passive, self-sustaining regime in which the chain continues to grow downward under its own weight, even while the conduit remains stationary.

Fig. 10 presents the results on a log–log scale. Panel (a) shows the maximum chain length as a function of particle diameter. The data points follow a clear trend, indicating that the longest chains are formed using smaller microparticles. The observed slope of –2 aligns with expectations, which can be explained by the balance of forces. The gravitational force acting on the chain increases with its total mass, which scales as $N{\cdot}r^3$, where N is the number of particles in the chain. In contrast, the capillary force that retains the last particle in the meniscus scales linearly with r. Equating the two gives $N{\propto}r^{-2}$, in agreement with the experimental data.

This behaviour is consistent across all tested materials, confirming that particle size plays a dominant role in determining the achievable chain length—with the exception of the blue data point, which corresponds to Ag-coated glass microparticles. These core–shell particles are substantially lighter than the others, allowing for the formation of longer chains. However, the observed chain length is still shorter than expected based on the nearly threefold difference in density, suggesting that additional factors may be limiting chain formation in this case.

Panel (b) presents the corresponding total mass of the longest chains. The data follow a clear trend with a slope of 1, indicating a linear dependence of chain mass on particle diameter. This trend is consistent with the calculated total mass, which accounts for the number of particles, their material density, and the estimated contribution from the surrounding liquid. The deviation observed for these particles arises from their markedly lower density, which weakens gravitational stabilization and makes the system more sensitive to capillary bridge effects and interactions with the surrounding medium. As a result, the chain length is ultimately limited despite the small particle size.

3.8. Pulling velocity, voltage, and liquid viscosity

In this section, we analyse the influence of pulling velocity, applied voltage, and dispersion liquid viscosity on the formation of 1D beaded structures from bulk liquid. Understanding these relationships is essential for optimizing experimental parameters and controlling the stability of microparticle structures.

In Fig. 11a–d, we present four sets of experiments conducted at different applied voltages, ranging from 0.5 kV to 1.5 kV. Each graph shows how the maximum chain length depends on the pulling velocity. At the lowest voltage (0.5 kV), once the pulling velocity exceeds 1 particle/s (equivalent to 200 μm/s for 200-μm particles), the chains become progressively shorter. After a one-decade increase in pulling velocity, chain formation is no longer possible.

As the voltage increases, the critical pulling velocity shifts to higher values. We define the critical velocity arbitrarily as the point where the chain length reaches 80% of the maximum achievable length for a given voltage (marked with a dashed line). Interestingly, the maximum chain length is not always attained at the lowest pulling velocities, which may seem counterintuitive. For example, at 1.25 kV and 1.5 kV, the maximum chain length occurs around 10 particles/s. This phenomenon arises because, at higher voltages, slower pulling speeds promote substrate-induced instability. Increasing the pulling velocity imposes more tension on the chain, counteracting the tendency of the chain to sag and its attraction to the non-conductive substrate. However, above the critical velocity, the chains shorten due to viscosity-related breakage. At higher velocities, increasing viscous drag generates tensile forces that capillary bridges and electric attractions between particles can no longer withstand, causing the chains to break.

In Fig. 11e, we present a phase diagram summarizing the outcomes of chain formation experiments performed using solder particles dispersed in a 150 mPa·s silicone oil, as a function of the applied voltage and pulling velocity. The diagram illustrates three distinct regions:

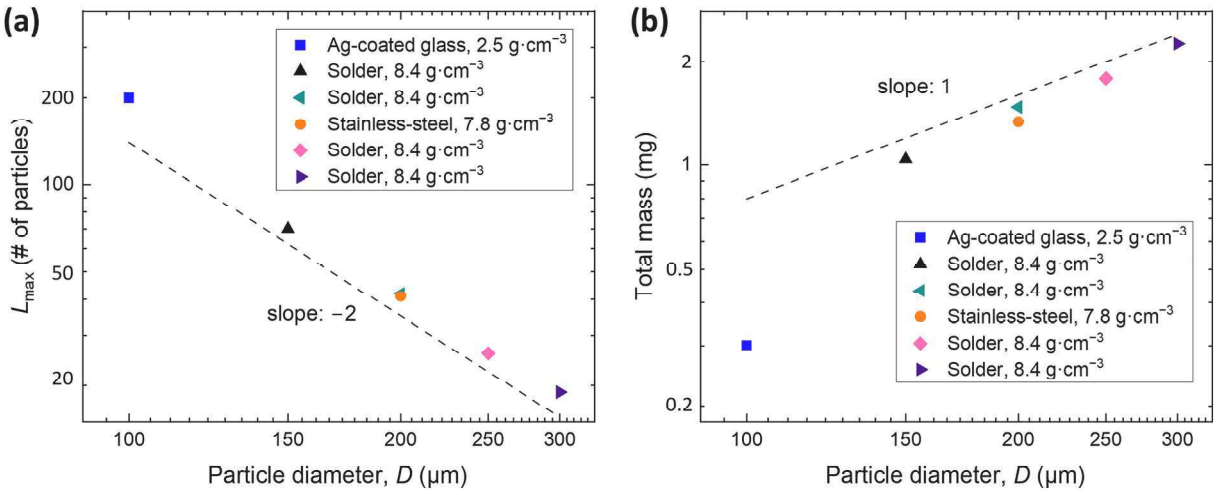

Fig. 10. (**a**) L_{max} as a function of particle diameter (D) for different materials. A consistent power-law decay is observed, with the dashed reference line indicating a slope of approximately –2. (**b**) Total mass of the longest chains as a function of particle diameter. The data exhibit a linear trend (slope of approximately 1), reflecting the expected scaling of chain mass with particle size. Only the blue square, representing Ag-coated glass particles, deviates noticeably from the observed trends in both panels.

failure to initiate (open circles), where the electric tension is too low to form even a dimer; *electric-force-limited breakage* (pink diamonds), where the chain breaks during the pulling process; and *substrate-induced instability* (blue circles). The boundaries between these regions, though drawn as sharp lines, are actually broad, as evidenced by overlapping data points. This variability arises from the inherent randomness of the system, such as particles emerging from the interface under slightly different local conditions, polydispersity in particle size, and shape irregularities. This phase diagram thus provides a comprehensive guide for selecting optimal experimental conditions to achieve stable 1D beaded structures.

It could be expected that with increasing viscosity η, the critical velocity v_{cr}, below which the chain remains long and stable, would decrease proportionally, since the drag force scales as $F_d \propto \eta v$. Therefore, if the viscosity increases by two orders of magnitude (100 ×), we expect v_{cr} to decrease by the same factor, shifting the curve towards lower velocity values by approximately two decades. However, experimental results presented in Fig. 11f show a weaker dependence, where the shift in critical velocity is only one decade. This discrepancy may be attributed to changes in the shape of the capillary bridge formed between the pulled particle and the meniscus surface. At higher viscosities, more liquid is drawn along with the chain, creating a funnel-like shape at the base of the meniscus. This increased liquid volume reduces the local capillary force acting on the particle being pulled from the meniscus. As a result, chains can form at higher pulling velocities than expected, partially offsetting the increased viscous drag and explaining the observed deviation from the predicted two-decade shift. Additionally, the capillary bridges formed between particles in the chain, now made of higher viscosity liquid, may provide greater stability. The increased viscosity likely delays the breakup of these bridges, allowing the chain to withstand transient disturbances more effectively and maintain its integrity over short timescales. This is a highly complex phenomenon that warrants further investigation, but such an analysis is beyond the scope of this work.

3.9. Disordered particle chains

In the previous sections, we analysed the formation of particle chains composed of nearly monodisperse microparticles, resulting in structures that can be referred to as 1D particle crystals due to their regular and periodic arrangement. Here, we explore the formation of *disordered* particle chains—structures that lack periodicity, typically due to the use of polydisperse microparticles. We hypothesized that single-particle-thick chains could still form with moderately polydisperse particles, even though they would not qualify as particle crystals. However, we expected that a high degree of polydispersity might lead to more irregular, agglomerated assemblies. In this section, we test these hypotheses through a series of experiments.

First, we conducted an experiment using a binary system consisting of monodisperse particles of two different sizes. Fig. 12a presents the results for a dispersion containing unleaded solder microparticles with diameters of 200 μm and 250 μm (estimated PDI ≈ 0.005). A slightly higher mass fraction of the larger particles was used to balance the approximate number of particles of each size in the dispersion. During the experiment, we could not control the local arrangement of particles in the meniscus, and thus the resulting chains showed a random distribution of particle sizes, with interspersed regions where one large particle was followed by several smaller ones, or vice versa. The results obtained for the binary system (navy colour in Fig. 12a) were compared with those for monodisperse systems of 200 μm and 250 μm particles. The behaviour of the binary system closely resembled that of the larger particles (250 μm).

In a second experiment, we used a polydisperse dispersion with particle sizes ranging approximately from 140 μm to 320 μm, for which the PDI was ten times higher than in the previous experiment (PDI ≈ 0.05). This level of PDI is often found in industrial batches of particles with moderate polydispersity. As in the previous experiment, we did not observe any significant influence of polydispersity on the process of forming single-particle-thick structures — the resulting chains remained straight and retained a thickness corresponding to a single particle. Fig. 12b presents examples of these disordered chains.

3.10. Application of the acquired knowledge

3.10.1. Continuous formation of structures

In principle, the chain extraction process can continue indefinitely, provided liquid dispensing is well-controlled, the dispersion concentration remains stable, and the chain length stays below the threshold of instability (explained in Section 3.4). Common disruptions to continuous particle pulling from the dispersion meniscus include impurities, irregular particle shapes, vibrations, air currents—all of which can induce structural instabilities and break the chain's structural continuity (see **Fig. S3** for an example).

Fig. 13 illustrates the continuous formation of a three-dimensional

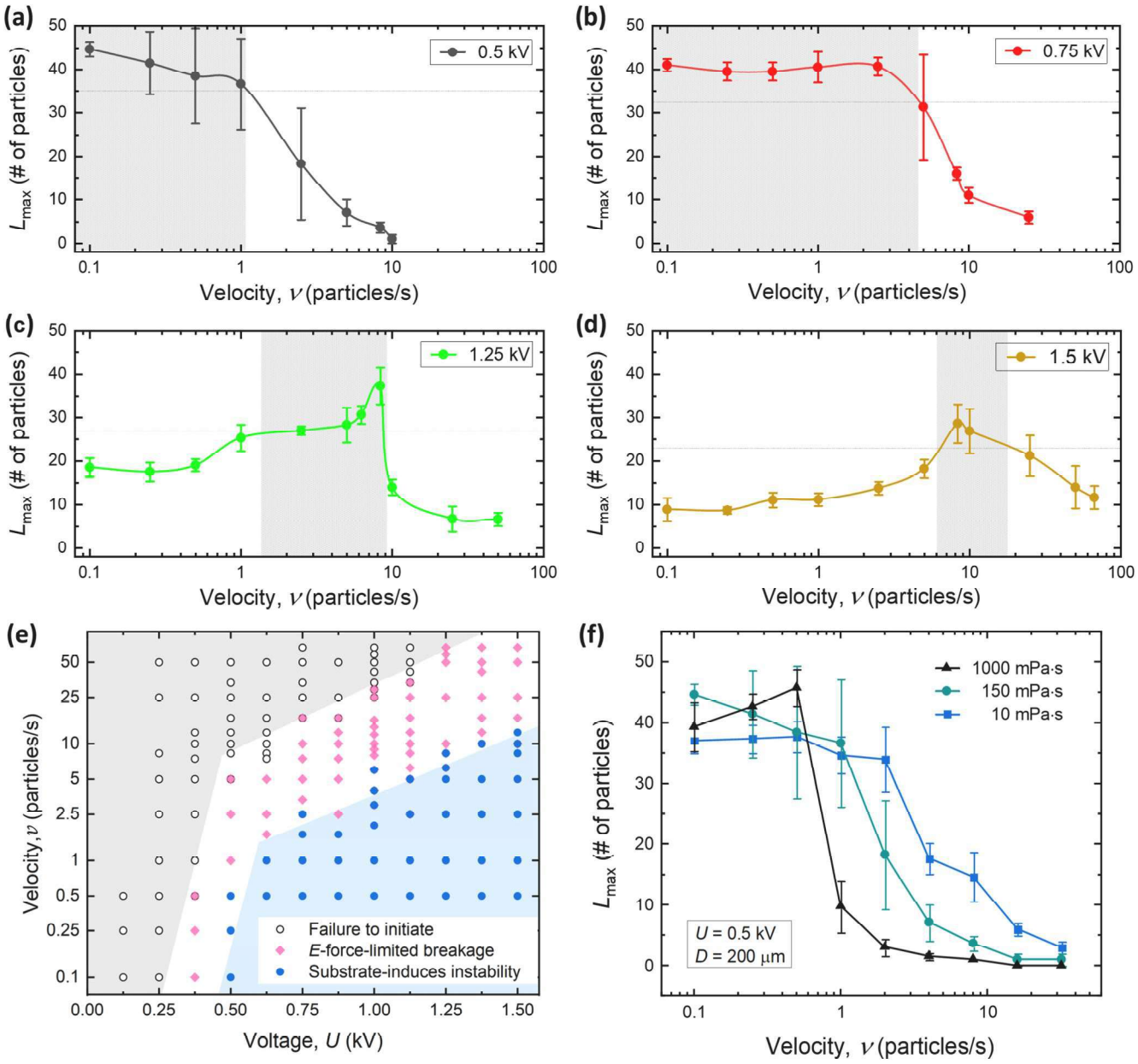

Fig. 11. Influence of pulling velocity, voltage, and viscosity on 1D beaded structure formation. (**a–d**) Maximum chain length (L_{max}) vs. pulling velocity for voltages ranging from 0.5 to 1.5 kV. Higher voltages increase the critical pulling velocity but limit the range of optimal performance, indicated by shaded areas where the chain length exceeds 80 % of the maximum. (**e**) Phase diagram summarizing data collected for 200-μm solder particles dispersed in silicone oil (150 mPa·s) under 12 different voltages, increasing in 0.125 kV increments. The boundaries between regions are shown as sharp lines but are actually broad due to system variability. (**f**) Effect of dispersion viscosity (10–1000 mPa·s) on L_{max} at 0.5 kV and 200-μm particles. The curves shift left with increasing viscosity due to greater drag forces, reducing the maximum chain length achievable at higher pulling velocities. See also the corresponding **Movie S7**.

structure using stainless steel microparticles (~50 μm) dispersed in silicone oil (100 mPa·s). The particles are dispensed through a conductive capillary (0.8 mm in diameter) and wound around a rotating optical fibre (~300 μm in diameter) under a 1.0 kV, 1 kHz electric voltage. This controlled process results in a helical structure, which continues uninterrupted until deliberately stopped and the voltage is turned off (see Movie S8).

3.10.2. *Particle-chain bridging between conductive structures*

Another practical application of the acquired fundamental knowledge is the realization that chains can also be formed on electrically conductive substrates, thereby avoiding substrate-induced instability. Based on this, we hypothesized that it would be possible to create suspended structures between metallic elements—structures long and stable enough to serve, for example, as freestanding interconnects analogous to wire bonds. To test this hypothesis, we designed and conducted an experiment to demonstrate this concept. As shown in Fig. 14 and Movie S9, SAC305 (lead-free solder) microspheres with a diameter of 150 μm were assembled into freestanding chains that bridge 0.64 mm copper terminals mounted on two separate printed circuit boards (PCBs).

Fig. 14a presents a time sequence of the bridging process. A dispersion meniscus is formed at the nozzle tip via controlled flow from a syringe pump. The nozzle is initially positioned near a vertical pin on the first PCB. Under an applied voltage (0.25 kV, 1 kHz), a chain of approximately 20 microparticles assembles upward from the surface (t = 0–8 s). The nozzle then translates laterally toward a corresponding pin on the second PCB, resulting in the formation of a suspended chain that

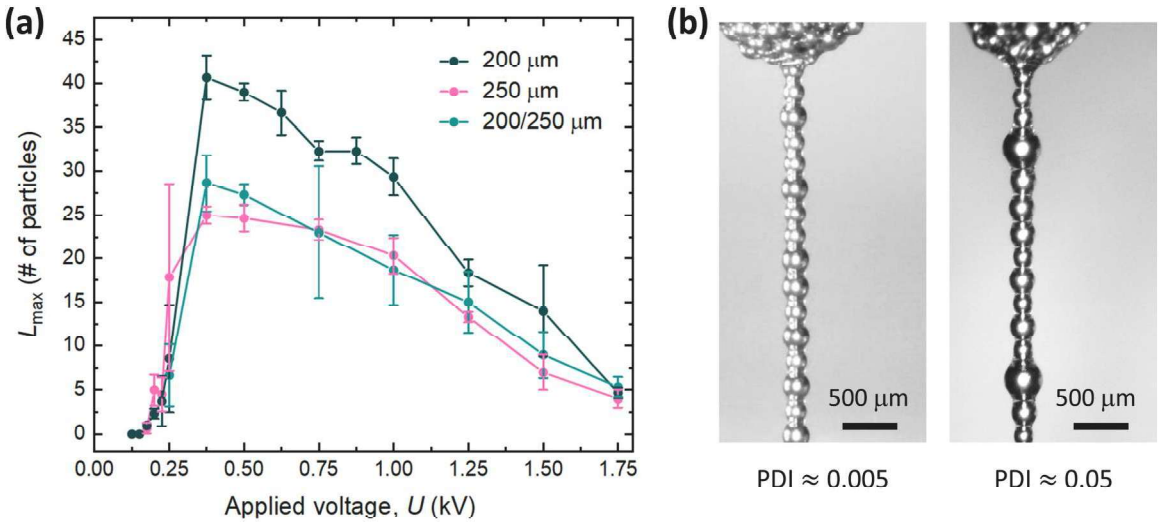

Fig. 12. (**a**) Maximum chain length L_{max} as a function of applied voltage U for chains formed from nearly monodisperse particles of 200 μm ± 3 % (black), 250 μm ± 3 % (pink), and alternating 200/250 μm particles (navy). The data indicate that the L_{max} values for the 200/250 μm mixed chain closely resemble those for the 250 μm chain. (**b**) Microscopy images of examples of single-particle-thick structures formed from binary (PDI ≈ 0.005, left) and polydisperse (PDI ≈ 0.05, right) dispersions. Despite the higher polydispersity in the second case, the resulting chains remain straight and retain a uniform thickness corresponding to a single particle.

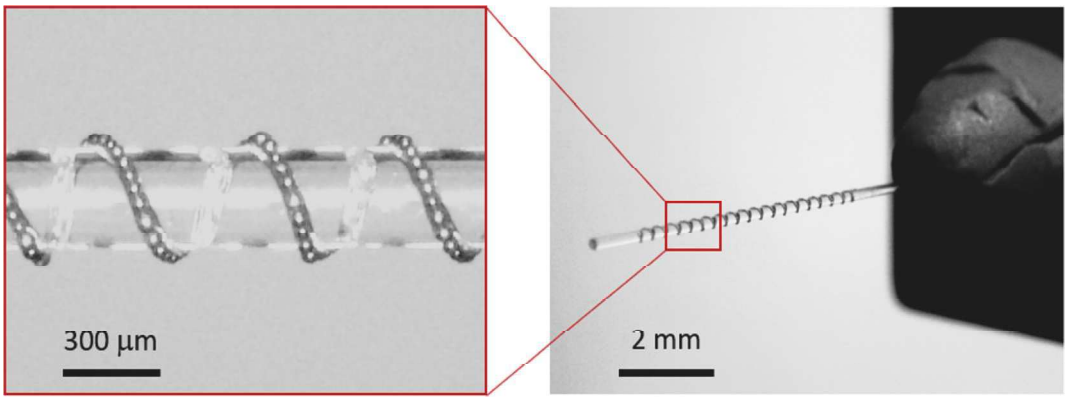

Fig. 13. Continuous particle pulling: Stainless steel microparticles (~50 μm) suspended in silicone oil (100 mPa·s) are dispensed through a conductive capillary (diameter ~0.8 mm). Under a 1 kV, 1 kHz electric voltage and with the rotation of an optical fibre (diameter ~300 μm), the particles are wound into a helical structure.

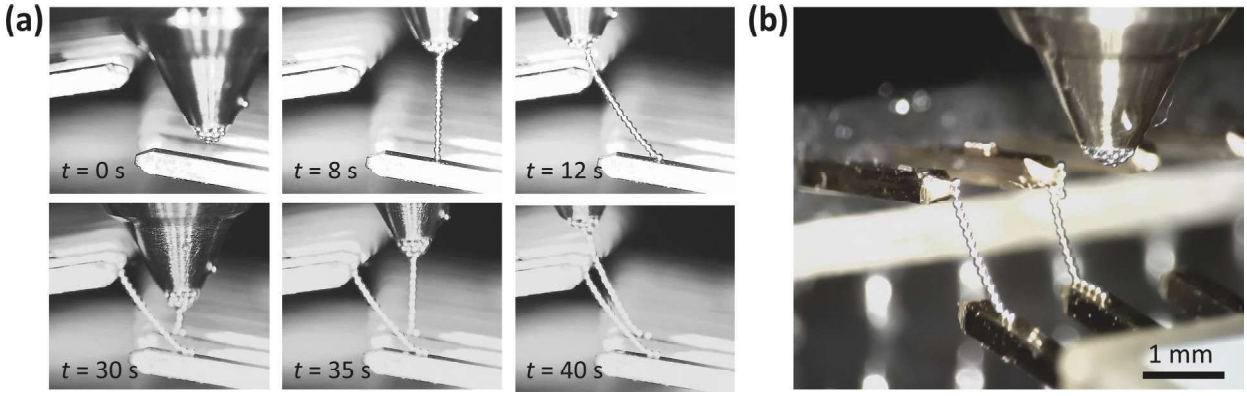

Fig. 14. Bridging of conductive elements using field-assembled chains of 150-μm SAC305 microparticles. (**a**) Time-lapse images showing the formation of two suspended chains connecting two pairs of copper terminals mounted on separate PCBs. Each chain is assembled from the meniscus of a particle dispersion using a voltage of 0.25 kV. After vertical growth from the first pin (t = 0–12 s), the nozzle then moves laterally to complete the connection to the second pin (t = 12 s). The process is subsequently repeated at a nearby location to form the second bridge (t = 30–40 s). (**b**) View from a different angle showing the two freestanding chains formed sequentially between neighbouring terminals.

bridges the two pins (t = 12 s). Once the second connection is established, the electric field is turned off. The chain remains intact and suspended between the two components. The nozzle is subsequently repositioned approximately 2 mm away, and the process is repeated to form a second interconnection. Fig. 14b presents a different viewing angle of the system, showing two freestanding chains formed sequentially between adjacent pins.

3.10.3. Chain-based structures as resilient alternatives to solid micro-wires

Another application that builds directly on the knowledge acquired in previous sections is the use of particle chains as mechanically resilient alternatives to conventional micro-wires. We have established that, unlike during formation on insulating substrates, chains are not electrostatically attracted toward narrow conductive substrates. This allowed us to fabricate suspended structures that do not adhere to the surface, thereby enabling mechanical testing.

To evaluate their mechanical performance, we tested a freestanding chain composed of 25 SAC305 microballs (diameter: 200 μm; total length: 5 mm) under cyclic axial deformation. The chain was compressed and released by approximately 10% of its length in each cycle (from 5.0 mm to 4.5 mm and back), while a voltage of 0.25 kV was maintained throughout the test. Remarkably, the structure withstood between 280 and 395 compression–relaxation cycles (across three independent experiments) without fracture, maintaining both structural integrity and visual continuity at all times (see Fig. 15).

For comparison, a standard cylindrical wire (200 μm diameter, 5 mm length) made of either copper or solder was subjected to identical cyclic deformation. In such solid wires, mechanical failure typically occurs after only 15–50 cycles under axial strain amplitudes of about 10%, due to the accumulation of localized plastic deformation. This deformation leads to fatigue crack initiation and propagation, particularly near fixed boundary regions, where bending and tensile stress are concentrated. In our own tests using copper wire segments with the same geometry, complete fracture occurred after 35–47 cycles, while SAC305 solder wires failed after only 16–26 cycles. These results are consistent with the well-established low-cycle fatigue behavior of ductile metals, where short, rigid segments subjected to repeated strain rapidly accumulate damage and ultimately fail through necking or brittle crack formation.

The superior durability of the chain-based structure stems from its modular and reconfigurable architecture, in which mechanical stress is distributed through soft, reversible liquid bridges rather than concentrated in a continuous solid core. Additionally, the presence of an electric field contributes to enhanced cohesion of the structure by maintaining alignment of particles. This combination of mechanical adaptability and field-induced cohesion enables the structure to accommodate deformation through internal rearrangements, minimizing localized damage and eliminating fatigue crack propagation mechanisms common in traditional wires.

3.10.4. Voltage-controlled retraction and extension of suspended particle chains

In this final demonstration, we show that the length of a suspended microparticle chain can be reversibly and precisely modulated by varying the applied electric voltage—without any mechanical motion of the system. The chain is formed in air, suspended between a liquid meniscus at the outlet of a stationary conduit and a passive substrate below.

In the initial phase, a voltage of 0.5 kV is applied to extract particles from the dispersion meniscus and form a vertically aligned chain composed of approximately 20 microparticles (Fig. 16a,b). Once the chain is formed, the applied voltage is modulated between 0.25 kV and 1 kV, while the conduit remains stationary. This voltage modulation causes the chain to alternately extend and retract increasing the voltage strengthens electrostatic attraction, pulling additional particles from the meniscus and lengthening the chain; decreasing the voltage weakens the field, resulting in partial detachment or redistribution of particles, and shortening of the chain. Because the chain remains mechanically connected at both ends, these changes occur reversibly and without breakage.

To visualise this behaviour, a lightweight and flexible element (a strip of paper) was placed beneath the chain. As the chain elongates under higher voltage, its weight and tension increase, causing a gentle downward deflection of the substrate. Conversely, as the chain shortens, the applied force decreases, and the substrate returns to its original position. This visible deformation confirms that voltage modulation not only controls chain length, but also the mechanical force transmitted through the structure. This cycle of extension and retraction is fully reversible and repeatable (Fig. 16c–f).

4. Discussion

In the following discussion, we expand upon the main experimental findings by analysing selected mechanisms in greater depth and highlighting their implications for structure formation. While the preceding

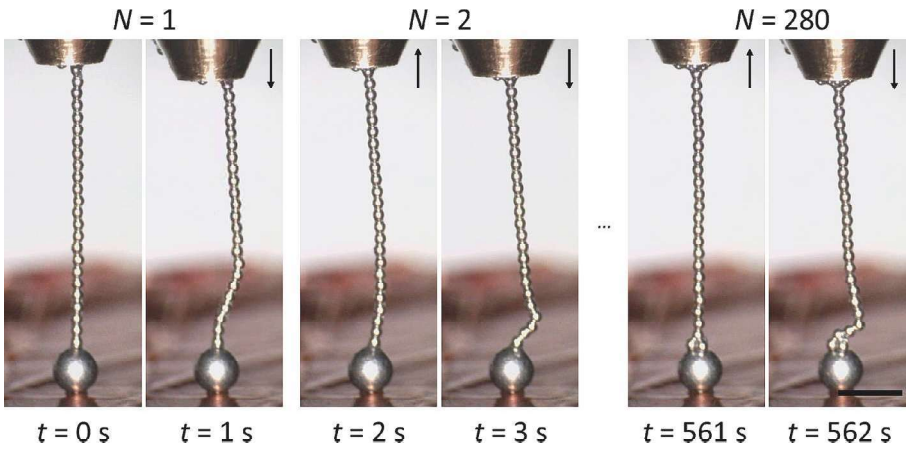

Fig. 15. Mechanical durability of a suspended particle chain subjected to repeated axial compression. A chain of SAC305 solder microballs formed in air and stabilized by voltage provided to the nozzle (0.25 kV, 1 kHz) is cyclically compressed and released by approximately 10 % of its initial length. To suppress substrate-induced instabilities during contact, a single 760-μm solder microball was placed on a non-grounded copper pad beneath the chain. The nozzle was displaced vertically with an amplitude of 0.5 mm at a speed of 1.67 mm/s (G-code: F100). The snapshots show the beginning of the experiment (left), selected moments during the first two compression–relaxation cycles (N = 1–2), and the final cycles near N = 280 (right). Arrows indicate the vertical movement direction of the nozzle. See also the corresponding **Movie S10**.

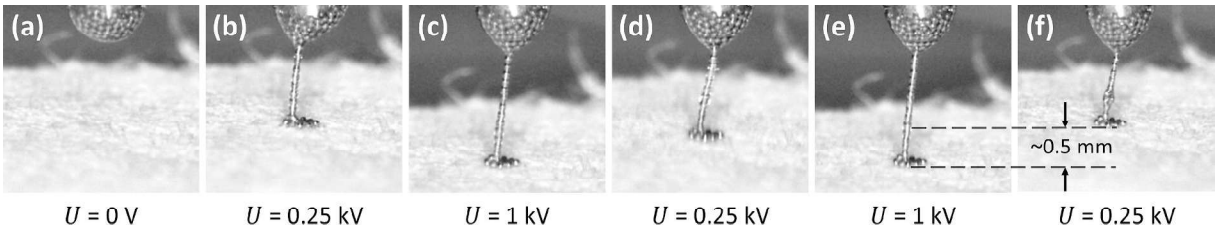

Fig. 16. Voltage-controlled modulation of a suspended microparticle chain. (**a,b**) Initiation and vertical growth of the chain from a stationary dispersion meniscus at the outlet of the conduit upon the application of an AC voltage (U = 0.25 kV). (**c–f**) Reversible elongation and contraction of the chain in response to voltage modulation between 0.25 and 1.0 kV, with the conduit remaining fixed. The increased chain length at higher voltage (**c, e**) leads to visible deflection of the lightweight flexible substrate, whereas reduced voltage (**d, f**) results in shortening of the chain and substrate relaxation. The total displacement of the substrate is approximately 0.5 mm, serving as direct evidence of voltage-controlled force transmission through the chain. See also the corresponding **Movie S11**.

sections focused on identifying key process parameters, here we address secondary effects, non-intuitive behaviours, and/or deviations from idealized models.

Simplified geometry used in numerical simulations: To perform numerical simulations in COMSOL, we used a simplified geometry in which the dispersion meniscus was approximated as a metallic hemisphere. To verify the validity of this simplification, we carried out additional 3D simulations using a more realistic model: the hemisphere was filled with liquid (assigned a permittivity corresponding to silicone oil) and contained several dozen spheres representing microparticles. These full 3D simulations required significantly more computational power and time. However, the results obtained were in close agreement with those from the simplified 2D axisymmetric model, with only negligible differences. Therefore, to reduce computational time while maintaining accuracy, we used the 2D axisymmetric model for all simulations.

Effect of meniscus shape and particle arrangement variability on threshold voltage: Regarding the presented data, it is worth noting that the voltage threshold (around 0.125–0.25 kV as observed in Fig. 6a) would generally be expected to increase with particle size, as a larger voltage would be required to overcome the capillary force stemming from the capillary bridge (between the particle at the interface and the liquid plane) that prevents the particle from leaving the liquid–air interface. However, this trend is not very clear in the data. One possible reason could be the low statistical sample size. Another reason might be the more complex configuration of the meniscus, where many particles are packed together and interact with one another. In each experiment, the spatial arrangement of microparticles within the meniscus and at its surface differs due to randomness in particle placement. This variability affects both the cohesive interactions between particles and the capillary forces [40], ultimately leading to differences in the force required to extract individual microparticles.

Absence of chain straightening despite field application: Interestingly, the electric interaction does not counteract the spontaneous extraction of particles from the liquid meniscus, as demonstrated in Fig. 9b and Movie S6. However, it still positively influences the formation of 1D microparticle structures. In the case of classical dielectrophoresis or dipole–dipole interaction, particles in the chain would typically experience strong mutual interactions, leading to chain straightening. This, however, is not the case here.

Capillary anchoring at the meniscus prevents self-unravelling of the chain: The capillary restoring force acting on the topmost particle limits the self-extension of the chain. Specifically, F_{sp} may exceed the total weight of the suspended portion of the chain, creating a mechanical constraint that prevents sagging or spontaneous elongation under gravity. Estimated values of the capillary force and the corresponding maximum number of suspended particles are provided in Table 1. The values are consistent with those observed experimentally and plotted in Fig. 10a. However, it should be noted that the calculations in Table 1 are based on a simplified force balance model that considers an individual, isolated microparticle. In practice, multiple microparticles coexist and interact within the meniscus region. As demonstrated in a carefully designed experiment reported in [40], the proximity of neighbouring particles reduces the effective capillary force acting on each of them. This reduction arises from geometric constraints that distort the local shape of the liquid–air interface, thereby diminishing the restoring force generated by the meniscus. Additionally, the meniscus in our system is convex rather than flat, which further reduces the upward capillary force compared to the idealized scenario of a particle resting on a planar liquid surface. These factors may explain the small discrepancy between the calculated values and the experimentally observed chain lengths.

Table 1
Estimated capillary retention forces and the corresponding maximum number of particles that can be suspended in a vertical chain without external forces, for various particle radii. Calculations assume a particle density of $\rho = 8.4\ \mathrm{g{\cdot}cm^{-3}}$ and a surface tension of $\gamma = 20\ \mathrm{mN{\cdot}m^{-1}}$.

Particle diameter, D (μm)	50	100	150	200	300	400
Capillary force, F_{sp} (μN)	3.1	6.3	9.4	12	19	25
Max number of particles L_{max} (number)	582	146	65	36	16	9

Chain stability: After formation, the particle chain remains stable both when the electric tension is applied and when it is turned off. To test long-term stability, we conducted overnight experiments in which chains consisting of 40 microparticles (diameter: 200 μm) were suspended between the dispersion meniscus and a conductive substrate. The chains were left undisturbed under three voltage conditions: 0 kV, 0.5 kV, and 1 kV. Laboratory conditions were maintained at 23 ± 2 °C and 30 ± 10% relative humidity. No changes in chain structure or position were observed under any condition, indicating that the chains remained fully stable regardless of the applied voltage.

Particles and liquids: Regarding particle size, as indicated in previous studies [16–18], it is possible to use microparticles within a broad size range, approximately from 10 to 500 μm. The physical lower limit is likely around the micron scale, where Brownian motion and interparticle cohesive forces start to play a significant role. The upper limit, in turn, is primarily constrained by gravitational forces, which scale with particle density. For instance, glass beads coated with a conductive layer—whose density is roughly a hundred times lower than that of solid metals—can extend the practical upper limit toward the millimetre scale.

In terms of material configuration, both solid and core–shell microparticles with conductive outer surfaces can be successfully used. In this study, we also demonstrated the use of three-phase microparticles, such as hollow glass spheres coated with conductive silver and containing air inside, offering extremely low effective density combined with sufficient surface conductivity. A particularly intriguing future direction could involve the use of Janus particles, whose surfaces are partly conductive and partly insulating. These asymmetric particles may enable new types of anisotropic interactions and directional alignment effects under electric fields.

In this manuscript, we primarily employed silicone oil as a non-polar,

low-conductivity dispersion medium. Additional tests were conducted using other liquids, including natural (non-synthetic) castor oil and soldering flux, the latter potentially improve bonding between solder microparticles and underlying substrates in application-oriented contexts.

5. Conclusions

In this work, we developed and explored an electric method for forming single-particle-thick microstructures that can be created outside a bulk liquid. Such structures, when aligned and formed of monodispersed particles, can be considered as 1D particle crystals; otherwise, they form disordered 1D structures—both of which we refer to here as particle chains. We studied in detail the influence of various parameters, including electric tension, particle size and type, viscosity of the dispersing liquid, substrate geometry and electrical properties, as well as system configuration on the assembly process, the stability of the final particle chain, and its length.

The microparticle chains exhibit distinctive properties—including their geometry, periodicity, optical and electrical characteristics, and the ability to polarize and attract at particle contact points—which make them especially promising for practical applications. We believe that the proposed methodology for the electric formation of particle chains offers numerous opportunities for developing functional materials. Potential applications include conductive tracks (for electrical signal transmission), resistive tracks for heating elements (for defrosting systems or heated windows), moisture condensation systems (for passive water collection in arid environments), humidity detection sensors (for environmental monitoring), heat dissipation structures (for thermal management in electronics), or flexible conductive pathways (for wearable electronics and stretchable sensors) designed for dynamic or deformable surfaces where traditional solid wires fail.

To illustrate the practical relevance of these findings, we demonstrated four out of many possible real-world applications of particle chains formed by the proposed electric method. The first example involved the continuous formation of three-dimensional structures by guiding particles to wind around a rotating fibre, showcasing the ability to produce controlled, spatially extended architectures with potential uses in microscale reinforcement, microcoiling, antennas, and hybrid material design.

The second demonstration focused on connecting conductive components that were mounted on separate substrates by forming suspended particle chains between them. This example highlights the capability of field-guided particle assembly to construct suspended microstructures that form connections between a variety of conductive elements, such as pins, pads, or microelectrodes. These structures may offer potential applications in reconfigurable electronics, rapid prototyping, or temporary interconnects in microscale systems.

In the third demonstration, we revealed one of the unique mechanical properties of suspended chains: their remarkable durability to repeated axial deformation. Despite undergoing hundreds of compression–relaxation cycles, the chain maintained structural continuity, outperforming conventional micro-wires of the same size by more than one order of magnitude, which typically fracture after only a few dozen cycles. These findings indicate that suspended particle chains may offer an alternative to solid micro-wires, particularly in applications that involve repetitive mechanical loading or vibration — such as flexible electronic interconnects, soft robotics, and dynamic testing setups where standard wires tend to fail prematurely.

The fourth demonstration showcased the ability to reversibly and dynamically modulate the chain's length by adjusting the applied voltage—without moving any mechanical parts. In this configuration, the suspended chain extended or retracted in response to increasing or decreasing electric field strength. This behaviour can be conceptually likened to an *electrostatically controlled tendon*, where a modular, filament-like structure adjusts its effective length in response to a tuneable external field. Unlike conventional actuators composed of continuous or elastic materials, the present system consists of discrete conductive microparticles joined by deformable liquid bridges, resulting in a highly adaptable structure with field-controlled cohesion. From a physical standpoint, this experiment illustrates a dynamic interplay between electrostatic forces and capillary-mediated cohesion, where voltage governs not only particle extraction but also structural stability and internal tension. The ability to control the shape and mechanical response of a particle-based structure post-formation opens new possibilities for reconfigurable microstructures and programmable soft elements. Potential applications include field-tuneable interconnects, reversible microgrippers, or lightweight actuators for soft robotics and adaptive electronics. Because no moving parts are required, the system offers a compact and elegant solution for voltage-driven shape control in confined or sensitive environments.

Declaration

During the preparation of this manuscript, we used an AI-powered writing assistant (Grammarly) solely to improve readability and language clarity. All content was thoroughly reviewed and edited by the authors after the use of this tool. We take full responsibility for the final content of this publication.

Author contributions

Z. Rozynek initiated the project, contributed to the formulation of key scientific hypotheses, and co-designed all experiments. He conducted the experiments presented in Figs. 4c, 9b, 12–16, and S3, as well as in Movies 1 and 8–11. He also co-performed the experiments shown in Figs. 2 and 6. Y. Harkavyi formulated part of the scientific hypotheses, co-designed all experiments, and performed the experiments and simulations whose results are shown in Figs. 4, 6, 8, 9a, 9c, 9d, 10, 11, 12a, and S2, as well as in Movies 3–7. He also co-performed the experiments presented in Figs. 2, 5 and 7. G. Tiwari conducted experiments presented in Figs. 5, 7 and Movie S2. She also co-performed preliminary experiments for the Figs. 6, 8, 11, and Movie S5. Z. Rozynek wrote the first draft of the manuscript. All authors contributed to discussions leading to the final version of the manuscript. Z. Rozynek managed the submission and review process.

CRediT authorship contribution statement

Y. Harkavyi: Writing – review & editing, Visualization, Validation, Software, Methodology, Investigation, Formal analysis, Data curation, Conceptualization. **G. Tiwari:** Writing – review & editing, Visualization, Investigation. **Z. Rozynek:** Writing – original draft, Visualization, Validation, Supervision, Resources, Project administration, Methodology, Investigation, Funding acquisition, Formal analysis, Data curation, Conceptualization.

Declaration of competing interest

The authors declare that they have no known competing financial interests or personal relationships that could have appeared to influence the work reported in this paper.

Acknowledgments

This research was funded by the Polish National Science Centre (NCN) through the OPUS program (grant numbers: 2019/33/B/ST5/00935 and 2022/45/B/ST5/03529). The contributions of G. Tiwari were funded by NCN under the SONATA 15 call (project number: 2019/35/D/ST5/03613). We gratefully acknowledge CADENAS P.S.A. (Poland) for providing essential research infrastructure, key technical equipment, and specialized materials used in multiple experimental

procedures. Selected parts of the research, including the development and demonstration of application-related experiments, were conducted using resources and support provided by the company.

Appendix A. Supplementary data

Supplementary data to this article can be found online at https://doi.org/10.1016/j.matdes.2025.114160.

Data availability

Data will be made available on request.

References

[1] M.D. Barnes, S.M. Mahurin, A. Mehta, B.G. Sumpter, D.W. Noid, *Phys. Rev. Lett.* 88 (1) (2001) 015508, https://doi.org/10.1103/PhysRevLett.88.015508.
[2] V.N. Astratov, J.P. Franchak, S.P. Ashili, *Appl. Phys. Lett.* 85 (23) (2004) 5508–5510, https://doi.org/10.1063/1.1832737.
[3] Y. Zhang, W. Jiang, T. Gu, J. Han, B. Lei, L. Wang, H. Liu, L. Yin, B. Chen, Y. Shi, *Langmuir* 36 (39) (2020) 11546–11555, https://doi.org/10.1021/acs.langmuir.0c02021.
[4] K.W. Allen, A. Darafsheh, F. Abolmaali, N. Mojaverian, N.I. Limberopoulos, A. Lupu, V.N. Astratov, A.P. Letters, *Appl. Phys. Lett.* 105 (2) (2014), https://doi.org/10.1063/1.4890595.
[5] T. Mitsui, Y. Wakayama, T. Onodera, T. Hayashi, N. Ikeda, Y. Sugimoto, T. Takamasu, H. Oikawa, *Adv. Mater.* 22 (28) (2010) 3022–3026, https://doi.org/10.1002/adma.201000155.
[6] E. Falcon, B. Castaing, M. Creyssels, *Eur. Phys. J. B* 38 (3) (2004) 475–483, https://doi.org/10.1140/epjb/e2004-00142-9.
[7] P. Béquin, V. Tournat, *Granul. Matter* 12 (4) (2010) 375–385, https://doi.org/10.1007/s10035-010-0185-8.
[8] C. Stephenson, A. Hubler, *Sci. Rep.* 5 (2015) 15044, https://doi.org/10.1038/srep15044.
[9] W. Ahn, X. Zhao, Y. Hong, B.M. Reinhard, *Sci. Rep.* 6 (2016) 22621, https://doi.org/10.1038/srep22621.
[10] Y. Hong, W. Ahn, S.V. Boriskina, X. Zhao, B.M. Reinhard, *J. Phys. Chem. Lett.* 6 (11) (2015) 2056–2064, https://doi.org/10.1021/acs.jpclett.5b00366.
[11] B. Yuan, L. Cademartiri, *J. Mater. Sci. Technol.* 31 (6) (2015) 607–615, https://doi.org/10.1016/j.jmst.2014.11.015.
[12] D. Nishiguchi, J. Iwasawa, H.-R. Jiang, M. Sano, *New J. Phys.* 20 (1) (2018) 015002, https://doi.org/10.1088/1367-2630/aa9b48.
[13] B. Yigit, Y. Alapan, M. Sitti, *Adv. Sci.* 6 (6) (2019) 1801837, https://doi.org/10.1002/advs.201801837.
[14] O.D. Velev, S. Gupta, *Adv. Mater.* 21 (19) (2009) 1897–1905, https://doi.org/10.1002/adma.200801837.
[15] F. Dutka, Z. Rozynek, M. Napiorkowski, *Soft Matter* 13 (27) (2017) 4698–4708, https://doi.org/10.1039/c7sm00396j.
[16] Z. Rozynek, M. Han, F. Dutka, P. Garstecki, A. Józefczak, E. Luijten, *Nat. Commun.* 8 (2017) 15255, https://doi.org/10.1038/ncomms15255.
[17] Z. Rozynek, Y. Harkavyi, K. Giżyński, *Mater. Des.* **2022,** *223*. DOI 10.1016/j.matdes.2022.111233.
[18] Z. Rozynek, A. Magdziarz, U.S. Patent No. 11,856,709. **2023**.
[19] Y. Harkavyi, K. Giżyński, Z. Rozynek, *Soft Matter* (2025), https://doi.org/10.1039/D4SM01499E.
[20] Z. Rozynek, Y. Harkavyi, Ø.G. Martinsen, K. Giżyński, *Mater. Des.* 253 (2025) 113985, https://doi.org/10.1016/j.matdes.2025.113985.
[21] S. Gangwal, A. Pawar, I. Kretzschmar, O.D. Velev, *Soft Matter* 6 (7) (2010) 1413–1418, https://doi.org/10.1039/b925713f.
[22] B. Bharti, G.H. Findenegg, O.D. Velev, *Sci. Rep.* 2 (2012) 1004, https://doi.org/10.1038/srep01004.
[23] H.R. Vutukuri, A.F. Demirors, B. Peng, P.D. van Oostrum, A. Imhof, A. van Blaaderen, *Angew. Chem. Int. Ed.* 51 (45) (2012) 11249–11253, https://doi.org/10.1002/anie.201202592.
[24] D. Morales, B. Bharti, M.D. Dickey, O.D. Velev, *Small* 12 (17) (2016) 2283–2290, https://doi.org/10.1002/smll.201600037.
[25] F. Martinez-Pedrero, A. Ortiz-Ambriz, I. Pagonabarraga, P. Tierno, *Phys. Rev. Lett.* 115 (13) (2015) 138301, https://doi.org/10.1103/PhysRevLett.115.138301.
[26] B. Bharti, F. Kogler, C.K. Hall, S.H.L. Klapp, O.D. Velev, *Soft Matter* 12 (37) (2016) 7747–7758, https://doi.org/10.1039/C6SM01475E.
[27] Z. Cenev, H. Zhang, V. Sariola, A. Rahikkala, D. Liu, H.A. Santos, Q. Zhou, *Adv. Mater. Technol.* 3 (1) (2018) 1700177, https://doi.org/10.1002/admt.201700177.
[28] R.R. Collino, T.R. Ray, R.C. Fleming, C.H. Sasaki, H. Haj-Hariri, M.R. Begley, *Extreme Mech. Lett.* 5 (2015) 37–46, https://doi.org/10.1016/j.eml.2015.09.003.
[29] H. Shen, K. Zhao, Z. Wang, X. Xu, J. Lu, W. Liu, X. Lu, *Micromachines* 10 (12) (2019) 882.
[30] W.H. Yeo, J.H. Chung, Y.L. Liu, K.H. Lee, Biosensing (2008) 7035, https://doi.org/10.1117/12.795098.
[31] J. Tang, B. Gao, H. Geng, O.D. Velev, L.C. Qin, O. Zhou, *Adv. Mater.* 15 (16) (2003) 1352–1355, https://doi.org/10.1002/adma.200305086.
[32] W.H. Yeo, F.L. Chou, K. Oh, K.H. Lee, J.H. Chung, *J. Nanosci. Nanotechnol.* 9 (12) (2009) 7288–7292, https://doi.org/10.1166/jnn.2009.1773.
[33] J. Ma, J. Tang, Q. Cheng, H. Zhang, N. Shinya, L.C. Qin, *Sci. Technol. Adv. Mater.* 11 (6) (2010) 065005, https://doi.org/10.1088/1468-6996/11/6/065005.
[34] J.H. Han, G.L. Paulus, R. Maruyama, D.A. Heller, W.J. Kim, P.W. Barone, C.Y. Lee, J.H. Choi, M.H. Ham, C. Song, C. Fantini, M.S. Strano, *Nat. Mater.* 9 (10) (2010) 833–839, https://doi.org/10.1038/nmat2832.
[35] R. Maruyama, Y.W. Nam, J.H. Han, M.S. Strano, *Curr. Appl Phys.* 11 (6) (2011) 1414–1418, https://doi.org/10.1016/j.cap.2011.06.026.
[36] J.H. Shin, K. Kim, T. An, W. Choi, G. Lim, *Nanoscale Res. Lett.* 11 (1) (2016) 385, https://doi.org/10.1186/s11671-016-1600-9.
[37] S.J. Kahng, J.H. Kim, J.H. Chung, *Sensors (Basel)* 17 (1) (2016) 1–17, https://doi.org/10.3390/s17010017.
[38] K. Yiannacou, V. Sariola, *Adv. Intell. Syst.* 5 (9) (2023) 2300058, https://doi.org/10.1002/aisy.202300058.
[39] S. Xin, K.A. Deo, J. Dai, N.K.R. Pandian, D. Chimene, R.M. Moebius, A. Jain, A. Han, A.K. Gaharwar, D.L. Alge, *Sci. Adv.* 7 (42) (2021), https://doi.org/10.1126/sciadv.abk3087 eabk3087.
[40] W. He, N. Senbil, A.D. Dinsmore, *Soft Matter* 11 (25) (2015) 5087–5094, https://doi.org/10.1039/c5sm00245a.
[41] Z. Rozynek, A. Magdziarz, Process of fabricating a beaded path on the surface of a substrate, a system for fabricating such a path, use thereof, and a kit (EP3831171B1). **2022**.

——Scientific Paper III——

Experimental and FEM simulation study of compressive deformation of solder microballs and particle chains

Harkavyi Y., Giżyński K. And Rozynek Z.

Soft Matter, 2025, 21, 4393

Soft Matter

PAPER

Cite this: *Soft Matter*, 2025, 21, 4393

Experimental and FEM simulation study of compressive deformation of solder microballs and particle chains†

Y. Harkavyi, [a] K. Giżyński [b] and Z. Rozynek *[ac]

Beaded microstructures, formed by side-by-side alignment of spherical microparticles, offer a promising approach for creating micropaths with pre-determined electrical and thermal conductivity. Post-processing through mechanical compression effectively modulates the structural and conductive properties, enabling precise control over conductivity by applying defined compressive forces and calibrating strain levels. To investigate the mechanical properties of these beaded structures, this study begins with an in-depth analysis of the compressive response of unconstrained individual solder microballs, representative of malleable soft materials. The study examines the influence of particle size, engineering strain rate, and temperature on compressive force and deformation characteristics. Results from single-particle experiments are then systematically compared with those from beaded structures, revealing distinct mechanical responses. In particular, particle chains require higher compressive forces due to lateral constraints introduced by neighbouring particles, with differences in force values dependent on strain level and also on the number of microballs in the chain. FEM simulations were employed to model stress distributions, contact pressures, and deformation profiles, extending the analysis to deformation scenarios beyond experimental limits. The Johnson–Cook (J–C) model proved to be a robust predictor of compressive behaviour under varying strain rates and elevated temperatures, with temperature exerting a more significant influence than strain rate. Parameterization of the model allowed for accurate replication of empirical scaling behaviours, with strain rate and temperature dependencies from the J–C model closely matching experimental observations. These results expand our understanding of single solder microparticle deformation and offer valuable insights into the deformation of beaded structures, which could be beneficial for practical applications such as the fabrication of electronic components.

Received 18th December 2024,
Accepted 3rd April 2025

DOI: 10.1039/d4sm01499e

rsc.li/soft-matter-journal

Introduction

Beaded micropaths, consisting of side-by-side aligned microparticles, possess intriguing properties, including mesoscale periodicity and a high surface-to-volume ratio. Such structures—resembling a pearl necklace by appearance—may also conduct electricity very effectively, thus serving as a new type of conductive micro-track.[1] The key to achieving high electrical conductivity in these structures lies in ensuring robust interconnections between the individual particles. To accomplish this, various post-processing techniques have been explored, including contact heating,[2] laser treatment,[3] and electric-current-induced-fusing,[4] each employing heat in a distinct manner.

For malleable materials, which can be easily shaped without breaking, uniaxial mechanical compression can be a straightforward alternative method. Pressing the line of microparticles deposited on a substrate, in a direction normal to the surface of the substrate, leads to an increase in contact between adjacent particles. This process enables the conduction of electric current, with the resultant electrical conductivity depending on the level of compressive strain applied;[1] see also exemplary experimental results in Fig. S1 (ESI†).

From a practical standpoint, understanding the specific compressive force values required for a given level of compression is essential for several reasons, including process scaling in different operating conditions, improving the durability of microstructures, enhancing repeatability and consistency in production, and facilitating adaptation to different materials. This normal force (F_N) is intrinsically dependent on particle size, the quantity of particles undergoing compression, and

[a] *Faculty of Physics and Astronomy, Adam Mickiewicz University, Uniwersytetu Poznańskiego 2, 61-614 Poznań, Poland. E-mail: zbiroz@amu.edu.pl*
[b] *Institute of Physical Chemistry, Polish Academy of Sciences, Kasprzaka 44/52 01-224 Warsaw, Poland*
[c] *CADENAS P.S.A., Prof. Sylwestra Kaliskiego 24, 85-796 Bydgoszcz, Poland*

† Electronic supplementary information (ESI) available. See DOI: https://doi.org/10.1039/d4sm01499e

material properties. Additionally, it is influenced by the compressive strain (ε), strain rate ($\dot{\varepsilon}$), and process temperature (T).

In this research, we first investigate the mechanical properties of an individual spherical microparticle, focusing on its material mechanics and rheological properties to provide foundational insights. We then examine the more complex interactions within a single-particle-thick structure, where particles are aligned side-by-side to form a beaded path. Solder materials, which are readily available and widely used in electronics, are our focus here, serving as representative examples of malleable soft materials. Our study utilizes microspheres ranging in size from 200 to 760 μm, which fall within the typical range used for these particles in various electronic applications.

Numerous studies have examined the deformation of individual solder balls[5–12] and microballs composed of other conductive and non-conductive materials,[13–15] though typically within limited ranges of deformation and temperature. Our work broadens this research by investigating microspheres under more extensive compressive strains and temperatures, providing a deeper understanding of the material's dynamic properties under complex interactions.

In the case of more complex systems, such as chains of adjacent microparticles, we found no comprehensive studies on beaded paths, where side-by-side aligned spherical particles undergo a distinct deformation process compared to single-particle compression. This difference arises because particles in a path have limited freedom to deform along the chain's direction, leading to uneven lateral deformation. In contrast, an isolated spherical particle, unconstrained by neighbours, can deform more uniformly in all lateral directions under compression. Consequently, the distribution of forces and pressures in a particle chain differs significantly from that in a single particle. It remains uncertain how force values compare between physically constrained and unconstrained microspheres across a broad range of compressive strains. We hypothesize that compressing particles in a chain will require greater force than compressing the same number of separated particles, with this difference becoming more pronounced at higher compression levels and with more particles in the chain. This study aims to verify this hypothesis through experimental research and computer simulations, quantifying the compression differences between these two microparticle arrangements. To facilitate collaboration and progress in materials research, all simulation files are available in the ESI,† inviting further analysis and validation by the scientific community.

Methods

Materials and experimental setups

In this study, we used both leaded ($Sn_{63}Pb_{37}$) and lead-free ($Sn_{96.5}Ag_3Cu_{0.5}$) solder ball microparticles sourced from PMTC, Taiwan, *via* Reball, Poland. The particle sizes ranged from 200 to 760 μm, with a tolerance of ±15 μm. These particles exhibit a melting point of 183 °C for the leaded solder material, and 217 °C for the lead-free solder material.

The mechanical properties of the solder balls were analysed using an MCR302e Anton Paar rheometer configured in a plate-plate setup, as depicted in Fig. 1a. This equipment allowed for the precise measurement and control of normal force, compressive strain, and compression velocity. The rheometer's specifications include a maximum normal force capacity of

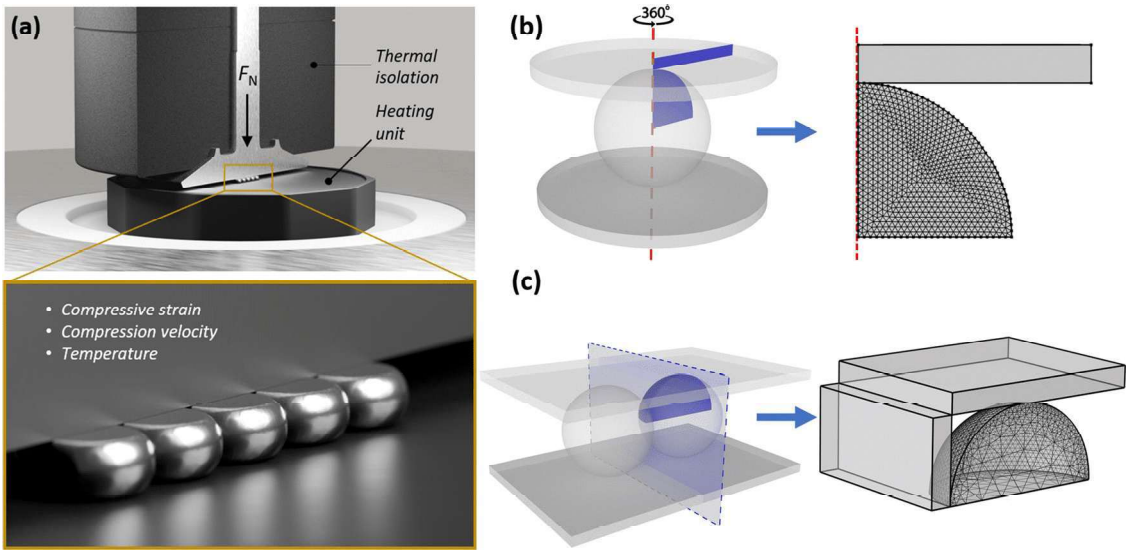

Fig. 1 (a) 3D computer graphics of the experimental setup. This setup is used for measurements of a particle/particle chain under mechanical compression. The thermal insulation and compressing shaft are presented in cross-section to enhance the clarity and comprehensibility of the setup. The black arrow indicates the direction of compression. During the experiments, temperature, compression rate, and normal force were the variables. (b) 2D geometry and triangular mesh used in FEM studies on the compression of a single sphere. Taking advantage of system symmetries, the model represents a single sphere constrained between two rigid plates. (c) 3D geometry and tetrahedral mesh applied in simulations involving two or more compressed spheres. In the left image, the vertically positioned plate serves as a symmetry plane, while the right image illustrates the actual modelled system.

50 N and a maximum compression velocity of 1 mm s^{-1}. For particle positioning, we consistently placed the solder balls in the central part of the measuring shaft. When aligning the particles in a line, a minimal quantity of ethanol was applied to facilitate the particles' proximity and physical contact. This approach utilized attractive capillary forces arising from liquid bridges formed between neighbouring particles, as detailed in ref. 16. Following the evaporation of the solvent, the testing was initiated.

Temperature control during the experiments was achieved using a Peltier device with active heating capabilities, allowing precise adjustment from −25 to 220 °C. To reduce heat loss from the measuring shaft, thermal foam insulation was applied (see Fig. 1a). Prior to each experiment, the position along the compression direction was calibrated by lowering the shaft until it contacted the heated base plate, establishing the zero position. Additionally, the normal force was zeroed by monitoring any increase in force during the heating phase, caused by the thermal expansion of the metal shaft. Once the normal force stabilized, both the 'zero gap' between the measuring shaft and the base, as well as the normal force itself, were reset to ensure accurate measurements. Subsequently, the shaft was raised, and the solder ball microparticles were swiftly positioned on the lower base of the rheometer for measurement. After positioning, the shaft was lowered to a height corresponding to the diameter of the measured particles. Typically, a waiting period of approximately one minute was allowed for the stabilization of the micro-particles' temperature and their surroundings before initiating the designated measurement program.

The data represented as closed circles in Fig. 2–4 is processed experimental data, with each experimental measurement repeated three times. Due to the use of a stepper motor, the measured deformation was slightly different for each experiment (though the differences were practically negligible). To average the data, a polynomial curve was fitted to the raw data points, ensuring identical values on the *X*-axis. In the final step, the data were averaged. Standard deviations were not added to Fig. 2–4 for clarity but are included in Fig. 5.

Theoretical model

Theoretical calculations were performed using COMSOL Multiphysics 6.1 with structural mechanics and nonlinear structural materials modules. Particle deformation was modelled using the Solid Mechanics interface in a time-dependent study. This approach facilitated accurate simulations of particle behaviour under load, focusing on key metrics such as contact area, deformation profiles, and applied forces.

To analyse the compression behaviour of a single sphere, a 2D axisymmetric model was utilized, as illustrated in Fig. 1b. This approach simplified the geometry, significantly reducing computational time by leveraging system symmetry. The pressing plate was modelled as a rigid domain with a prescribed displacement, determined by the product of constant velocity and time. The particle mesh was composed of triangular elements, with the element size set to the predefined 'extremely fine' setting. Manual adjustments to the minimum element size were applied to ensure precision. The pressing plate was meshed with a single brick element, as shown in the right panel of Fig. 1b.

The solder particle, composed of $Sn_{63}Pb_{37}$ alloy, was treated as a plastic material. Three material hardening models were implemented and compared: perfect plastic, Ludwik, and Johnson–Cook (J–C). The simplest among these, the perfectly plastic model describes a material that deforms elastically up to a specific yield stress value, referred to as the initial yield stress (σ_γ). Beyond this point, the material deforms plastically without any further increase in stress. This behavior can be expressed mathematically as:

$$\sigma_{eq}(\varepsilon_{eq}) = E{\cdot}\varepsilon_{eq} \text{ for } \varepsilon_{eq} \leq \varepsilon_\gamma,$$

$$\sigma_{eq}(\varepsilon_{eq}) = \sigma_\gamma \text{ for } \varepsilon_{eq} > \varepsilon_\gamma$$

where σ_{eq} is the equivalent (local) plastic stress, ε_{eq} is the equivalent (local) plastic strain, E is Young's modulus (elastic modulus), σ_γ is the yield stress, $\varepsilon_\gamma = \sigma_\gamma/E$ is the yield strain.

A more comprehensive model is the Ludwik model, which includes strain-hardening effects and is given by the following expression:

$$\sigma_{eq} = \sigma_y + k{\cdot}\varepsilon_{eq}^n,$$

where k is the hardening modulus, and n is the strain-hardening exponent. Lastly, the model most extensively used here, was the J–C model, which extends the Ludwik model by incorporating both strain-rate and temperature effects into the deformation description. It is expressed by the following equation:

$$\sigma_{eq} = \left(\sigma_y + k \cdot \varepsilon_{eq}^n\right)\left(1 + C\ln\left(\frac{\dot{\varepsilon}_{eq}}{\dot{\varepsilon}_{ref}}\right)\right)(1 - T^{*m}),$$

where C is the strain-rate sensitivity coefficient, $\dot{\varepsilon}_{eq}$ is the equivalent (local) plastic strain rate, $\dot{\varepsilon}_{ref}$ is the reference strain rate, T^* is the dimensionless temperature and m is the temperature exponent.

It is important to note that in the COMSOL simulations, σ represents the equivalent local stress (not the global stress that would be calculated as the average stress across the entire material or structure). Equivalent stress, often referred to as von Mises stress in finite element analysis, is a scalar value derived from the stress tensor at each point in the material. Similarly, the equivalent plastic strain rate, $\dot{\varepsilon}_{eq}$, represents the rate of change of plastic deformation over time, specific to each mesh element. Therefore, the reference strain rate parameter should not be treated as a global parameter, a common mistake that can occur when modelling in COMSOL. To clarify, we denote the reference strain rate as $\dot{\varepsilon}_{eq,ref}$ to emphasize that it is a local value, ensuring a constant logarithmic relation for a specific compression rate. This raises the question of how to define and input $\dot{\varepsilon}_{eq,ref}$, into COMSOL, as it is a matrix of values in space and time rather than a single value defined by the engineering strain rate as $\dot{\varepsilon} = \upsilon/D$. Our solution was to manually implement the J–C model equation in COMSOL, where we directly specify the values obtained from the logarithmic ratio of the engineering strain rate to the reference engineering strain rate. We can do this because we assume in our calculations that the deformation shape is independent of the strain

rate, *i.e.*, the simulated deformation shapes of the initially spherical sample remain the same regardless of the compression speed. This assumption is approximately consistent with real conditions. Therefore, we do not require a matrix of $\dot{\varepsilon}_{eq,ref}$ values, as we know that each value in this matrix will change in the same way, expressed as the logarithm of $\dot{\varepsilon}_{eng}/\dot{\varepsilon}_{eng,ref}$. Thus, the final equation for the J–C model used has the following formula:

$$\sigma_{eq} = \left(\sigma_{y,ref} + k_{ref} \cdot \varepsilon_{eq}^{n_{ref}}\right)\left(1 + C\ln\left(\frac{\dot{\varepsilon}_{eng}}{\dot{\varepsilon}_{eng,ref}}\right)\right)(1 - T^{*m}).$$

Additionally, we discovered that the J–C model in COMSOL version 6.1 does not correctly simulate stress values for structures compressed at rates slower than the reference strain rate. Specifically, regardless of how low the strain rate was set, the simulation yielded stress values as if the reference strain rate had been applied. This behaviour results from COMSOL's implementation of the model, where the argument of the logarithmic function is shifted by 1, $\ln(1 + \dot{\varepsilon}_{eq}/\dot{\varepsilon}_{ref})$ to enhance calculation stability. Ultimately, we resolved the convergence issue by manually implementing the modified J–C model, as described above.

Each model predicted the particle's shape, contact area with the pressing plate, and applied load. The accuracy of these predictions was validated by comparing simulation results to experimental data (see Fig. 6b in the Results section).

Once the J–C model (including isotropic hardening and Coulomb friction between the pressing plate and the surface of each individual sphere, with a friction coefficient of 0.15) was identified as the most accurate for predictions (see Section 3.2 for detailed reasoning), the Optimization Module, coupled with a parametric study, was used to fine-tune the model parameters to match the experimental data. The optimization study using the Nelder–Mead method was conducted in cycles, with the optimality tolerance parameter set to 0.001. In each cycle, a parametric sweep was performed, varying simulation input parameters such as strain rate or temperature. After each cycle, the discrepancy between the experimental data and the simulated curves was estimated based on residual sum of squares (RSS). The ultimate goal of optimization was to minimize the summed RSS for the considered experimental parameter values. Model parameters were then adjusted, and the next cycle commenced. This iterative process continued until the optimality tolerance was achieved (Fig. S2 shows the reduction in the objective function across cycles, ESI†). The final set of optimized parameters was applied to all subsequent simulations.

Due to the limitations of the 2D axisymmetric model for single-particle scenarios, interactions between multiple particles in contact were simulated using a 3D model with the symmetry-based geometry shown in Fig. 1c. To further reduce computational complexity, one-quarter of the system was simulated, leveraging both the contact plane symmetry and the symmetry of the compressed objects.

Results and discussion

Laboratory results for single-ball compression

We begin our measurements by compressing individual solder balls and studying how the compressive force (F_N)–strain (ε) relation depends on ball diameter (d), engineering strain rate ($\dot{\varepsilon}$), and solder ball temperature (T).

Fig. 2 illustrates the relation between applied compressive force and compressive strain for single solder balls of varying diameters. The strain is defined as $\varepsilon = \Delta L/L_0 \times 100$, where ΔL is the change in length, *i.e.*, axial shortening due to compression, and L_0 is the initial length of the sample, which in this case is the ball diameter. The experiment involved compressing the solder balls at a constant engineering strain rate of 0.005 s^{-1} ($\dot{\varepsilon} = v/d$, where compression velocity v is divided by sphere diameter d), with each trial lasting approximately 3 minutes.

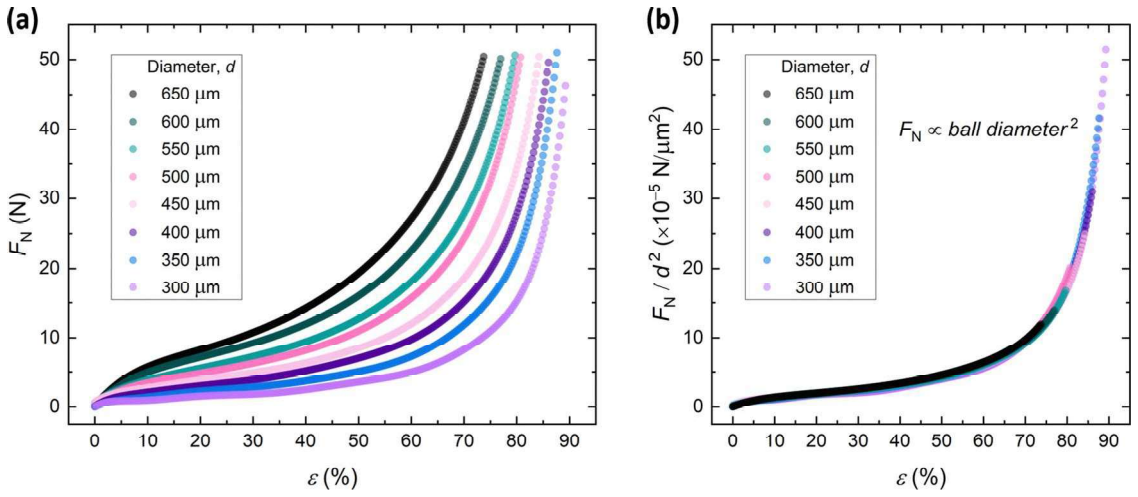

Fig. 2 Compression behaviour of $Sn_{63}Pb_{37}$ single solder balls. (a) Force–strain relation: graph illustrating applied force (F_N) *versus* compressive strain (ε) for single solder balls of different sizes. (b) The normalized (by ball size) force–strain relation. A constant strain rate of 0.005 s^{-1} was used. The presented data are processed experimental results, with each experimental measurement repeated three times (for details, see the Methods section).

As shown in Fig. 2, the compressive force increases rapidly at low strain values (a few percent), then grows more gradually at intermediate strains (up to about 60%), and finally rises sharply at higher strains, exhibiting a near-divergent trend as strain approaches 100%. The changes in F_N values are the result of changes in the contact area A_1 (plate-ball contact), the transition from elastic to plastic deformation, and the strain hardening. Additionally, at high strain values, friction is likely becoming significant. As the contact area between the deformed particle and the plates increases, the amount of material sliding along the contact surface grows, and the compressive force applied perpendicular to the contact surfaces increases, all of which contribute to an increase in tangential friction.

When compressing a spherical bead, the stress σ induced by the force F_N is distributed over the contact area perpendicular to the applied force. In the purely elastic regime (strains $<1\%$), Hertzian contact theory predicts a scaling of $F_N \sim d^{1/2}x^{3/2}$, where x represents the contact radius. However, in the plastic deformation regime relevant to our study (1–80% strain), the force scales as $F_N \sim d^2$. This transition occurs because plastic flow constrains further stress increase, shifting the governing mechanism from elastic deformation to contact area dominance. Specifically, the contact area grows proportionally to d^2, as opposed to the Hertzian model, which assumes elastic material behaviour. In Fig. 2b, the experimental results are normalized by dividing F_N values by d^2 for each data series. The resulting data collapse confirms the quadratic scaling relationship, validating that the plastic regime governs the deformation behaviour at these strain levels.

In the subsequent experiment, force–strain characteristics were determined for different strain rates. Notably, force is reported instead of stress, as calculating stress is challenging for a spherical object, requiring assumptions about which cross-sectional area to consider. From an experimental perspective, measuring force provides a more direct parameter. Fig. 3a presents the experimental data for five measurements, where the engineering strain rate (defined as the velocity of the compressive rod moving only in the Z-direction divided by the sphere diameter) varied from 3.1×10^{-5} to 1.5 s^{-1}. For microparticles with a size of 650 μm, this corresponds to a pressing plate displacement speed ranging from 0.025 to 1000 μm s^{-1}. At the lowest strain rate, the experiment lasted 7 hours, allowing for deformation up to 84%. In contrast, at the highest strain rate, the experiment lasted approximately 0.4 seconds, with deformation reaching 64%, limited by the maximum permissible force of 50 N imposed by the measurement apparatus.

Fig. 3b presents the same force–strain relation as Fig. 3a, with the additional normalization of the force value. We found that within the studied range of strain rate values, a power law with an exponent of 0.12 can describe the strain rate dependence of the compressive force. Nevertheless, this dependence is very weak, suggesting that in practical industrial applications, solder microparticles can be compressed at higher strain rates without a significant increase in force. This is particularly relevant for calendering or rolling processes, where typical strain rates during compression range from 0.01 to 10 s^{-1}. However, if the compressive force – and thus the pressure at the particle–substrate interface – becomes too high, leading to substrate indentation or cracking, the compression speed should be reduced. Alternatively, increasing the process temperature remains an option.

In the next experiment, we investigate how temperature (T) affects the compressive force–strain relationship. A series of experiments were conducted over a broad temperature range, from 5 °C to 210 °C. Note that the melting temperature of $Sn_{63}Pb_{37}$ solder is approximately 183 °C, thus the final measurement involves the compression of a molten solder droplet.

The experimental data presented in Fig. 4a reveal a strong temperature-dependent trend in the mechanical properties of the solder material, *i.e.*, the material's resistance to deformation decreases with increasing temperature. This behaviour can be represented mathematically using a temperature-dependent

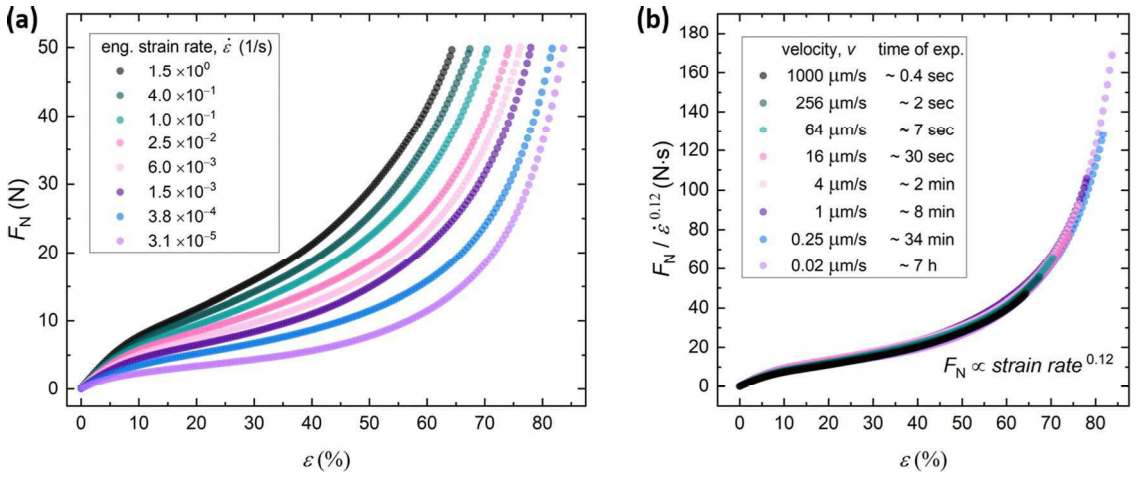

Fig. 3 Strain rate dependency of 650-μm single $Sn_{63}Pb_{37}$ solder balls. (a) Force–strain relation at different strain rates varying from 3.1×10^{-5} to 1.5 s^{-1}. (b) The normalized force–strain relation reveals that a simple power-law relation can be used to scale the force. The power-law exponent of 0.12 indicates a very weak dependence of force on strain rate.

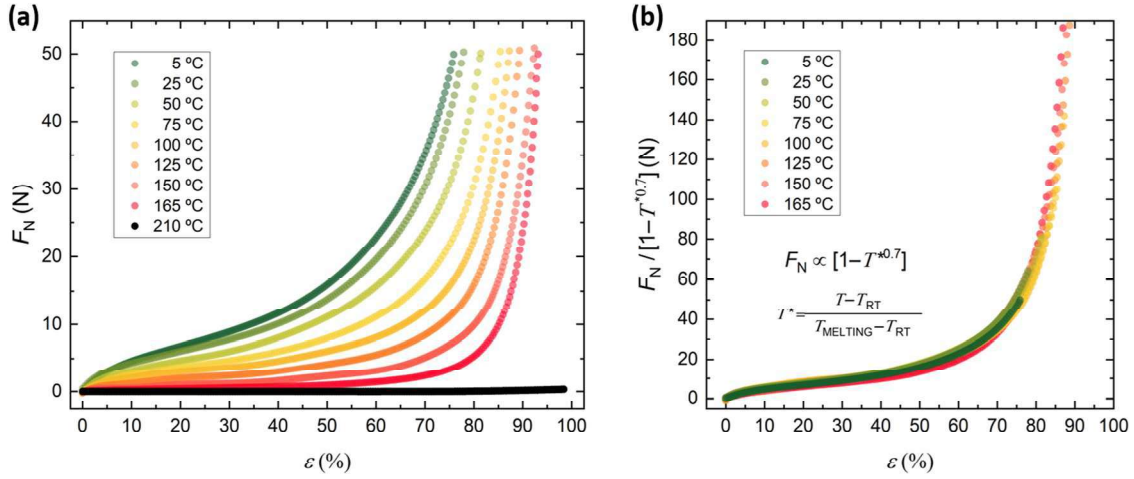

Fig. 4 Temperature dependency of 650-μm single $Sn_{63}Pb_{37}$ balls. (a) Force–strain relation at different temperatures in the range 5–210 °C. A constant strain rate of 4.0×10^{-4} s^{-1} was used. (b) The normalized force–strain relation reveals that a temperature-dependent scaling factor $1 - T^{*m}$ can be used to describe the behavior, with the parameter m determined to be 0.7. The results indicate a strong dependence of force on temperature.

scaling factor. Specifically, the force–strain curves for different temperatures were normalized using a factor that accounts for thermal softening: $1 - T^{*m}$, where $T^* = (T - T_{RT})/(T_{melt} - T_{RT})$. This relation is widely used in material science to predict the performance of materials under varying thermal conditions,[17] where T_{RT} is the reference temperature used as a baseline for normalizing the temperature T in relation to the melting temperature T_{melt}. To determine the parameter m, we tested various values and observed which value resulted in the best collapse of the data onto a single curve. Through this empirical process, we found that the value of m is approximately 0.7. In Fig. 4b, the scaled data from Fig. 4a is plotted. In Fig. 4b, we did not plot the results for the experiment conducted at 210 °C, which is above the melting temperature. For the molten solder droplet, F_N is nearly constant and is in the range of mN for strain values up to around 70%, after which it starts to increase, reaching 0.3 N at a strain of 95%. This is still very small to be observed in Fig. 4a.

In this section of the research, we identified an empirical relation between the compressive force and the parameters of particle diameter, compression strain rate, and process temperature, which can be expressed as: $F_N \propto d^2 \cdot \dot{\varepsilon}^{0.12} \cdot [1 - T^{*0.7}]$.

In the final part of the laboratory studies on the compression of a single microparticle, we compare two solder particle materials, namely the leaded alloy $Sn_{63}Pb_{37}$ and the lead-free alloy SAC305 (96.5% Sn, 3% Ag, 0.5% Cu). Although $Sn_{63}Pb_{37}$ remains widely used in many applications due to its excellent wetting properties and reliable joint strength, the lead-free solders are increasingly favoured. This shift is driven by environmental and health regulations, as well as the need for sustainable alternatives. Spherical microparticles, each 650 μm in diameter were compressed at strain rates of 1.5×10^{-3} s^{-1} and 4×10^{-1} s^{-1} at room temperature. The experiment for each type of microparticle was repeated three times.

Fig. 5 illustrates the averaged results along with the standard deviation. As shown in the graph, the leaded particles deform more easily, requiring slightly less force. This is expected, given

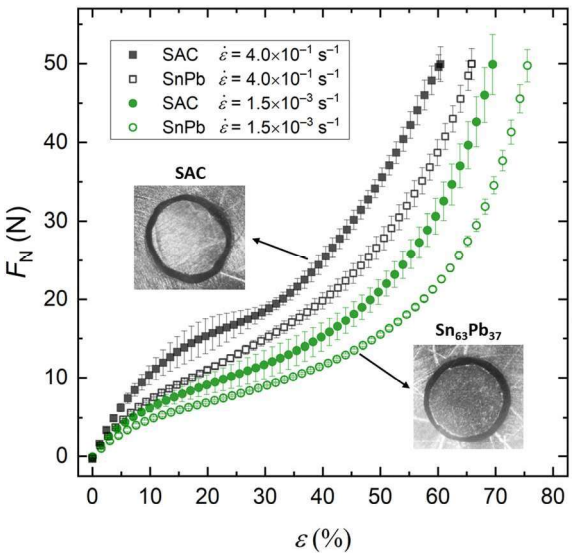

Fig. 5 Comparison of compression behaviour of leaded ($Sn_{63}Pb_{37}$) and lead-free (SAC305) solder beads. The force–strain relation shows that the leaded particles deform more easily, requiring slightly less force. The measurements of lead-free particles were less consistent, as evidenced by the error bars, which are larger for measurements of lead-free particles at strain rates of 1.5×10^{-3} and 4×10^{-1} s^{-1}. The inset images show views taken from above in the direction of compression. The contact area of the compressed lead-free particles is typically less spherical than that of the leaded solder particles.

that leaded solders generally exhibit lower yield strength and greater ductility compared to lead-free solders[18,19] due to the presence of lead, which imparts greater malleability and reduces the resistance to deformation. Additionally, stress–strain curves for these experiments are provided in Fig. S3 (ESI†).

It is interesting to note that for the measurement of lead-free microparticles, there is consistently a greater spread in the measurements, as shown by the error bars. Under the microscope, the contact area of the compressed lead-free particles

always appears less spherical, displaying more irregular deformation shapes. The greater spread and irregular deformation in lead-free microparticles like SAC305 can be explained by the differences in microstructure. Lead-based solders (*e.g.*, $Sn_{63}Pb_{37}$) are eutectic alloys with a uniform structure that leads to more regular, predictable deformation. SAC305, a hypoeutectic alloy, has a heterogeneous structure with tin-rich phases and hard intermetallic compounds (Ag_3Sn, Cu_6Sn_5), resulting in uneven mechanical behaviour and less spherical deformation.[20]

Two-dimensional axisymmetric simulation results of single ball compression

Numerical simulations were conducted using the finite element analysis methodology. The primary goals were to verify experimental results and ensure the accuracy of the obtained data. Additionally, simulations helped extend the range of deformations, particularly for larger or rapidly compressed spheres, where equipment limitations prevented compressive forces exceeding 50 N. The simulations also provided data that are challenging to acquire in laboratory settings, such as true strain rates (as opposed to engineering strain rates), enabled parametric analyses to identify appropriate material parameters, and allowed examination of the impact of friction on the results.

We will begin with several general simulations to illustrate the differences between commonly used compression models for microballs of various materials. Fig. 6 shows the results for a lead solder microparticle with a size of 650 μm subjected to compression with an engineering strain rate of 0.1 s^{-1} (arbitrarily chosen). The simulations started with perfect plastic material model. In general, when compressing a material with a constant cross-section at small strain levels, the changes in cross-sectional area can be considered negligible. Under these conditions, the stress–strain curve for an idealized, perfectly plastic material initially appears as a straight line with a positive slope, corresponding to elastic deformation. This elastic regime typically dominates up to relatively large strains in elastic and viscoelastic materials. However, in the case of soft metals, elastic deformation occurs only at the very beginning of the loading process—typically up to strains around 0.2%,[8,9,21] a value barely discernible in practice and therefore neglected in our analysis.

Beyond this point, the curve transitions sharply to a horizontal line at the yield stress, indicating a regime of constant stress characteristic of plastic deformation. Above this level it sharply transitions to a horizontal line at the yield stress level, indicating constant stress during plastic deformation. However, in the case of compressing an object with a non-uniform cross-section (such as a sphere) or where the values of this cross-section vary significantly, the perfect plastic model (or any other model used here) cannot be directly applied to analytically find a solution. This is because, at a given time step (overall engineering strain, ε), different points within the compressed object experience different equivalent (local) stresses, σ_{eq} (Fig. 6a). Consequently, the results on the graph represent an effective force–strain response that accounts for the heterogeneous distribution of stresses and strains throughout the object. The simulation graph for the perfect plastic model (Fig. 6b, purple colour) is therefore a curve with

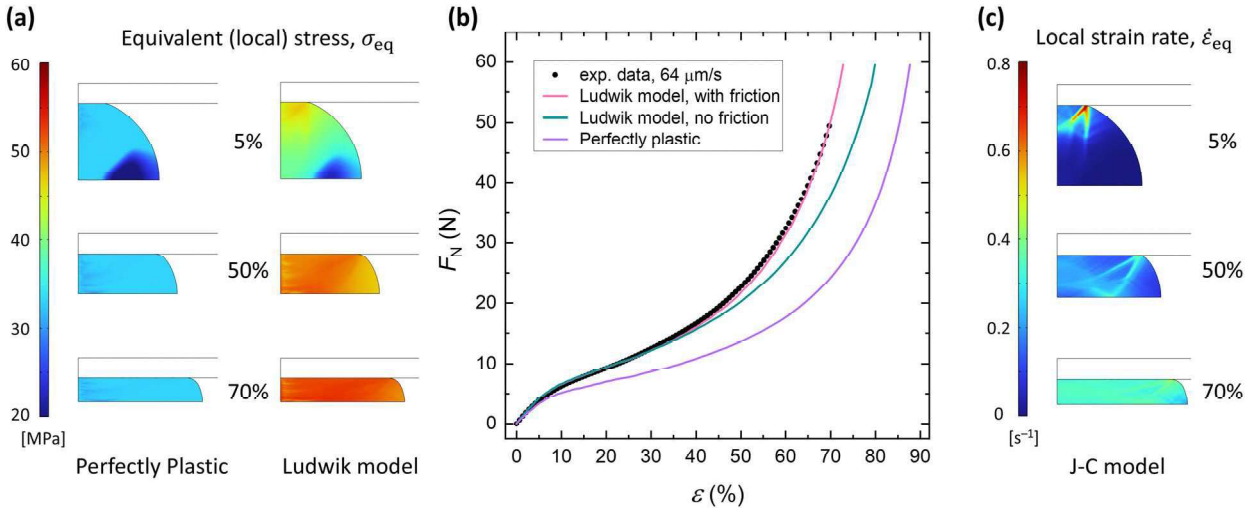

Fig. 6 (a) 2D axisymmetric COMSOL simulations depicting the equivalent (local) stress distributions within a quarter-sphere subjected to uniaxial compression. The left column illustrates results for a perfect plastic model, while the right column corresponds to a Ludwik material model, under 5%, 50%, and 70% strain. The perfect plastic model exhibits a uniform stress distribution capped at approximately 33 MPa, signifying no further stress increase post-yield. Conversely, the Ludwik model demonstrates stress heterogeneity, indicative of a more accurate representation of material behaviour under deformation. See also corresponding Movie S1 (ESI†). (b) The force-compression response is shown for three models: perfect plastic, Ludwik without friction, and Ludwik with friction. The model incorporating Ludwik material behaviour with friction exhibits the closest alignment with experimental data, obtained from compression testing of a 650-μm $Sn_{63}Pb_{37}$ solder ball at an engineering strain rate of approximately 0.1 s^{-1}. (c) 2D axisymmetric COMSOL illustrations of a quarter-sphere under compression, showing equivalent local strain rate distributions at 5%, 50%, and 70% strain. These strain rate distributions are used in the J–C model to calculate the resulting equivalent stress values, and eventually the global compressive force F_N. See also corresponding Movie S2 (ESI†).

varying force values. As expected, the simulation results are far from the actual data, which is understandable since solder is a viscoplastic material with hardening.

The results from simulations based on the Ludwik model indicate that hardening behaviour of the material, influences both the values of the equivalent stress and its distribution, as illustrated in Fig. 6a (second column). The simulated curve (Fig. 6b, teal colour) shows a close approximation to the actual laboratory data. With appropriate parameter selection, the simulation can accurately replicate experimental results, particularly in the low to mid-range deformation levels. For large deformation values, the friction of the sliding material on the plane of the compressing slabs can play a role. Thus, in the last simulation presented in Fig. 6b (pink colour), frictional force was added (friction coefficient $\mu = 0.15$), increasing the effective compressive force. As can be seen, this allows for a better fit of the numerical data to the experimental data.

However, to determine the appropriate (not arbitrarily chosen) model parameters, it is necessary to perform parameterization firstly for the reference data and then for a family of experimental curves. The material model used for parameterization is the J–C plasticity model.

Fig. 7 presents the results of parameterization using the J–C model. Panel (a) shows a set of experimental curves as a function of strain rates, along with the corresponding simulations. The fitting process began by fitting the force-deformation curve at a strain rate of 1.5 s^{-1}, where the most extensive data was available from five independent experiments conducted by two researchers. Based on this curve, key material parameters such as $\sigma_{y,\mathrm{ref}}$, k_{ref} and n_{ref} were determined, enabling further parameterization to find C by fitting the simulations to the full set of experimental curves. The parameters used in the calculations are provided in Table 1, panel (a). Once all parameters were identified, the complete set of curves was plotted. Additionally, knowing C enables calculation of strain rate-dependent yield stress values σ_y using the equation $\sigma_y = \sigma_{y,\mathrm{ref}} \times (1 + C{\cdot}\ln(\dot{\varepsilon}_{\mathrm{eng}}/\dot{\varepsilon}_{\mathrm{eng,ref}}))$ for the corresponding strain rates. For example, at an engineering strain rate of 4.0×10^{-1} s^{-1}, the calculation is: $\sigma_y = 34 \times (1 + 0.07{\cdot}\ln(0.267) = 30.8$ MPa. Yield stress values for different strain rates are provided in Table 2.

Subsequently, parameterization was performed to find the optimal values of C and m to best fit the additional experimental data series. Fig. 7b presents a set of experimental curves as a function of temperature, along with the corresponding simulations. Similar to the strain rate parameterization in Fig. 7a, an iterative approach was applied here. Initially, model parameters were adjusted to minimize the difference between simulated and experimental curves at 5 °C, establishing a baseline parameter set (see Table 1, panel b). This allowed further parameterization to determine m, which was set at 0.7. This value aligns with the scaling parameter obtained from data collapsing in Fig. 4b. With all parameters identified, the full set of curves was plotted. Additionally, knowing m allows calculation of temperature-dependent yield stress values σ_y using the equation: $\sigma_y = \sigma_{y,\mathrm{ref}} \times (1 - T^{*m})$ for the corresponding temperatures. For instance, at temperature 50 °C, the calculation is: $\sigma_y = 19 \times (1 - [(50 - 5)/(183 - 5)]^{0.7}) = 11.74$ MPa. Yield stress values for different temperatures are provided in Table 3.

Experimental and 3D simulation results of particle chain compression

In this section, we investigated the compression of assembled microballs. We conducted experiments where the balls were arranged linearly, as well as experiments where the balls were freely dispersed, meaning they did not touch each other during the compression. Fig. 8a shows the experimental results, illustrating the relation between normal force (F_N) and strain (ε) for different configurations of particle chains. The data were

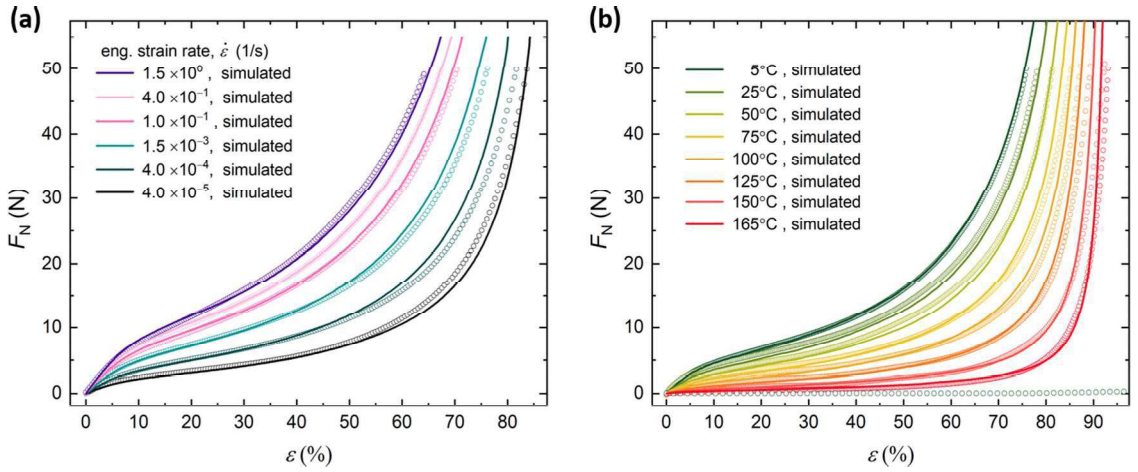

Fig. 7 Force–strain curves for (a) different engineering strain rates from 4×10^{-5} to 1.5 s^{-1}, and (b) different temperatures from 5 °C to 165 °C. Open circles represent experimental data, while solid lines show simulated results using the J–C model. In panel (a), the simulated curves agree well with the experimental data across the entire strain range, with only slight deviations at higher strains, which are within the typical variation range (as shown in Fig. 5). Notably, although the J–C model is typically applied to dynamic situations and does not account for material relaxation, it effectively describes the behaviour of solder microparticles across the tested strain rates and deformations. Panel (b) illustrates the temperature-dependent softening of the material, where higher temperatures lead to a decrease in compressive force for the same strain level, with simulations accurately reflecting this trend.

Table 1 Material parameters used for initial curve fitting and parameterization of $\dot{\varepsilon}$ and T dependencies. The parameters for $\sigma_{y,ref}$, k, n in panel (a) were obtained from fitting data from experiments conducted at a strain rate of 1.5 s^{-1} and at a temperature of 23 °C, while the parameters in panel (b) were obtained from data fitting for an experiment conducted at a strain rate of 4.0 × 10^{-4} s^{-1} and a temperature of 5 °C

	$\sigma_{y,ref}$ [MPa]	k_{ref} [MPa]	n_{ref} [—]	C [—]	m [—]	Mesh size [m]	Poisson ratio [—]	YM [GPa]
Panel (a)	34	39	0.2	0.07	0	5×10^{-4}	0.39	35
Panel (b)	19	21	0.2	0	0.7	1×10^{-5}	0.39	35

Table 2 Calculated σ_y values for various $\dot{\varepsilon}$, based on the C-parameter obtained from the J–C model parameterization

$\dot{\varepsilon}$ [s^{-1}]	1.5×10^{0}	4.0×10^{-1}	1.0×10^{-1}	6.0×10^{-3}	4.0×10^{-4}	4.0×10^{-5}
σ_y [MPa]	34	30.8	27.5	20.7	14.3	8.78

Table 3 Calculated σ_y values for various T, based on the m-parameter obtained from the J–C model parameterization

T [°C]	5	25	50	75	100	125	150	165
σ_y [MPa]	19	14.9	11.7	9.11	6.76	4.58	2.54	1.37

processed through averaging and polynomial fitting. The curves indicate that linearly arranged particle systems exhibit greater resistance to deformation, requiring more force to reach the same strain level compared to systems with freely dispersed particles. The difference in force values becomes noticeable for strains above approximately 20%. At this level of strain, the contact surface between the particles becomes substantial, and the shape of the particles during deformation begins to deviate from symmetry, transitioning from spherical to disc-like, and eventually to an elongated form (see Fig. 8b, c and Movie S3, ESI†).

Fig. 8b and c show the deformation stages of a pair of particles (panel b) and a segment of an infinitely long particle chain under compression (panel c). The images illustrate how the particles undergo shape changes at different strain levels: 10%, 30%, and 70%. At low strains, the particles remain nearly spherical, indicating minimal deformation and a small contact area between neighbouring microparticles (A_2), represented by the blue regions. As the strain increases, the particles begin to flatten, transitioning into a disc-like shape. At high strains, this deformation becomes even more pronounced, with the particles adopting an elongated, oblong form. This visual progression underscores the mechanical behaviour of particles within a chain configuration and demonstrates how their interactions contribute to the overall deformation process.

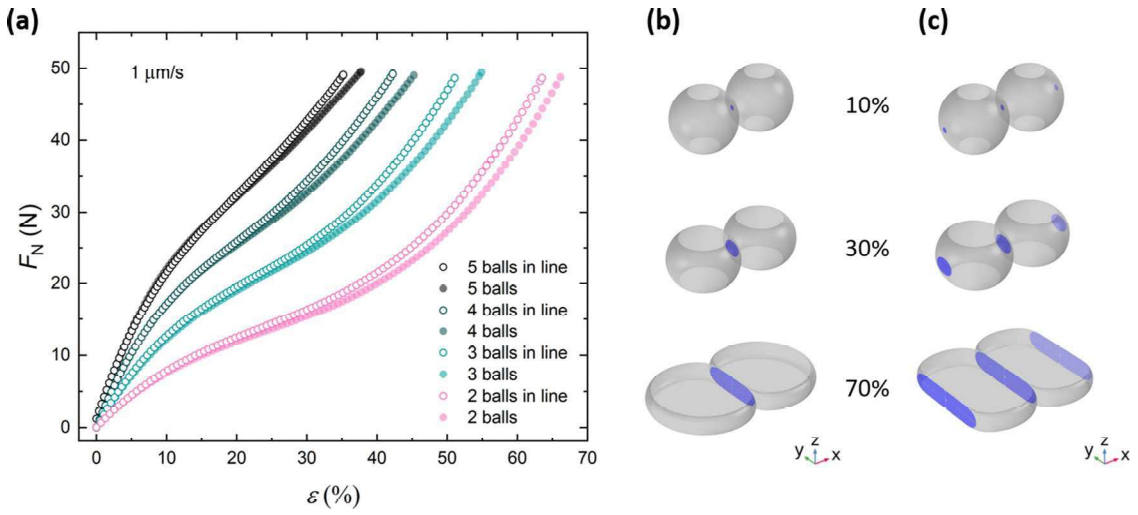

Fig. 8 (a) Experimental results depicting the relation between normal force (F_N) and strain (ε) for various particle configurations. Linearly arranged particle systems exhibit greater resistance to deformation, requiring higher forces to achieve equivalent strain levels compared to systems with freely dispersed particles. The experiments were conducted at an engineering strain rate of 0.0015 s^{-1}. The magnitudes of error bars (typically <5% relative error) are smaller than the symbol sizes and are not visible. (b) and (c) Shape deformation stages of particles under compression at different strain levels (10%, 30%, and 70%), showing the contrast between two-particle systems (b) and a segment of an infinitely long particle chain (c). The two-particle system exhibits asymmetrical deformation, while the infinite chain shows symmetrical deformation due to balanced forces from neighbouring particles. Blue colour indicates contact areas between neighbouring particles (A_2).

In the configuration with only two particles (Fig. 8b), there are no constraints on the side opposite to the contact, which leads to asymmetric deformation relative to the axis passing through the centre of the particle. In contrast, in the segment of an infinitely long chain (Fig. 8c), constraints are present on both sides, resulting in symmetrical deformation, with the microparticles elongating somewhat faster in the direction parallel to the chain axis due to the balanced forces exerted by neighbouring particles.

To simulate the response of different microparticle configurations under compressive force, it was necessary to perform 3D simulations. A 2D axisymmetric approach (used in Section 3.2) would be insufficient due to the inability to accurately capture the full geometrical and mechanical behaviour of the spherical particles, especially in cases involving asymmetric deformation, complex contact interactions, and variations in force distribution across the surface of the microparticle, which are inherently three-dimensional phenomena. Importantly, the best-matched parameters for the J–C model obtained from the 2D axisymmetric simulations were applied directly to the 3D simulations, providing a well-calibrated basis for this expanded analysis. The appropriate symmetries used for efficient simulations are provided in the COMSOL mph files, included as ESI.†

Fig. 9a presents the experimental results and the corresponding simulations (represented by dashed and solid lines) for various ball configurations (2, 3, and 4 balls, both in-line and separated). As observed, the simulated results closely match the experimental data, indicating the accuracy of the model. It is noteworthy that the difference in force values between the separated and in-line configurations increases as the number of balls is increased. In Fig. 9b, we present the percentage difference in simulated compression forces between the 'in line' ball configuration and the 'separated' configuration. As can be observed, this difference increases with the number of balls but stops rising significantly for a particle chain consisting of around 10 balls. The curve begins to approach the theoretically predicted value for an infinite chain of balls.

The observed difference in compression forces for systems with varying numbers of balls, as shown in Fig. 9b, is due to the deformation constraints that arise as the number of particles in the system increases. In the case of two balls, each can deform in multiple directions, as the compression forces are not restricted solely to the balls' contact direction. In a system of three balls, the central particle experiences constraints from both sides, which reduces its freedom to deform and leads to higher compression forces compared to the two-ball system. In the case of four balls, the two central particles are further constrained, increasing the difference between the forces in the in-line and separated configurations. For very long chains, the number of neighbouring particles drives the system closer to the behaviour predicted theoretically for an infinite chain, where additional balls no longer introduce significant changes in the force distribution.

Fig. 10a presents the simulated relationship between average plate-particle contact pressure (F_N/A_1) and compressive strain for three configurations: unconfined microparticles, two microparticles in contact, and a segment of two microparticles in an infinite chain. The values for all configurations are normalized per particle. Initially, the contact pressure is high due to the small contact area between the microparticle and plate; however, as the contact area increases with strain, the pressure decreases. This trend is followed by a subsequent rise beyond around 50% strain, driven by the effects of tangential friction and material hardening.

In Fig. 10b, the average interparticle contact pressure is plotted against compressive strain for two configurations: two microparticles in contact and a segment of two microparticles in an infinite chain. The pressure values for small strains (up to approximately 20%) exhibit oscillations, which are numerical artifacts caused by the mesh resolution used in the 3D simulation and are not of physical origin. A finer mesh could smooth

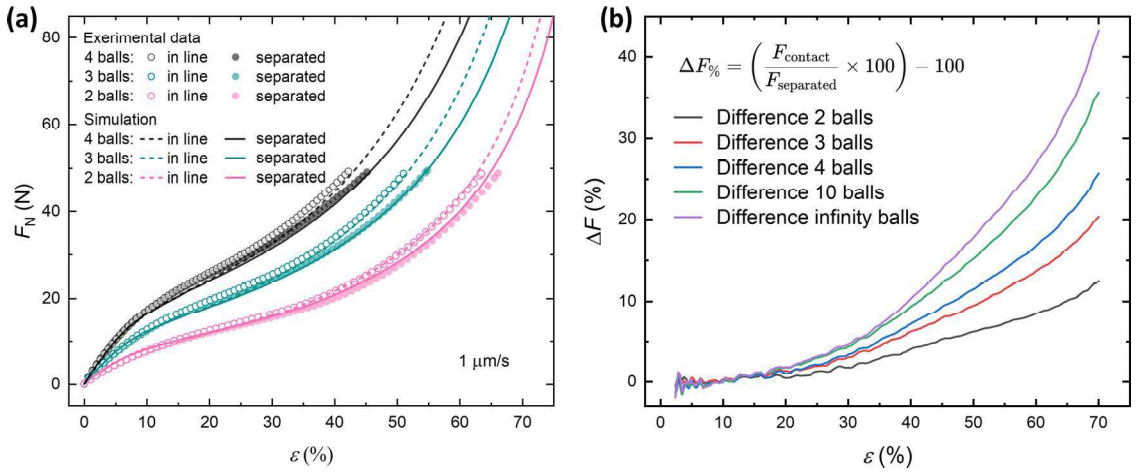

Fig. 9 (a) Experimental data (symbols) and simulation results (lines) for 2, 3, and 4 balls, arranged either in-line or separated, showing normal force (F_N) as a function of strain (ε). Both the experiments and simulations were conducted at an engineering strain rate of 0.0015 s^{-1}. The magnitudes of error bars (typically <5% relative error) are smaller than the symbol sizes and are not visible. (b) Percentage difference in simulated normal force (ΔF) for different numbers of balls in the in-line configuration, where the force is normalized by dividing the total applied force by the number of particles.

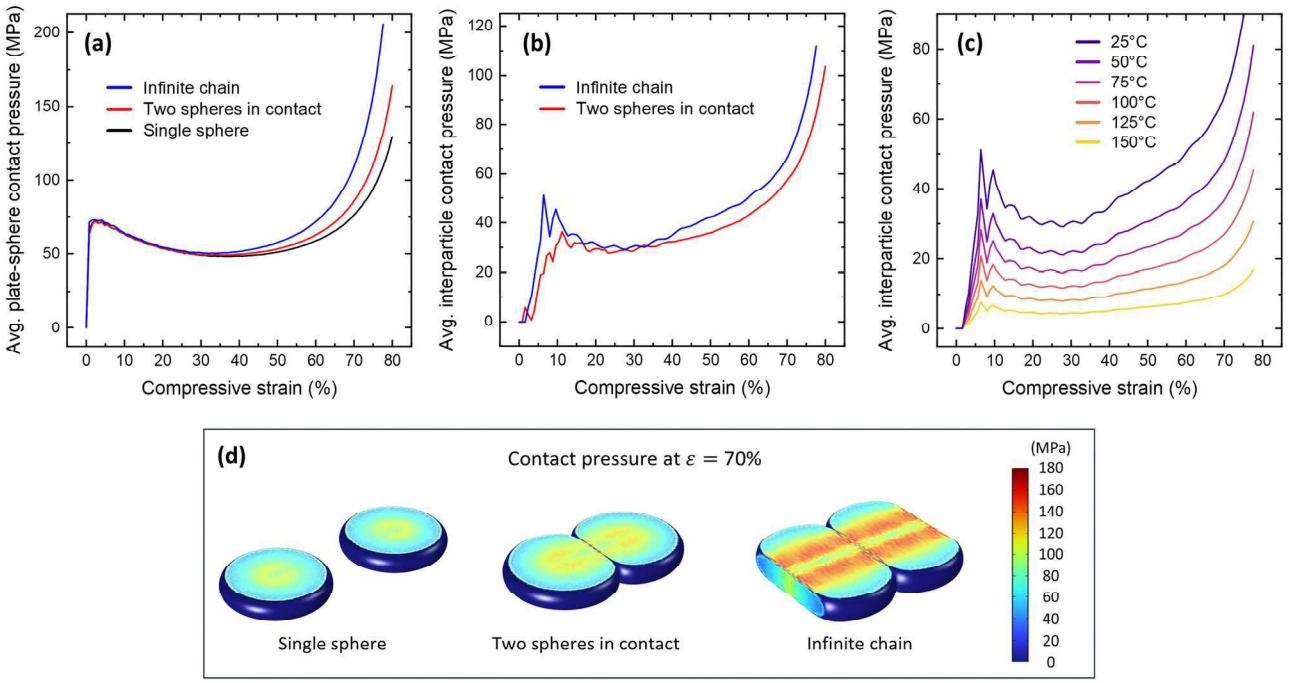

Fig. 10 (a) Average plate-sphere contact pressure as a function of compressive strain for three configurations: single sphere, two spheres in contact, and an infinite chain. (b) Average interparticle contact pressure *versus* compressive strain for two configurations: two spheres in contact and an infinite chain. (c) Temperature effect on interparticle contact pressure as a function of compressive strain, evaluated at different temperatures. (d) Simulated contact pressure distribution maps at 70% compressive strain for three configurations: unconfined microparticles, two microparticles in contact, and a segment of two microparticles in an infinite chain, generated in COMSOL. Note that the results are normalized per particle. All simulations were conducted at an engineering strain rate of 0.0015 s^{-1}.

these results, though it would significantly increase simulation time. However, this is not critical, as the overall trend remains clear, and the data values are relatively accurate.

The curves exhibit a similar trend to those in panel (a), though the initial rise in pressure is more gradual and extends over a broader range of strains (to around 10%). The interparticle contact pressures are roughly 40% lower than the plate-particle contact pressures. As in panel (a), the chain configuration exhibits higher pressure values. This is attributed to the geometric constraints imposed within the compressed chain: each microparticle is restricted from lateral deformation by adjacent particles, resulting in a more concentrated load at the contact points. In contrast, in the two-microparticle configuration, each particle can deform laterally in directions other than the contact point, leading to lower overall contact pressures.

Fig. 10c illustrates the results of simulations examining the effect of temperature on interparticle contact pressure within an infinite chain under compression. The plots display contact pressures across a range of temperatures, from 25 °C to 150 °C. As temperature increases, a decrease in interparticle contact pressure is observed, aligning with expectations. This relationship highlights the temperature dependence of mechanical interactions between particles, which is critical for understanding potential mechanisms of mechanical solid-state bonding within particle chains and, consequently, for enhancing electrical contact.

In Fig. 10d, simulated contact pressure distribution maps at 70% compressive strain show detailed pressure distributions for the three particle configurations. These color-mapped images visually capture how pressure is concentrated at contact points within each configuration. In the chain configuration, a repetitive, regular pattern of high-pressure zones is observed along the compression axis. For the single sphere, the pressure is centrally concentrated, with deformation symmetrically spreading around the contact point with the plate. In the two-sphere configuration, there are two regions of high pressure—at the contact point between the spheres and at the points where they contact the plate. Notably, in the infinite chain configuration, local pressure values are nearly twice as high as the average pressure values, both for plate-particle and interparticle pressures. This may have implications for the mechanical stability of the chain, such as stronger adhesion to the substrate and enhanced bonding between particles.

Discussion and conclusions

One of the main motivations for conducting this study was to understand the differences in deformation between unconstrained individual particles of malleable materials, such as solder, and particles arranged side-by-side in a linear structure.

We began our research with experiments on the deformation of individual unconstrained solder microparticles, studying the compressive force across a wide range of strains (0 to 80%), strain rates (0.000031 to 1.5 s^{-1}), particle diameters (200–650 μm), and temperatures (5–165 °C). To our knowledge, this is one of the most comprehensive experimental studies on the deformation of

solder ($Pb_{63}Sn_{37}$ and $Sn_{96.5}Ag_3Cu_{0.5}$). By employing a systematic data collapse approach on the experimental results, we derived an empirical relationship that correlates compressive force with particle size, strain rate, and temperature. To supplement the experimental findings, we conducted simulations, which not only validated the empirical data but also allowed us to extend the parameter space beyond hardware-imposed limitations of strain rate and maximum compressive force.

For the simulations, we used the J–C model, which accurately reflected the experimental data across the full range of strain rates, strains, and temperatures. In implementing this model, we also incorporated the friction coefficient to account for interfacial effects. Thus, for the material examined within the specified parameter ranges, we conclude that the J–C model is sufficiently robust, making the application of more complex models[22] unnecessary for this case.

The results of the study show that temperature exhibited a more pronounced effect on the applied force compared to strain rate. As temperature increased, material strength decreased significantly, attributed to the heightened mobility of dislocations within the material at elevated temperatures. In contrast, the influence of strain rate was relatively weak, suggesting that a wide range of compression rates can be utilized in industrial applications without substantially impacting the applied compressive force. These findings provide valuable insights for optimizing industrial processes involving solder microparticles, such as calendering or cold rolling. Recognizing the dominant effect of temperature on material strength is important for ensuring the reliability and performance of solder joints under varying thermal conditions. Additionally, the minimal influence of strain rate permits faster processing speeds without compromising the mechanical integrity of the solder. This balance between temperature and strain rate effects supports more efficient and effective manufacturing processes.

Moreover, through model optimization, precise values for material parameters were identified, as detailed in Tables 1–3. It should be noted that the parameter C varies depending on the initial strain rate used for curve fitting. When fitting begins with the highest strain rate, C is 0.07, whereas starting with the lowest strain rate results in C being 0.24. This discrepancy arises from the mathematical structure of the logarithmic function in the model rather than from any intrinsic material behavior, indicating the importance of the chosen fitting approach.

The yield stress values, presented in Table 2, are noteworthy. At low compression rates, these values are significantly lower than typical reference values for solder materials (*i.e.*, 25–35 MPa at room temperature[23]). At a very low strain rate, such as 10^{-3} s^{-1} or lower, stress relaxation and creep can significantly lower the yield stress of solder materials. Under these conditions, the material behaves more like a viscoplastic than an elastoplastic material, rendering the conventional definition of yield stress less applicable. This effect is evident in Fig. S4 (ESI†), where strain in the solder continues to increase over time under constant loads, even at low levels of applied force. Slow deformation through mechanisms such as atomic diffusion and dislocation motion contributes to creep, while stress relaxation results from the gradual dissipation of built-up stress as atoms in the solder's crystal structure rearrange. These mechanisms collectively contribute to a lower observed yield stress at very low strain rates, as the material undergoes continuous deformation without an increase in applied stress.[24] Table 3 demonstrates a significant decrease in yield stress with increasing temperature. This reduction is attributed to increased atomic mobility and a greater tendency for creep at higher temperatures, with the crystalline structure of the solder becoming increasingly susceptible to plastic deformation.

In the latter part of the study, we extended the investigation to more complex systems, specifically examining in-line configurations. A comparison between isolated particles and particles in contact was performed both experimentally and through simulation. As the number of particles in the chain increased, the difference in compressive force compared to isolated particles grew significantly, following an asymptotic trend. This trend approaches a limit as the number of particles increases, aligning with theoretical predictions for an infinite chain, where additional particles no longer significantly alter the force distribution. This effect arises from deformation constraints that intensify with an increasing number of neighbouring particles in contact.

Additionally, the simulations provided an in-depth view of pressure distributions, which would be exceedingly difficult, if not impossible, to capture experimentally. This allowed us to examine the impact of particle arrangement and temperature on contact pressures within compressed solder microparticle systems. Configurations involving multiple particles, such as chains, exhibited higher plate-sphere contact pressures compared to isolated particles, primarily due to lateral deformation constraints imposed by neighboring particles. We also quantified the sphere-sphere contact pressures across different particle configurations.

These findings highlight the relative magnitudes of contact pressures at various temperatures, which is essential for understanding the formation of conductive pathways in electronic applications. The bead-like particle chain structure, as referenced in the introduction, offers advantages for creating conductive paths and other electronic applications.[25] Elevated temperatures promote effective solid-state bonding between microparticles by facilitating processes such as diffusion and interface softening. However, the reduction in interparticle contact pressure at higher temperatures may lessen the mechanical stability of the bonding, potentially affecting the overall durability and conductivity of the assembled structure. These results suggest directions for further exploration, which will be addressed in detail in our subsequent work.

While the study centres on solder microparticles, the same principles regarding particle confinement, lateral constraints, and progressive plastic or viscoplastic deformation are relevant to various soft matter systems. For instance, gels or elastomers containing rigid filler particles can be modelled similarly, with local contact regions behaving analogously to solder-ball

junctions. These insights help guide the design and optimization of stretchable electronics, shape-morphing composites, or soft robotic actuators, where the interplay between rigid inclusions and soft matrices is pivotal.

Author contributions

Y. Harkavyi initiated the project, formulated scientific hypotheses, co-designed all experiments, and performed the experiments with results presented in Fig. 1–10. Z. Rozynek co-designed and performed experiments with results shown in Fig. 2–4 and 7–9. K. Giżyński co-designed and performed the experiments with results presented in Fig. 4–10. Y. Harkavyi wrote the first version of the manuscript. All authors took part in discussions toward the finalization of the manuscript. Y. Harkavyi administered the submission and the review process.

Declaration of generative AI and AI-assisted technologies in the writing process

During the preparation of this work, we utilized an AI-powered writing assistant, Grammarly, solely to enhance readability and language clarity. Following the use of this tool, we meticulously reviewed and edited the content. Therefore, we take full responsibility for the content of the publication.

Data availability

The data supporting this article have been included as part of the ESI.†

Conflicts of interest

The authors declare that they have no known competing financial interests or personal relationships that could have appeared to influence the work reported in this paper.

Acknowledgements

This research was funded by the Polish National Science Centre through OPUS (grant no. 2019/33/B/ST5/00935 and 2022/45/B/ST5/03529) and SONATA (grant no. 2019/35/D/ST5/03613) programs. We wish to thank CADENAS P.S.A. in Poland for giving us access to the company's research infrastructure and for providing materials. We also extend our gratitude to Marek Woźniak for preparing the 3D rendering visualizing the experimental setup (Fig. 1a).

References

1 Z. Rozynek, Y. Harkavyi and K. Giżyński, Fabrication of 1D particle structures outside a liquid environment using electric and capillary interactions: from fundamentals to applications, *Mater. Des.*, 2022, **223**, 1–11.
2 S. Zhang, Y. Liu, Y. Qian, W. Li, J. Juvert, P. Tian, J.-C. Navarro, A. W. Clark, E. Gu, M. D. Dawson, J. M. Cooper and S. L. Neale, Manufacturing with light – micro-assembly of opto-electronic microstructures, *Opt. Express*, 2017, **25**(23), 28838–28850.
3 F. Klocke and C. Wagner, Coalescence behaviour of two metallic particles as base mechanism of selective laser sintering, *CIRP Ann.*, 2003, **52**(1), 177–180.
4 N. Suetsugu and E. Iwase, Conduction Conditions for Self-Healing of Metal Interconnect Using Copper Microparticles Dispersed with Silicone Oil, *Micromachines*, 2023, **14**(2), 1–9.
5 X. He, S. B. Wang, Y. X. Wang, L. Liu, Y. W. Dong and Y. Yao, Viscoplastic behavior of bulk solder material under cyclic loading and compression of spherical joint-scale granules, *J. Mater. Sci.: Mater. Electron.*, 2021, **32**(15), 20640–20650.
6 H. C. Lin, C. Kung and R. S. Chen, Evaluations of the BGA solder ball shape by using energy method, *CMC-Comput. Mat. Contin.*, 2007, **6**(1), 43–50.
7 M. A. Haq, M. A. Hoque, J. C. Suhling and P. Lall, Determination of Anand Parameters From Creep Testing of SAC305 Solder Joints, ASME 2020 International Technical Conference and Exhibition on Packaging and Integration of Electronic and Photonic Microsystems, 2020.
8 M. A. Haq, M. A. Hoque, J. C. Suhling and P. Lall, Anand Parameters for Eutectic Tin-Bismuth Solder, 20th InterSociety Conference on Thermal and Thermomechanical Phenomena in Electronic Systems (ITherm), *IEEE Electr. Network*, 2021, pp. 926–932.
9 M. Motalab, Z. J. Cai, J. C. Suhling and P. Lall, Ieee, Determination of Anand constants for SAC Solders using Stress–Strain or Creep Data, *13th IEEE InterSociety Conference on Thermal and Thermomechanical Phenomena in Electronic Systems (ITherm)*, IEEE, San Diego, CA, 2012, pp. 910–922.
10 L. Zhang, J. G. Han, Y. Guo and C. W. He, Anand model and FEM analysis of SnAgCuZn lead-free solder joints in wafer level chip scale packaging devices, *Microelectron. Reliab.*, 2014, **54**(1), 281–286.
11 J. F. Liu, V. P. W. Shim, V. B. C. Tan and T. K. Lee, Dynamic Testing of Solder Joint Strength under Compression, Tension and Shearing, 2007 9th Electronics Packaging Technology Conference, 2007, pp. 380–385.
12 T. T. Nguyen, D. Yu and S. B. Park, Characterizing the Mechanical Properties of Actual SAC105, SAC305, and SAC405 Solder Joints by Digital Image Correlation, *J. Electron. Mater.*, 2011, **40**(6), 1409–1415.
13 Y. L. Lin, D. M. Wang, W. M. Lu, Y. S. Lin and K. L. Tung, Compression and deformation of soft spherical particles, *Chem. Eng. Sci.*, 2008, **63**(1), 195–203.
14 H. Y. Bu, Q. Li, S. H. Li and M. N. Li, Comparison of Modified Johnson–Cook Model and Strain-Compensated Arrhenius Constitutive Model for 5CrNiMoV Steel during Compression around Austenitic Temperature, *Metals*, 2022, **12**(8), 17.
15 M. Bazilchuk, T. Sumigawa, T. Kitamura, Z. L. Zhang, H. Kristiansen and J. Y. He, Contact area measurement of

micron-sized metal-coated polymer particles under compression, *Int. J. Mech. Sci.*, 2020, **165**, 7.
16 F. Dutka, Z. Rozynek and M. Napiórkowski, Continuous and discontinuous transitions between two types of capillary bridges on a beaded chain pulled out from a liquid, *Soft Matter*, 2017, **13**(27), 4698–4708.
17 N. S. Selyutina and Y. V. Petrov, Comparative Analysis of Dynamic Plasticity Models, *Rev. Adv. Mater. Sci.*, 2018, **57**(2), 199–211.
18 R. Darveaux, M. Johnson and C. Reichman, Solder Joint Ductility, *Int. Microelectron.*, 2012, **2012**(1), 1046–1056.
19 S. T. Jenq, Y. S. Chiu, R. J. Lin and Y. S. Lai, The stress–strain relationship of $Sn_{63}Pb_{37}$ and SAC305 solder materials at elevated temperature condition, 2010 5th International Microsystems Packaging Assembly and Circuits Technology Conference, 2010, pp. 1–4.
20 J. Xu, X. Zhu, D. Shan, B. Guo and T. G. Langdon, Effect of grain size and specimen dimensions on micro-forming of high purity aluminum, *Mater. Sci. Eng., A*, 2015, **646**, 207–217.
21 W. J. Plumbridge and C. R. Gagg, Effects of strain rate and temperature on the stress–strain response of solder alloys, *J. Mater. Sci.: Mater. Electron.*, 1999, **10**(5), 461–468.
22 Y. Wang, X. Zeng, H. Chen, X. Yang, F. Wang and L. Zeng, Modified Johnson–Cook constitutive model of metallic materials under a wide range of temperatures and strain rates, *Results Phys.*, 2021, **27**, 104498.
23 H. Ma and J. C. Suhling, A review of mechanical properties of lead-free solders for electronic packaging, *J. Mater. Sci.*, 2009, **44**(5), 1141–1158.
24 N. Zhang, F. Yang, Y. Shi and F. Guo, Compression creep of 63Sn37Pb solder balls, *Acta Mater.*, 2011, **59**(8), 3156–3163.
25 Z. Rozynek, Y. Harkavyi, Ø. G. Martinsen and K. Giżyński, Fabrication of a new type of electrically conductive microtracks via mechanical compression of beaded structures, *Mater. Des.*, 2025, DOI: **10.1016/j.matdes.2025.113985**.

Supporting Information

Experimental and FEM simulation study of compressive deformation of solder microballs and particle chains

Y. Harkavyi[1], K. Giżyński[2] and Z. Rozynek,[1,3*]

[1] *Faculty of Physics, Adam Mickiewicz University, Uniwersytetu Poznańskiego 2, 61-614 Poznań, Poland*
[2] *Institute of Physical Chemistry, Polish Academy of Sciences, Kasprzaka 44/52, 01-224 Warsaw, Poland*
[3] *CADENAS P.S.A., Prof. Sylwestra Kaliskiego 24, 85-796 Bydgoszcz, Poland*

[*]Corresponding author: zbiroz@amu.edu.pl

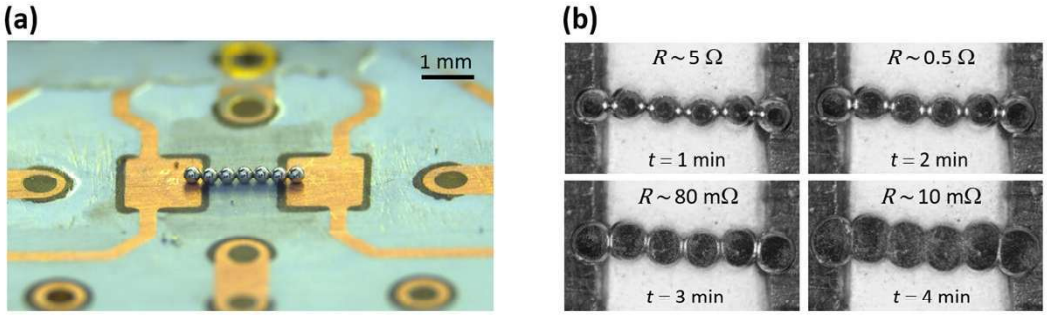

Figure S1. (**a**) Image showing a particle chain of 300-µm $Sn_{63}Pb_{37}$ spheres on a PCB carrier, stretched between two copper pads. (b) Top-view images of the compressed chain at four different stages, corresponding to 3%, 6%, 22%, and 50% compressive strain, during which the resistance of the structure changes from 5 Ω to 10 mΩ.

Resistance measurements were conducted with a Zurich Instruments MFIA (5 MHz Impedance Analyzer) using an MFITF fixture and a specially designed, low-loss PCB carrier, minimizing parasitic effects by eliminating lead wires for precise particle chain measurements. Nearly monodisperse 300-µm particles were deposited between 1.5 × 1.5 mm copper pads, 1.4 mm apart on the PCB. Low-frequency (100 Hz, 0.3 V) measurements of the impedance's real part (R) were used to minimize dielectric loss effects.

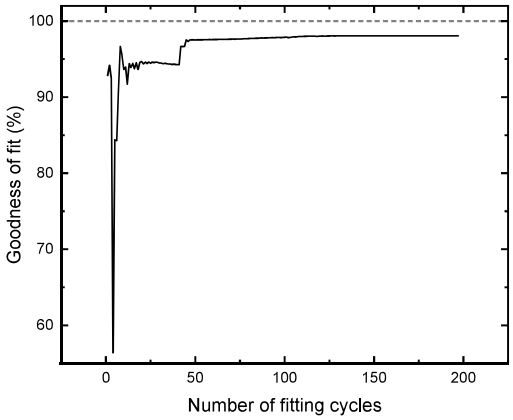

Figure S2. Goodness of fit as a function of fitting cycles during parameter optimization for the Johnson-Cook model. The goodness of fit increases sharply in the initial cycles and then gradually approaches an asymptote near 100%, where further improvements become marginal. The dashed line at 100% represents an ideal fit. This trend highlights the progressive fine-tuning of model parameters to closely align with experimental data, achieving an optimal fit within approximately 100 cycles, after which the changes stabilize.

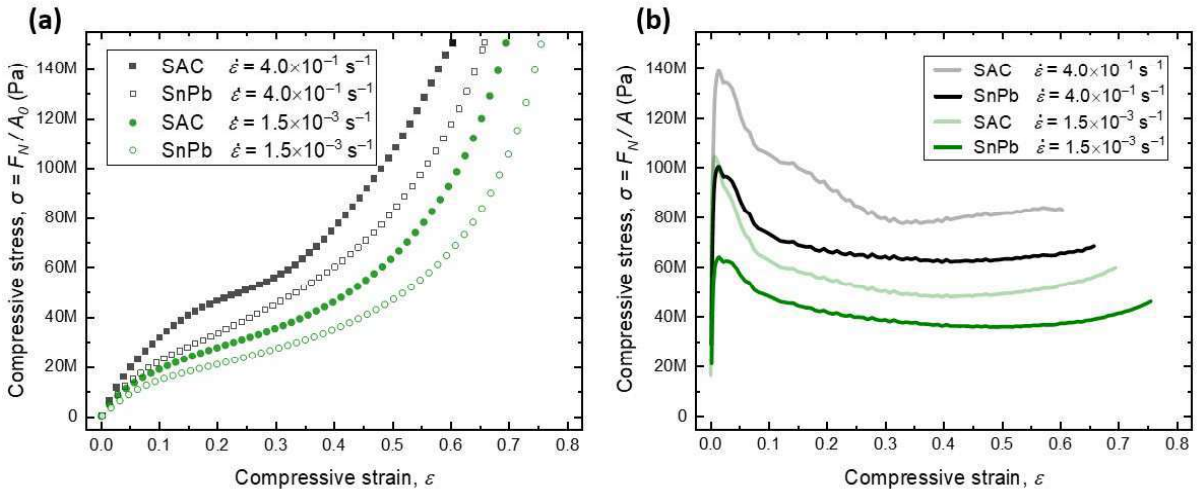

Figure S3. Compressive stress-strain curves for leaded and unleaded solder balls (**a**) Stress is calculated as applied force divided by the initial (equatorial) cross-sectional area of the uncompressed sphere. (**b**) Stress is presented as force divided by the actual contact area between the compressive slab and the sphere, which corresponds to a classical pressure-based approach.

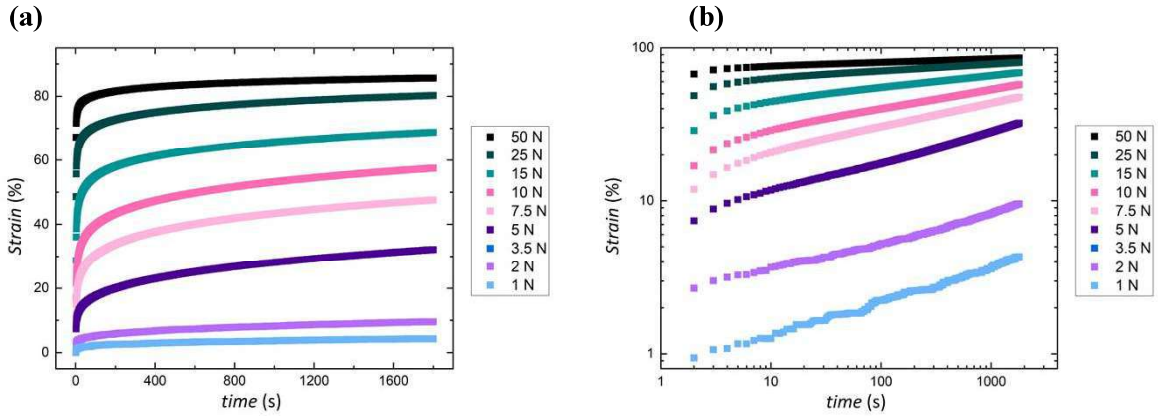

Figure S4. Engineering strain of a $Sn_{63}Pb_{37}$ solder ball with a diameter of 600 µm as a function of time, presented on (**a**) a linear-linear scale and (**b**) a log-log scale, under different compression forces (F_N) at a temperature of 23°C. The initial strain increases rapidly and then stabilizes over time, indicating a gradual approach to equilibrium. This behavior is typical for viscoelastic materials, where the material initially resists deformation and then enters a flow state.

Movie S1. 2D simulation results illustrating equivalent (local) stress distributions within a quarter-sphere subjected to uniaxial compression. The left panel shows results for a perfectly plastic material model, while the right panel presents results for a Ludwik material model.

Movie S2. 2D simulation results displaying the distribution of equivalent (local) stress (left panel) and local strain rate (right panel) within a symmetrical section of a sphere under uniaxial compression. The simulation employs the J-C model with an applied engineering strain rate of 0.1 s^{-1}.

Movie S3. 3D simulation results illustrating the stages of shape deformation for $Sn_{63}Pb_{37}$ particles under compression in two different configurations: two particles in contact (left panel) and a segment of an infinitely long particle chain (right panel). Contact areas between neighboring particles are highlighted in blue (A_2).

——Scientific Paper IV——

Fabrication of a new type of electrically conductive micro-tracks via mechanical compression of beaded structures

Rozynek Z., Harkavyi Y., Martinsen Ø.G., Giżyński K.

Materials & Design, Volume 253, May 2025, 113985

Materials & Design 253 (2025) 113985

Contents lists available at ScienceDirect

Materials & Design

journal homepage: www.elsevier.com/locate/matdes

Fabrication of a new type of electrically conductive micro-tracks *via* mechanical compression of beaded structures

Z. Rozynek [a,b,1,*], Y. Harkavyi [b,1], Ø.G. Martinsen [c,d], K. Giżyński [e]

[a] CADENAS P.S.A., Prof. Sylwestra Kaliskiego 24, 85-796 Bydgoszcz, Poland
[b] Faculty of Physics and Astronomy, Adam Mickiewicz University, Uniwersytetu Poznańskiego 2, 61-614 Poznań, Poland
[c] Department of Physics, University of Oslo, Sem Sælands vei 24, 0371 Oslo, Norway
[d] Department of Clinical and Biomedical Engineering, Oslo University Hospital, Sognsvannsveien 20, 0372 Oslo, Norway
[e] Institute of Physical Chemistry, Polish Academy of Sciences, Kasprzaka 44/52, 01-224 Warsaw, Poland

ARTICLE INFO

Keywords:
Conductive paths
Micro-tracks
Compressive deformation
Compressive strain
Solder balls
Linear structure
Zigzag arrangement
Polydispersity
Electrical resistance
Mechanical force
Computer simulations

ABSTRACT

In recent years, the importance of critical raw materials for global economic development has become increasingly evident, especially in electronics. A challenge in this industry is replacing traditional, unsustainable silver nanoparticle-based conductive pastes used for creating conductive paths. This paper presents an approach to fabricating conductive micro-tracks from preassembled bead-like chains of microparticles. These single-particle-thick structures achieve high conductivity through a straightforward post-processing method — mechanical compression — offering a sustainable alternative to complex nanoparticle pastes. Our study explores the effects of uniaxial compression on malleable microparticles deposited additively on substrates, examining particle deformation, interparticle contact area changes, and their impact on conductivity. Through comprehensive numerical simulations, closely aligned with experimental observations, we establish a quantitative relationship between compressive strain (ε), compressive force (F_N), the contact area between the compressing plate and the ball (A_1), interparticle contact area (A_2), and the electrical resistance (R) of the particle chain. We studied linear structures of monodisperse microparticles and investigated the effects of polydispersity and deviations from linearity. Furthermore, we studied the influence of compression force and process temperature on the stability of the substrate on which beaded structures are formed. This research presents a sustainable alternative to traditional nanoparticle pastes, offering a bottom-up method for developing optimized conductive paths.

1. Introduction

Electrically conductive tracks with thicknesses ranging from 20 to 500 μm are essential components in a wide range of devices. They serve as interconnects in PCBs, pathways in flexible electronics [1,2], sensors in biomedical devices [3], capacitive touch screens [4], antennas in RFID tags [5], interdigitated electrodes for piezoelectric devices [6], active layers in OLEDs [7], and fingers and busbars in photovoltaic cells [8], among many others. Currently, silver nanoparticle-based conductive pastes are the industry standard for fabricating these tracks due to their high conductivity and processing reliability. However, the growing demand for such pastes, driven by rapid expansion in sectors such as photovoltaics, flexible electronics, and the automotive sector, has raised significant concerns over sustainability and cost [9].

Last year's silver consumption exceeded global supply [10], and projections indicate that production may not meet future needs [11]. Increasingly, reports highlight risks to the supply chain stability of silver nanoparticle pastes [12,13], with potential shortages threatening the scalability of silver-dependent technologies, including photovoltaics [14,15]. Without alternative solutions, these challenges could hinder innovation and disrupt critical industries.

To address these risks, there is an urgent need to explore sustainable alternatives to silver nanoparticle-based conductive pastes. Developing additive technologies for producing conductive tracks from sustainable materials offers a promising solution to mitigate environmental, economic, and supply chain challenges while ensuring the growth and resilience of the global electronics industry.

Particle microtracks: A promising approach to fabricating highly

* Corresponding author at: Faculty of Physics and Astronomy, Adam Mickiewicz University, Uniwersytetu Poznańskiego 2, 61-614 Poznań, Poland.
E-mail address: zbiroz@amu.edu.pl (Z. Rozynek).
[1] These authors contributed equally to this work.

https://doi.org/10.1016/j.matdes.2025.113985
Received 18 December 2024; Received in revised form 15 April 2025; Accepted 21 April 2025
Available online 23 April 2025

conductive particle microtracks involves aligning microparticles side by side to form a 'beaded' structure. This approach offers several significant advantages over the microtracks made from the currently prevalent silver nanoparticle pastes. Specifically, microparticle-based tracks exhibit enhanced electrical conductivity. Unlike the porous network of sintered nanoparticles, beaded structures consist of aligned particles with direct contact between neighboring particles. This configuration ensures higher conductivity, as will be demonstrated in this work. In addition to enhanced conductivity, microparticles offer notable cost advantages, as they are generally more affordable than nanoparticles. Furthermore, microparticles enable the fabrication of tracks with an advantageous height-to-width ratio. This combination of properties unlocks immense potential for developing functional microtracks on substrates suitable for optical [16–18], biosensing [19], and electronic applications [20–22].

In the context of electronic applications, we have been exploring novel uses for single particle–resolution structures deposited on substrates, leveraging the aforementioned unique properties of the particle chains. In our recent publications [23–25], we demonstrated an uncomplicated electric method for efficiently assembling particles into 1D structures outside a liquid environment. The developed method is versatile, accommodating various types of electrically conductive particles (*e.g.*, solid and core–shell balls or hollow spheres) with radii ranging from 10 to 500 μm, enabling their organization into single-particle–thick structures. These particles can be organized into single-particle-thick structures and subsequently deposited onto substrates to form both linear and nonlinear patterns.

In **Fig. S1**, we present a few examples of different particle patterns created on substrates using the electric method described in ref. [25]. **Fig. S1a** depicts parallel lines of aluminum particles formed on a photovoltaic solar cell, **Fig. S1b** displays a path of solder balls deposited on a surface of the printed circuit board (PCB), and **Fig. S1c** demonstrates nonlinear microtracks of unleaded solder particles printed on a plexiglass substrate. These particle microcracks have the potential to be used as solar cell fingers and busbars, transmission lines on PCBs, and conductive pathways in composite materials, among other applications.

The prerequisite for using chain-like particle structures in many electronic applications is that the microtracks made of them are electrically highly conductive. However, the as-deposited particle structures (as those shown in **Fig. S1**) exhibit low conductivity, typically several orders of magnitude smaller than commonly used conductive micropaths. This is due to the small contact area between the neighboring particles, which limits the flow of electrical current. Fortunately, various post-processing solutions exist that can increase the conductivity (and often also mechanical stability) of the particle microtracks.

Electrical conductivity of a single particle–thick structure: A particle chain exhibits higher resistance compared to a solid wire with the same linear mass density [21]. However, once the chain particles are firmly joined (through fusing, sintering, or other methods), the structure's resistance decreases and eventually matches that of the wire conductor made of the same material. This characteristic makes a post-treated single particle–thick structure an excellent choice for conductive microtracks. Compared to widely used conductive microtracks made of nanoparticles, microtracks made of microparticles demonstrate nearly one order of magnitude lower resistivity. As mentioned before, typically, nanoparticle-based microtracks are porous, and conductive paths are formed by a network of interconnected nanoparticles. This, along with other issues, such as the presence of insulating barriers like oxide layers and organic ligands at the nanoparticle interfaces, results in an overall increase in resistance of the microtrack based on nanoparticles [26–28]. In contrast, single particle-thick structures do not exhibit these issues. In addition, as already noted, microparticles are often less expensive to produce than nanoparticles. These two advantages (lower resistivity and lower fabrication cost) increase the attractiveness of commercial utilization of single particle–thick structures.

Postprocessing for enhancing electrical conductivity: Achieving high electrical conductivity in microtracks is essential for many applications. For the particle chains, this can be realized through specific post-processing techniques. Among the available methods, thermal treatments have been extensively employed. These encompass techniques such as Joule heating [29], microwave sintering [30], and infrared laser treatment [31,32], wherein microparticles are either sintered together through the growth of bonds (necks) between them or fused through particle melting and partial coalescence. In addition to thermal approaches, mechanical methods present an effective alternative, especially when working with malleable materials. Specifically, materials like tin, zinc, lead, copper, aluminum, silver, and gold [33] can undergo significant plastic deformation under compressive stress before failure. The particles are plastically deformed by applying compressive stress from above to the microparticle pattern (in a direction normal to the substrate). This process enlarges their contact areas, leading to an enhancement in electrical conductivity [34].

Each postprocessing approach for improving electrical conductivity has advantages and limitations, and their practicality depends on the specific application. For instance, Joule heating does not require a sophisticated experimental setup, but controlling heat generation and dissipation along the particle chain can be challenging. On the other hand, mechanical compression offers precise particle joining, allowing for accurate control of the contact area between adjacent particles and, consequently, the electrical conductivity. Straightforward calendering can be used to compress particle patterns deposited on flat surfaces, such as in the case of solar cells.

Compressive deformation: Extensive research, both experimental and theoretical, has been conducted on the deformation of various types of particles, addressing both static and transient deformation [35–42]. This study focuses specifically on the compressive mechanical deformation of malleable spherical particles between two parallel slabs. While numerous scientific contributions exist on the deformation of individual malleable conductive particles [43–45], studies addressing the deformation of particle chains compressed perpendicular to the chain's direction are scarce. We aim to fill this gap in knowledge through numerical simulations and experimental investigations.

Mechanical-electrical interplay: The deformation of particles within a chain induces changes in the contact between adjacent microparticles, affecting both the electrical properties (a key focus of this work) and phenomena such as particle fusion within the chain and the particles' adhesion to the substrate. While the literature includes studies on electrical transport within chains of metallic beads under stress, these studies predominantly concern compression along the chain's direction [46–49]. There remains limited knowledge about the correlation between the degree of compression (compressive strain, ε) and the electronic properties of the particle chain when compression occurs perpendicular to the chain's direction. Our results contribute to reducing this gap in understanding by providing new insights from experiments and simulations.

Analytical estimation of the shape evolution of side-by-side aligned particles undergoing compressive stress is non-trivial. Therefore, we rely on computer simulations for our analysis. Specifically, we utilize the finite element method to solve the continuum mechanics equations numerically. These simulations allow us to estimate several essential parameters: (i) particle shape, (ii) contact area and pressure between a particle and a pressing plate, and (iii) contact area and pressure between neighboring particles. These parameters can be evaluated over a wide range of compressive strains. Subsequently, we compare our theoretical results with experimental data, providing a solid foundation for thoroughly investigating the electronic properties of single particle–thick structures under compressive stress. The ultimate goal is to advance the understanding of the post-processing of particle chains to enable the efficient production of both single- and multi-layer structures containing conductive elements.

2. Methods

2.1. Materials

Silicone oil (Rhodorsil Oils 47), with a dynamic viscosity of 300 mPa·s at 25 °C, a density of 0.96–0.97 g·cm^{-3} at 25 °C, an electrical conductivity of 5–10 pS·m^{-1}, and a relative permittivity of 2.8, was used to prepare dispersions with unleaded solder particles (used in Fig. S1). Liquid flux (TK83, ThermoPasty, Poland), with a density of 0.85 g·cm^{-3} at 25 °C, was used to prepare dispersions with leaded solder microparticles (used in Fig. S1 and Fig. 8). Leaded solder microparticles ($Sn_{63}Pb_{37}$, various sizes ranging from 200 to 760 μm, electrical resistivity ~ 1.4 × 10^{-7} Ω·m) and unleaded solder microparticles (SAC305, sizes 500 and 760 μm) were purchased from PMTC, Taiwan. Silver microparticles (500 μm, electrical conductivity 1.59 × 10^{-8} Ω·m) were purchased from GoodFellow (AG00-SP-000140). The silicon wafer coated with silicon nitride (shown in Fig. S1a) was provided by colleagues from the Solar Department, IFE, Norway.

2.2. Fabrication of 1D structures on a substrate

The experimental setup used for the fabrication of 1D microstructures included a signal generator (SDG1025, Siglent), a high-voltage bipolar amplifier (10HVA24-BP1, HVP), a digital microscope (AM7115, Dino-Lite), a light source (KL 300 LED, Schott), motorized stages (MT1-Z8, Thorlabs) for vertical and horizontal substrate translation, and a PC for process control and image collection. We followed the methodology described in ref. [25] to print a particle structure on a substrate. In short, a particle dispersion was prepared and supplied to an electrically conductive microcapillary, which served as both a conduit and an electrode. A convex meniscus of the dispersion formed at the outlet end of the microcapillary, positioned above the surface of a substrate. An alternating voltage (1 kHz, square wave) was applied to the microcapillary, resulting in the formation of a 1D structure. The structure composed of aligned one-by-one particles was formed between the dispersion meniscus and the surface of the substrate. The substrate was then moved relative to the microcapillary, causing the deposition of the particle structure onto the substrate. The electric voltage was turned off to complete the printing. The substrate's motion determined the final shape of the particle pattern. See also the corresponding **Movie S1**.

2.3. Experimental setup for resistance measurement of chains under mechanical compression

The impedance measurements were conducted using an impedance analyzer (Zurich Instruments, MFIA, 5 MHz Impedance Analyzer) equipped with an impedance test fixture (MFITF) and a low-capacitive, low-loss two-terminal PCB carrier specifically designed for measuring surface-mounted electronic components. This PCB carrier was chosen to minimize parasitic effects and damping by eliminating the need for lead wires, allowing for the study of the electronic properties of particle chains. The equipment was calibrated using an open-circuit test (measurement of a device with infinite impedance) and a short-circuit test (measurement of a device with zero impedance). To enhance clarity and understanding of the experimental setup, we created 3D visualizations, as shown in Fig. 1 and the corresponding **Movie S2**. Photographs of the actual experimental setup have also been included in the supplementary materials for reference (**Fig. S2**).

A 5 mm thick glass slab was mounted on a translational stage and positioned above the sample. This setup facilitated the observation and recording of the chain's deformation during the compression process. The motion of the glass slab was controlled by a motorized translational stage (refer to Fig. 1**a**). A line composed of nearly monodispersed particles was deposited on the surface of the PCB carrier between two copper pads of size 1.5 × 1.5 mm with a separation distance of 1.4 mm (refer to Fig. 1**b**). To study the real part of the impedance (R), experiments were conducted using a low-frequency (100 Hz) voltage with an amplitude of 0.3 V. The low-amplitude AC signal was selected to minimize current-induced local welding [50,51], while the low frequency was chosen to avoid any potential influence from dielectric loss.

2.4. Theoretical model

To determine the change in the shape of the balls forming the chain and the contact areas between the plate and balls as well as between balls, 3D simulations were employed. The system configuration included three objects: a 760 μm spherical solder particle of $Sn_{63}Pb_{37}$ composition (Young's modulus E = 27.5 GPa, initial yield stress σ_{ys0} = 32 MPa, density ρ = 8400 kg·m^{-3}, electrical resistivity of 1.50 × 10^{-7} Ω·m), the pressing plate and another plate being a substitute for neighboring particle. Exploiting the system's symmetry at the contact plane allowed for model simplification. To reduce computational complexity, symmetry of the compressed objects was also utilized, resulting in modeling only 1/8th of the actual system. The pressing plate was lowered with a constant velocity while the position of the symmetry plate was fixed. Each rigid plate was meshed using a single brick element. The solder particle had tetrahedral elements with the maximum element size prescribed at the surface while the mesh inside it was set as the predefined 'normal' option. **Fig. S3 (a)** illustrates the final meshed geometry of the model, providing a visual representation of the simulated system

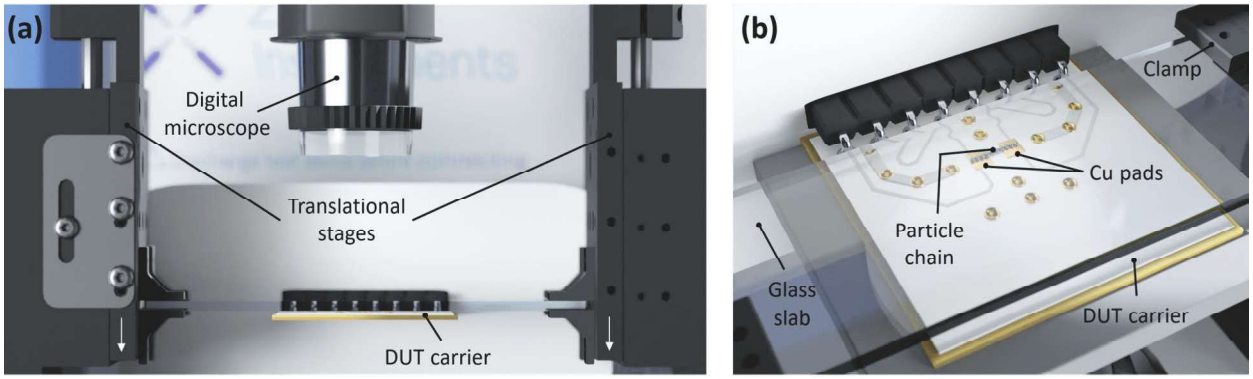

Fig. 1. 3D computer graphics of the experimental set-up used for resistance measurements of a particle chain under mechanical compression. The set-up includes the following components: **(a)** an impedance analyzer equipped with the impedance test fixture (MFITF), a digital microscope positioned above the particle chain to observe it from the top along the compression direction, translational stages for moving the compression slab (in a direction indicated by white arrows); and a device-under-test (DUT) carrier specifically designed for measuring surface-mounted electronic components. (**b**) The PCB carrier features a line of nearly monodispersed particles deposited on its surface between two copper pads. A thick glass, secured by clamps mounted on the translational stages, serves as the compression slab. Its position can be precisely controlled with sub-micrometer accuracy. Refer to **Movie S2** for additional visual information.

configuration.

In the realm of computational simulations, enhancing the mesh size is crucial for attaining accuracy, but leads to increased computational time. Despite efforts to simplify the geometry, 3D simulations remained time-consuming, often taking several weeks. The data shown in Supplementary Information demonstrate good agreement between the simplest plasticity model (perfectly plastic) and experimental data for contact areas between the press and the particle (A_1) and between neighboring particles (A_2) (refer to **Fig. S4**). The discrepancies with the experiment are likely due to the mesh size. We anticipate that further reduction in mesh size could yield experimental results, but such simulations would require significant time. For instance, with our computational resources, a single compression simulation of 760 μm spherical solder particle took 2 h with a maximum boundary element size set to 25 μm, 25 h with a maximum size of 6.3 μm, and 8 days with a maximum size of 5 μm. **Fig. S4** illustrates a comparison of each studied mesh element size.

In contrast to the aforementioned model, the resistance calculation of the deforming structure necessitates the use of the full geometry with two contacting spheres. In such a configuration, the number of mesh elements is doubled. Thus, to achieve computational efficiency, the mesh was coarsened compared to the confined single-ball model Fig. S3 **(b)**. In AC/DC Module model we utilized the Electric Currents interface to study the electrical resistance of the deformed structure as a function of the compression level. The current and ground sources were applied at the cross-sections of neighboring particles. Two modeling approaches were implemented: the *union* model and the *roughness* model. In the *union* model, surface roughness was not considered, whereas in the *roughness* model, roughness effects were included for strains ranging from 0% to 5%. In this model, the roughness parameters decreased linearly from a predefined initial value to zero at $\varepsilon =$ 5%. For higher strains, the *roughness* model transitioned into the *union* model.

In the case of simulations conducted to calculate the effect of particle polydispersity on the $R(\varepsilon)$ relationship, a mesh with twice-increased element size was used. In simulations involving particle misalignments, the maximum boundary element size was set to 20 μm. All the calculations were carried out using COMSOL Multiphysics 6.2, Structural Mechanics and Nonlinear Materials modules.

2.5. SEM imaging and EDS mapping

Solder balls were examined using a JEOL JSM-7900F field emission scanning electron microscope (SEM) with an accelerating voltage of 5 kV. The lower electron detector was used as it enables the acquisition of images with a 3-dimensional appearance, which helps to gain insight into the roughness from the illumination effects. Energy-Dispersive X-ray Spectroscopy (EDS) was conducted using the Ultim Max 65 detector from Oxford Instruments.

2.6. Profilometry for roughness studies

The Bruker DektakXT system, positioned on a pneumatic table, was used to measure surface roughness of solder balls. The results included three measurements of four different particles' surfaces ($Sn_{63}Pb_{37}$, 760 μm). The stylus was moved by tens of micrometers in the XY plane to prevent repeated measurements of the same line. All measurements were conducted with a constant force of 3 mg, a measurement length of 400 μm, a duration of 120 s, and a stylus diameter of 2.5 μm. In the results section, data from only two exemplary measurements are presented, although all the data were used to estimate the roughness parameters.

2.7. Force-strain measurements

The mechanical properties of the solder balls were analyzed using an MCR302e Anton Paar rheometer configured in a plate-plate setup. The rheometer's specifications include a maximum normal force capacity of 50 N and a maximum compression velocity of 1 mm/s. For particle positioning, we consistently placed the solder balls in the central part of the measuring shaft. Temperature control during experiments was maintained using a Peltier device with active heating, enabling precise adjustments from −25 to 220 °C. Before each experiment, a stabilization period of approximately one minute was observed to allow the temperature of the micro-particles and their surroundings to equilibrate. The data presented in Fig. 8a is processed experimental data, with each measurement repeated three times. A polynomial curve was fitted to the raw data points to standardize X-axis values, followed by averaging. Standard deviations were omitted from the figure for clarity but are typically below 5%.

3. Results and discussion

3.1. Theoretical model and its accuracy

We initiated our study by simulating the changes in the ball-ball contact shape, ball-plate contact shape, as well as the shape evolution of the chain particles during compressive deformation. The compression was applied continuously, ranging from 0% to 85%. The simulation results, shown in Fig. 2**a**, demonstrate that as the particles undergo compression, their shapes transition from spherical to disc-like, ultimately reaching an oblong form.

The black area marked on the top view of the chain (middle row in panel a) represents the contact area, denoted as A_1, between the spheres and the pressing plate. By analyzing A_1, we can gain insights into the electrical resistance between the conductive particles and the measuring pads as they are pressed together (refer to Section 3.2). Visual tracking of the changes in A_1 allows for easy cross-checking of the compression level in the experiment. Furthermore, in the angle view of the chain (bottom row in panel a), the contact area between neighboring spheres is depicted in blue and denoted as A_2. Monitoring the variations in A_2 provides information on the impact of changes in electrical conductance as the compression level alters.

As a result of compression, the shapes of both A_1 and A_2 undergo a transition from circular shapes to oblong shapes. This evolution in shape can be observed more vividly in **Movie S3** and **Movie S4**, where the progressive compression of the chain is captured. Fig. 2**b** provides a quantitative analysis of this transition, allowing us to study the changes in A_1 and A_2 as a function of the compression strain, denoted as $\varepsilon = \Delta h/2r \cdot 100\,[\%]$, where r is the initial radius of the spherical particle. It is evident that, for lower values of ε, the size of A_1 exhibits a faster growth rate compared to A_2. Furthermore, throughout the entire range of ε values, the size of A_1 consistently exceeds that of A_2 significantly. Notably, as ε approaches zero, A_1 tends toward zero, whereas A_2 converges to a finite value (see the inset of Fig. 2**b**). This assumption was made for practical reasons. In reality, it is difficult to assume an infinitely small, point-like contact between the spheres at $\varepsilon = 0$. Therefore, a submicron contact was assumed instead.

Notably, the morphological transition of the chain particles during compression is not limited to the contact areas alone. Fig. 2**c** illustrates the relationship between the aspect ratio ($h : w$) of a particle and the compressive strain. The aspect ratio, defined as the ratio between the height (h) and the width (w) of the particle measured across the structure at the center of the particle, demonstrates how the particles undergo shape transformations throughout the compression. This visualization of the aspect ratio evolution can be further explored in **Movie S5**.

In order to evaluate the correspondence between simulation results and real-world behavior, we compared the contact areas A_1 and A_2 obtained from simulations with experimental data. Initially, A_1 was directly observed and analyzed using optical microscopy, allowing for a straightforward comparison of its shape transitions. In Fig. 3**a**, we present stacked images of simulated shapes at three different compression levels superimposed on images captured from above through a

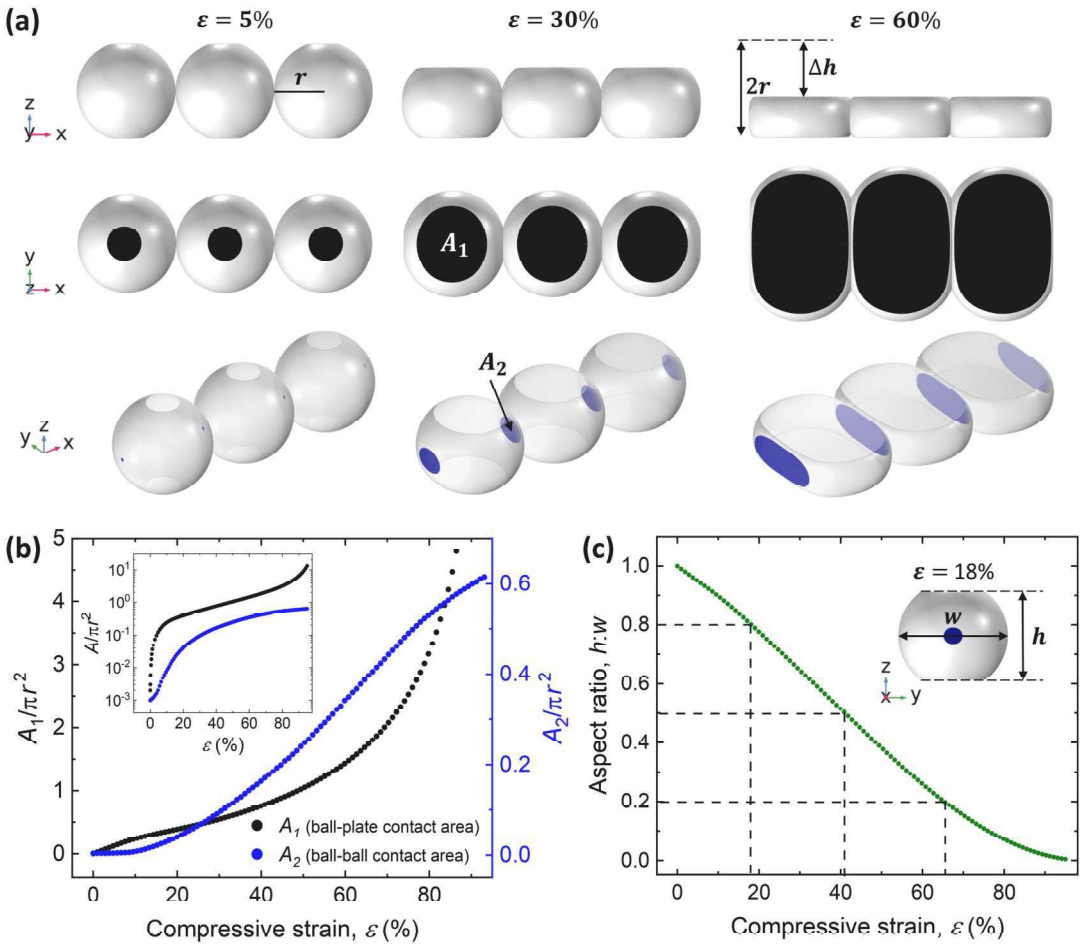

Fig. 2. The results from the COMSOL simulations on the compressive deformation of a particle chain. (**a**) Side view, top view, and angle view of three particles comprising an infinitely long chain under different magnitudes of compressive strain, denoted as $\varepsilon = \Delta h/2r \cdot 100[\%]$, where r is the initial radius of the spherical particle. The contact areas between the compressing wall and the particle (A_1) and between two adjacent particles (A_2) are indicated with black and blue colors, respectively. (**b**) The dimensionless areas, normalized to the initial ball surface, as a function of ε. See also the corresponding **Movie S3** and **Movie S4** for additional visual representation. (**c**) The aspect ratio $h : w$ as a function of ε. See also the corresponding **Movie S5**. (For interpretation of the references to colour in this figure legend, the reader is referred to the web version of this article.)

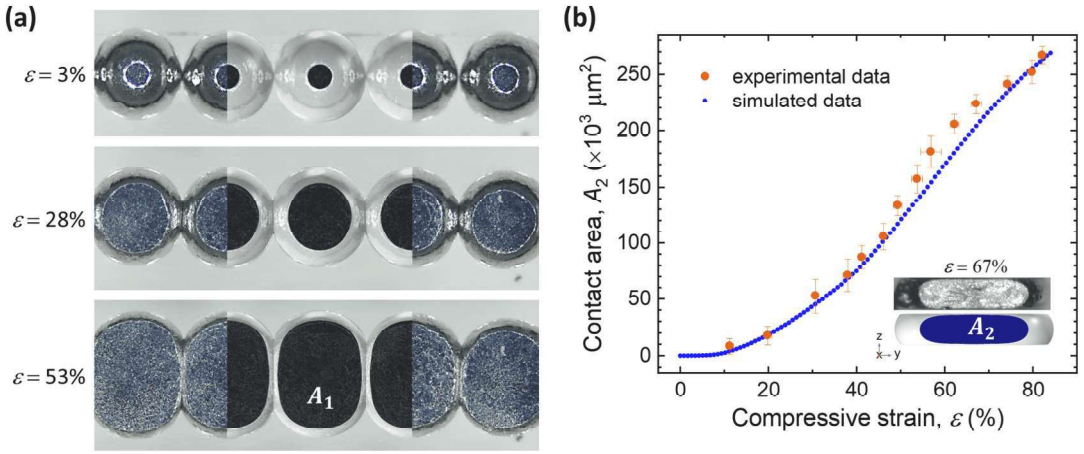

Fig. 3. (**a**) Top-view images of aligned 760-μm solder balls at three different levels of compressive strain (ε), captured through a transparent glass slab. The overlaid COMSOL-simulated shapes closely match the experimentally observed deformations, validating the accuracy of the numerical model. The black regions represent the contact area between the particle and the compressing wall (A_1). (**b**) Contact area (A_2) as a function of compressive strain (ε) for both experimental (orange points) and simulated data (blue line). The inset presents a comparison of an experimentally obtained and a simulated particle shape at $\varepsilon = 67\%$, with the blue region indicating A_2, the contact area between adjacent particles. (For interpretation of the references to colour in this figure legend, the reader is referred to the web version of this article.)

transparent glass slab containing aligned 760-μm solder balls. Remarkably, the simulated shapes closely align with the shapes of the solder particles, providing strong evidence for the reliability and accuracy of the simulation results.

The assessment of A_2 posed a challenge due to the opacity of the particles, which impeded direct measurement of the contact between them. Despite this limitation, the comprehensive evaluation of A_2 was addressed through alternative means. Specifically, we employed experimental techniques involving careful detachment of neighboring solder balls after each compression step. Subsequently, we utilized optical microscopy to measure A_2, albeit with inherent uncertainty due to experimental factors (see Fig. 3**b**). While acknowledging the inherent limitations and uncertainties associated with the experimental measurements, we observed that the trends and range of measured A_2 values were consistent with the simulation outcomes. This convergence between the experimental and simulated results indicates the validity of the chosen material model and simulation parameters and their ability to accurately capture the system's behavior under investigation.

3.2. Resistance measurements and computer simulations

The experimental setup (described in Section 2.3) enabled accurate measurements of the resistance of a particle chain undergoing compressive deformation using a quasi-four-probe technique. It was designed to significantly reduce measurement errors caused by probe and circuit resistance. Nevertheless, this approach does not fully decouple the contact resistance at the electrode pad-particle interfaces (*i.e.*, at the beginning and end of the particle chain) from the chain resistance. Therefore, the contact resistance between the particle and Cu pad ($R_{c\_pad-ball}$) could initially be considered a concern.

However, two important considerations must be noted. As mentioned in the previous section, the ball-plate contact area (A_1) increases at a faster rate than the ball-ball contact area (A_2), and $A_1 \gg A_2$ throughout the entire range of deformation. Thus, the contribution from $R_{c\_pad-ball}$ to the total resistance measured by the LCR meter should be insignificant. To verify this assumption, we conducted an experiment where two solder balls, each placed on one of the Cu pads, were pressed from above using an electrically conductive Cu slab (see **Fig. S5a**). The results presented in **Fig. S5b** demonstrate that the contribution from the contact resistance $R_{c\_pad-ball}$ is small compared to the total resistance value and can be neglected. Secondly, the pads are approximately 30 μm thick, meaning that the solder balls placed on them experience small compression first. This ensures a good electrical contact between the balls and the Cu pads before interparticle contacts are formed. Taking these factors into consideration, we conclude that the resistance of the particle chain can be accurately obtained using our experimental setup.

We initiated the actual measurements by depositing solder balls on the PCB carrier (Fig. 4**a**). In their as-deposited state, the particle chains had a measured resistance on the order of 10^8 Ω. However, our LCR meter produced unstable and fluctuating readings in this state, similar to those recorded when no particle chain was present. This indicates that

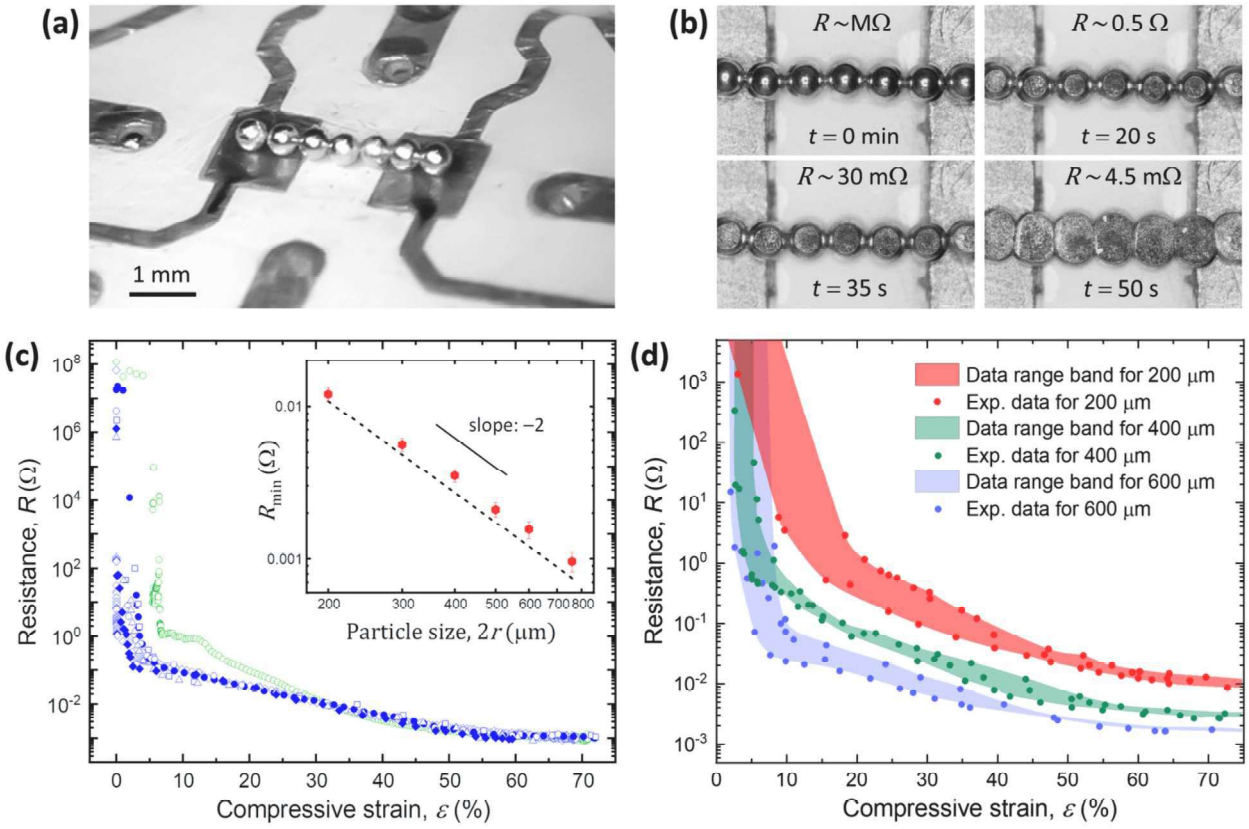

Fig. 4. (**a**) An optical image of a particle chain composed of 600-μm $Sn_{63}Pb_{37}$ spheres, stretched between two copper pads. (**b**) Top-view images showing the compressed chain composed of 350-μm $Sn_{63}Pb_{37}$ spheres at four different stages, corresponding to compressive strains of 0%, 6%, 25% and 65%. Refer to **Movie S6** for a corresponding visual representation. (**c**) The resistance R of a deformed chain composed of 760-μm spheres as a function of ε. The inset graph illustrates the relationship between the minimum resistance R_{min} (at $\varepsilon = 70\%$) and the initial particle size $2r$, demonstrating a quadratic correlation between these parameters, $R_{min} \propto r^{-2}$. The dashed line represents the theoretical resistance values of a solid wire cylinder (of the same solder material) having the same volume as a particle chain. The data series with green open circles corresponds to an experiment in which a small intentional gap (~1 μm) was introduced between two adjacent particles in the chain. This was done to investigate its effect on the threshold strain value at which a sharp drop in resistance occurs. The resistance data were smoothed using a moving average over 20 points and plotted every 5 points to enhance the figure clarity. (**d**) Three sample data series for microparticles with diameters of 200, 400, and 600 μm. (For interpretation of the references to colour in this figure legend, the reader is referred to the web version of this article.)

the electrical contact between neighboring particles is either extremely weak or absent, with the data suggesting it is predominantly absent. As a result, the resistance in this state is effectively immeasurable rather than merely high.

To investigate the evolution of resistance under compression, we then lowered the glass slab at a rate of ~1 μm/s to compress the particle chains. The shape of each particle chain was monitored from above along the compression direction (see Fig. 4**b**), while the electrical resistance was recorded simultaneously.

In Fig. 4**c**, we present the resistance values (R) obtained from five independent experiments on chains composed of 760-μm particles. A significant decrease in resistance is observed as the chain undergoes compression. The resistance reaches several hundred milliohms (mΩ) at just a few percent strain, while the microparticles remain nearly spherical, and the connections between them are barely discernible. With further compression, the resistance decreases by an additional two orders of magnitude, reaching approximately 1.2 mΩ at 60% compressive strain. Beyond this point, further compression does not significantly affect the resistance.

Next, we repeated the experiment for multiple particle chains, each with different particle sizes (200 μm, 300 μm, 400 μm, 500 μm, 600 μm, and 760 μm), compressing them to $\varepsilon \approx 70\%$. As noted above, the resistance exhibits small changes at higher deformations. Fig. 4**d** presents three representative data series for microparticles with diameters of 200, 400, and 600 μm.

Additionally, in the inset of Fig. 4**c**, we plotted the minimum resistance values (R_{min}), measured at the maximum compressive strain ($\varepsilon \approx 70\%$), as a function of particle size. As expected, R_{min} scales inversely with the square of the particle radius, following $R_{min} \propto r^{-2}$. Notably, the experimental values of R_{min} align closely with the theoretical resistance of a solid wire made of the same material, having a cross-sectional area S comparable to A_2 of the corresponding compressed chain. This agreement, indicated by the dashed line in the inset of Fig. 4**c**, arises because the highly compressed particle chain effectively resembles a thin conductor with a uniform cross-section, as depicted in **Fig. S6**. Given this behavior, we can approximate R_{min} using the standard resistance formula for a solid wire: $R = \rho \cdot L/S$, where ρ is the resistivity of the material, L is the length of the resistor, and S is the cross-sectional area. Since a highly compressed particle chain effectively behaves as a continuous conductor, its resistance can be estimated by substituting its theoretical cross-section A_2 with S of a solid wire. Alternatively, R_{min} can be derived from the total volume of the beaded chain. If we assume that the final shape of the compressed particle assembly resembles a compressed cylindrical wire, its cross-section can be inferred accordingly. This approach provides a straightforward way to estimate resistance without requiring direct microscopic measurements of the contact area.

A relevant question is how these resistance values compare to those of microtracks fabricated from sintered nanoparticle-based pastes. It is important to emphasize that the typical resistivity of sintered nanoparticle-based pastes, regardless of their composition (*e.g.*, nanoAg, nanoCu, or nanoAu), are approximately 5 to 15 times higher than the resistivity of the bulk material from which the nanoparticles are made [52,53], see also **Fig. S7**). This implies that the resistance of a microtrack made from nanoparticle-based silver, copper, or gold pastes—assuming a cross-section equivalent to that of a microtrack made from compressed microparticles (Fig. 4**c**, compressed to $\varepsilon > 60\%$) and of the same length as in our experiment—would fall within the range of approximately 0.5 mΩ to 1.5 mΩ. Remarkably, despite their intrinsic conductivity being approximately ten times lower than that of Ag, Au, or Cu, microtracks composed of compressed solder microparticles exhibit a comparable order of magnitude in resistance to those fabricated from costly and unsustainable nanoparticle-based composite pastes (or inks). This highlights the potential of compressed microparticles as an alternative, cost-effective solution for conductive tracks.

Although at high compressive strains the measured R values remain consistent across different measurement trials (using the same particle type and size), an initial sharp drop in resistance is observed at varying strain values, typically at $\varepsilon < 3\%$ (see Fig. 4**c**). Assuming that variations in oxide layer thickness among different microparticles are minimal—and that its behavior during compression is similar across experiments with the same particle type—we do not attribute these discrepancies in initial ε to the presence of the passivation layer. Instead, we hypothesize that these discrepancies arise from the initial arrangement of microparticles prior to measurement, particularly the possible presence of small interparticle gaps. Although the microparticle chain, after forming on the PCB carrier, was carefully examined under the highest available microscope magnification before measurement, particles that appeared to be in contact may still have contained microscopic gaps or may have formed them during the initial compressive contact with the glass slab.

Given this, we found it important to examine how the radial dimension of an individual microparticle evolves as a function of compressive strain ε. To investigate this, we simulated the compressive deformation of a single microball, and the results are presented in Fig. 5. As shown in Fig. 5**b**, the relative change $\Delta r/r$ remains minor during the first few percent compression, which aligns with intuitive expectations. However, the exact magnitude of these changes is not immediately obvious. The inset in Fig. 5**b** presents a semi-logarithmic plot, providing a clearer view of the slow progression of changes at low compressive strain. Specifically, Δr (for the microparticle with an initial size of 760 μm) increases by approximately 100 nm within the first 5% strain.

To further investigate the role of interparticle gaps, we conducted an experiment in which a deliberate ~ 1 μm gap was introduced between two particles within a chain of eight microparticles. In this case, the initial strain at which a drop in resistance was observed (green open circles in Fig. 4**c**) occurred around 7%, which aligns with the numerical

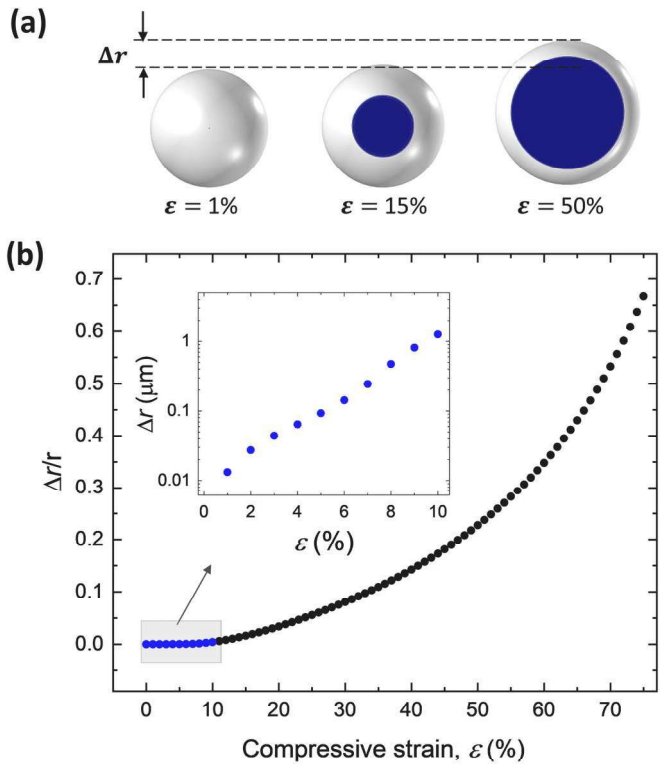

Fig. 5. (**a**) Visualization of the simulated compressive deformation of a single microparticle for different compressive stain levels. (**b**) Normalized radial deformation ($\Delta r/r$) as a function of compressive strain (ε), illustrating a gradual initial increase followed by a more pronounced deformation at higher strain values. The inset presents a lin-log plot of Δr (in micrometers) *vs.* ε, highlighting the minimal changes in radial deformation within the first few percent of strain.

predictions in Fig. 5**b**.

The analysis of the obtained results indicates that the smaller the microparticles, the smaller the relative changes in $\Delta r/r$. Consequently, for the same interparticle gap (*e.g.*, 1 μm), smaller particles must undergo greater compression (*i.e.*, require a higher ε) to fill the gap. This effect may explain why, in our experiments, a significant drop in resistance for 200-μm particles was observed only at strains exceeding 5% (see Fig. 4**d**).

Additionally, preliminary experiments revealed a dependence of resistance values on the length of the particle chain, particularly at low and intermediate strain levels. To investigate this effect, experiments were conducted using short chains composed of only three particles, with two in direct contact with the electrical pads. For 760-μm particles, the resistance vs. strain plot (Fig. 6**a**) shows that resistance values for this three-particle chain (open circles) significantly deviate from those obtained for longer chains (including two additional particles), in the initial and intermediate strain range (up to approximately 35%). However, at higher strain levels, the resistance values begin to converge, suggesting that the influence of chain length is most pronounced in the early stages of deformation.

This behavior is attributed to the fact that the two outer particles of the three-particle chain experience fewer mechanical constraints, allowing the chain to stretch more freely in different directions. As a result, the formation of electrical contacts between particles is delayed due to lower interparticle pressure and a smaller interparticle contact area, leading to higher resistance values at low and intermediate strains. The optical images in Fig. 6**b** and Fig. 6**c** illustrate these effects, showing top-view images of the three-particle chain and a longer chain at $\varepsilon =$ 5% and $\varepsilon =$ 65%. In the unconstrained chain, the particles adjust their positions more freely, while in the longer, mechanically constrained chains, deformation is more uniform, facilitating earlier formation of electrical contacts.

Additionally, we conducted an experiment in which a four-particle chain was initially formed, and a single additional particle was deliberately positioned at a small distance from the fourth particle, creating a gap of several microns. This setup ensured that, during the initial phase of compression, only the four-particle chain contributed to conduction. Once the strain reached $\varepsilon =$ 25%, the fifth particle came into contact with the chain (see Fig. 6**d**), introducing a mechanical constraint and limiting further elongation along the chain axis. This transition is clearly reflected in Fig. 6**a**, where a drop in resistance is observed at $\varepsilon =$ 25% as the fifth particle becomes part of the conductive network.

Next, we investigated the behavior of $R(\varepsilon)$ for microparticles composed of different materials, including lead-free solder (760 μm) and silver (500 μm). Fig. 7**a** shows top-view images of compressed chains formed by different particles. Notably, in both SAC305 and silver particle experiments, the contact formation between the particles and the compressing glass slide appears more irregular compared to $Sn_{63}Pb_{37}$ (see also the corresponding **Movie S7**). This suggests that the deformation behavior of SAC305 and silver differs from that of $Sn_{63}Pb_{37}$, leading to asymmetrically shaped contact surfaces.

SAC305, a hypoeutectic alloy, exhibits a heterogeneous microstructure with tin-rich phases and hard intermetallic compounds (Ag_3Sn, Cu_6Sn_5), resulting in non-uniform mechanical behavior and less spherical deformation [20]. Another possible contributing factor is the adhesion mechanism to the substrate. Yet, a similar asymmetry is observed when a microparticle is compressed against a copper pad (see **Fig. S8**), suggesting that adhesion is not the dominant factor. The asymmetrical deformation occurs regardless of whether the microparticle is compressed by glass or copper. However, as shown by the experimental data, this does not significantly affect the results. The data from experiments using SAC305 (magenta points from two experiments) remain comparable to those obtained for leaded solder (blue points from six experiments).

As shown in Fig. 7**b**, the electrical resistance of a chain formed from silver particles decreases sharply upon contact formation. Due to the sampling rate of 10 measurements per second, no intermediate resistance values were recorded between the open circuit state and resistances on the order of hundreds of milliohms. At high strain levels, the R seems to approach the calculated resistance for a compressed silver cylinder with the same mass as the chain structure (green dashed line). However, since the sensitivity limit of the LCR meter is approximately 1 mΩ, further decreases in resistance beyond this threshold cannot be accurately resolved. Notably, the resistance measured for a silver particle chain compressed beyond 50% strain is an order of magnitude lower than typical resistance values obtained from nanosilver pastes for structures of similar volume.

The above experiments were conducted by manually arranging dry microparticles. To assess the impact of a fluid forming capillary bridges between neighboring particles (and also between the particles and the substrate) on the $R(\varepsilon)$ relationship, we conducted additional experiments in which microparticles were deposited on a PCB carrier. A drop of ethanol was placed on the carrier just before the microparticles were positioned and arranged. Ethanol was left to evaporate before measurement. No significant differences in resistance were observed between dry particle deposition and ethanol-assisted deposition after

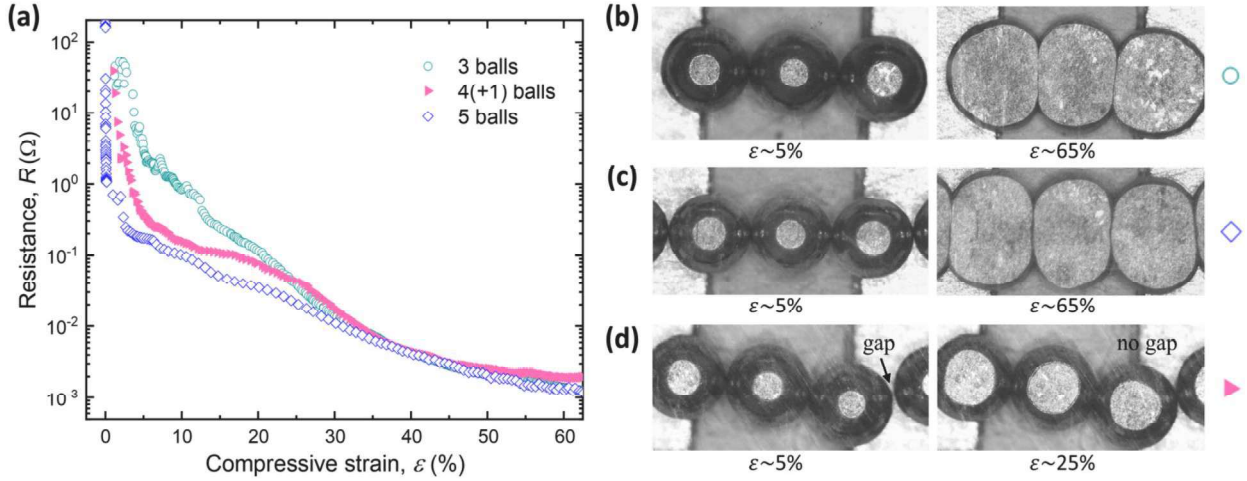

Fig. 6. (**a**) $R(\varepsilon)$ relationship for chains composed of 3, 4(+1), and 5 solder microparticles. Shorter chains exhibit higher resistance at low and intermediate strain. The resistance data were smoothed using a moving average over 20 points and plotted every 2 points to enhance the figure clarity. (**b, c**) Top-view images of a three-particle chain (**b**) and a longer, mechanically constrained chain (**c**) at ε~5% and ε~65%, highlighting differences in deformation and contact formation. (**d**) A four-particle chain with an initially separated fifth particle, which joins the conductive network at ε~25%, reducing resistance.

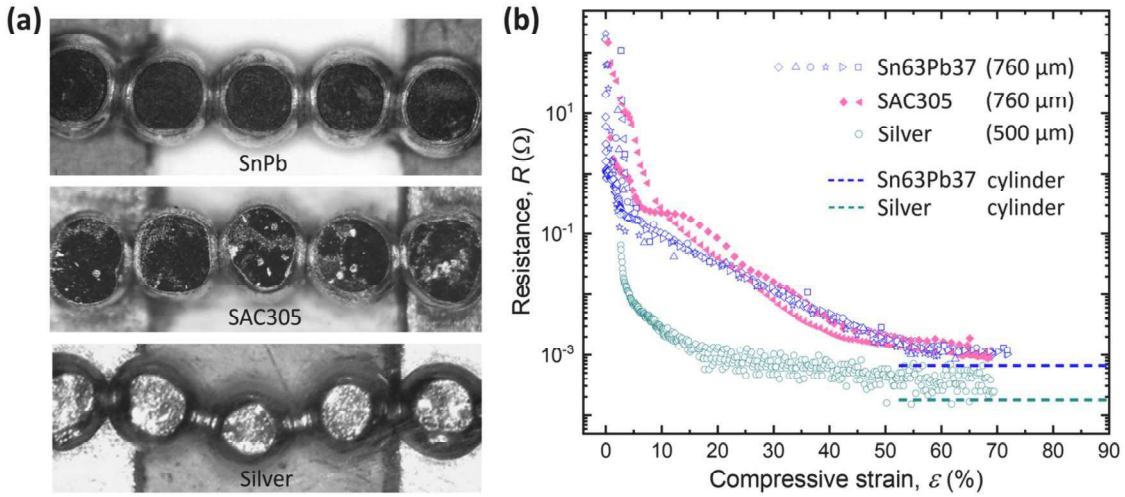

Fig. 7. (**a**) Top-view images of compressed chains of $Sn_{67}Pb_{37}$, SAC305, and silver microparticles. The contact regions in SAC305 and silver appear more irregular compared to $Sn_{67}Pb_{37}$. (**b**) Electrical resistance as a function of compressive strain for chains composed of $Sn_{67}Pb_{37}$ (blue), SAC305 (magenta), and silver microparticles (green). The dashed lines correspond to calculated resistance values for compressed cylindrical structures with equivalent mass. The resistance data for solder particles were smoothed using a moving average over 30 points and plotted every 5 points to enhance the figure clarity. In contrast, the data for silver microparticles were not smoothed to highlight the scatter in values at and below approximately 1 mΩ. (For interpretation of the references to colour in this figure legend, the reader is referred to the web version of this article.)

complete evaporation. However, when the ethanol was not allowed to fully evaporate, the results differed, as shown in Fig. 8**a**. Given that ethanol is not a good conductor, its presence should not drastically affect the results. A similar reduction in R was observed when the liquid used was black glycol-based ink (Fig. 8**b**), further supporting the idea that the low conductivity of the liquid itself is unlikely to be responsible for the observed changes.

In addition, we conducted an experiment to observe how the A_1 contact area forms when a particle is immersed in a liquid containing a black pigment for visualization. As shown in **Movie S8** and **Fig. S9**, the liquid does not appear to penetrate the contact surface but is instead expelled from this region. Although we cannot definitively determine the exact mechanism at play, the results indicate that the presence of liquid influences the $R(\varepsilon)$ relationship.

Next, we conducted experiments in which microparticles were assembled using an electrical method [25], with the particles dispersed in silicone oil. We performed several experiments, and in most cases, the resistance values in the low strain range were lower than those observed for dry particles. A representative result is shown as blue triangles.

To interpret the experimental results presented in Fig. 4 and Figs. 6–8, it is important to note that, unlike $R_{\min}$, the resistance values of a particle chain deformed at compressive strains below approximately 70% cannot be analytically estimated. This limitation arises from the non-uniform, periodically varying cross-sectional area along the chain. The minimum cross-sectional area occurs at the particle joints, while the maximum is at the center of each particle, halfway between the joints. Given this variability, accurately determining R in this strain range is non-trivial. To address this, we simulated R as a function of ε using the previously simulated shapes of particles in a chain.

As a first approximation, we considered a straight chain with the contacts between solder balls to be ideal and fully conductive, neglecting weak connections caused by microscopic imperfections such as air gaps and contaminants, which can act as insulating barriers. We also disregarded surface irregularities that may impede the flow of electric

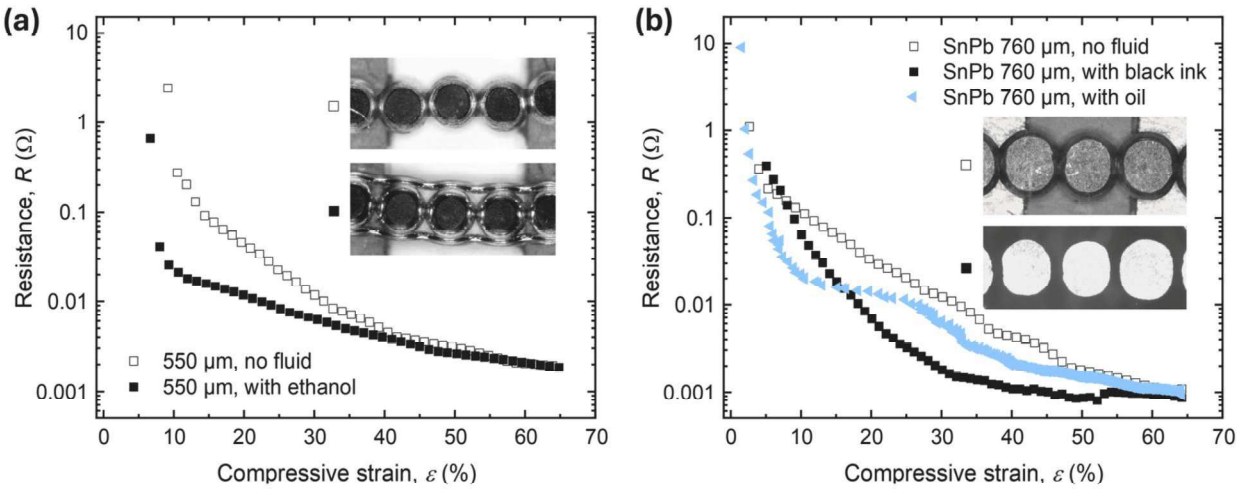

Fig. 8. $R(\varepsilon)$ relationship for microparticle chains composed of (**a**) 550 μm and (**b**) 760 μm solder particles, formed in dry conditions (open squares), in the presence of ethanol (solid squares), in black glycol-based ink (black squares), and in silicone oil (blue triangles). The insets present corresponding top-view images of compressed chains. The presence of liquid seems to facilitate better contact between particles and a reduction in resistance in the lower strain range. (For interpretation of the references to colour in this figure legend, the reader is referred to the web version of this article.)

current. That is, we assumed that the mechanically flattened region formed between spheres due to compression (A_2) corresponds to the electrical contact area (A_{el}).

The simulation results (model 'union', dashed red line in Fig. 9) closely match the experimental data obtained for silver microparticles (green open circles in Fig. 9**a,c**), with deviations occurring only at small strain values. In contrast, for solder particles, the experimental data significantly deviate from the simulation results over a wide range of strains (Fig. 9**b,d**).

In this simulation, we assumed that the total chain resistance consists solely of the material resistance, determined by its bulk properties and shape function. However, in actual measurements, the total resistance R is the sum of the material resistance and constriction resistance, given by: $R = R_{material} + R_{constriction}$, where $R_{material}$ is dictated by the intrinsic resistivity of the material and the geometry of the spheres, while $R_{constriction}$ arises due to the limited number of conducting paths at the contact points between neighboring particles.

One major contributor to $R_{constriction}$ is surface roughness, which may have an impact, particularly at low strains, when initial contacts are being formed, and the real electrical contact area is still small. In numerical simulation tools like COMSOL, roughness can be incorporated either as a fixed parameter (through average roughness and root mean square roughness) or as a function of strain. For the materials used in this study, roughness is expected to evolve with ε rather than remain constant, as mechanical compression significantly alters the initial roughness. However, experimentally determining roughness as a function of strain is non-trivial, and we found no relevant literature data.

Despite this limitation, we chose to simulate the effect of roughness by adopting a simplified assumption: we assumed roughness varies linearly from an initial value at $\varepsilon = 0\%$ to zero at a certain strain value, which can be estimated based on Fig. 5, using the average roughness value as a reference. To determine this initial roughness value, we performed SEM imaging and mechanical profilometry of the solder microball surfaces. The following roughness parameters were obtained: an average surface roughness of approximately 200 nm and a peak roughness height of approximately 0.5 μm (refer to SEM imaging and profilometry in **Fig. S10**). It can therefore be assumed that such roughness can be flattened by deforming the microball to approximately $\varepsilon \approx 5\%$ (assuming a diameter in the range of several hundred micrometers). Consequently, in our simulations, we assumed a strain value of 5%, at which the roughness parameters are considered to reach zero.

Roughness was implemented in the COMSOL Electric Currents module using the Cooper-Mikic-Yovanovich (CMY) correlation. Although originally developed for thermal contact conductance, the CMY correlation provides a reasonable approximation for electrical contact resistance in rough surfaces [54]. The input parameters included average roughness, root mean square roughness, microhardness, and deformation characteristics. Additionally, the simulation required microhardness data for the solder material. We incorporated a Micro-vickers Hardness Number (HV) of 11.5, consistent with reported values in the literature. The obtained simulation results, shown as black solid lines in Fig. 9, indicate improved agreement with experimental data at low strains.

Notably, the experimental data for the compressed silver microball show remarkable consistency with the simulated values. An interesting observation is the behavior of the solder microparticles, which is particularly well illustrated in Fig. 9**d**, which reveals three distinct regimes of resistance behavior as a function of the interparticle contact area A_2. In the first regime, corresponding to small A_2 values, resistance decreases very rapidly as the initial electrical contacts are formed. In the second regime, spanning approximately two decades of A_2 values, resistance exhibits only moderate changes, decreasing from approximately 15 mΩ to 7 mΩ. In the third regime, the rate of resistance decline increases again as A_2 further expands. A fourth regime is expected for deformations exceeding 70%, where R decreases only slightly and gradually approach a constant value as strain nears 100%, when A_2 reaches its maximum finite value.

This complex, non-monotonic resistance behavior suggests that additional factors beyond simple geometric considerations may be at play. As seen, the electro-mechanical mechanism appears to be complex and does not seem universal. The resistance values can also be influenced by morphological imperfections, such as dents, and by the cleanliness of the microballs' surfaces. Indeed, the EDS map shown in **Fig. S11** reveals the presence of impurities on the surface of the solder particles. However, we assume that these play only a minor role. The observed complex behavior is strongly material type-dependent.

3.3. Aspect ratio

From the perspective of many practical applications involving

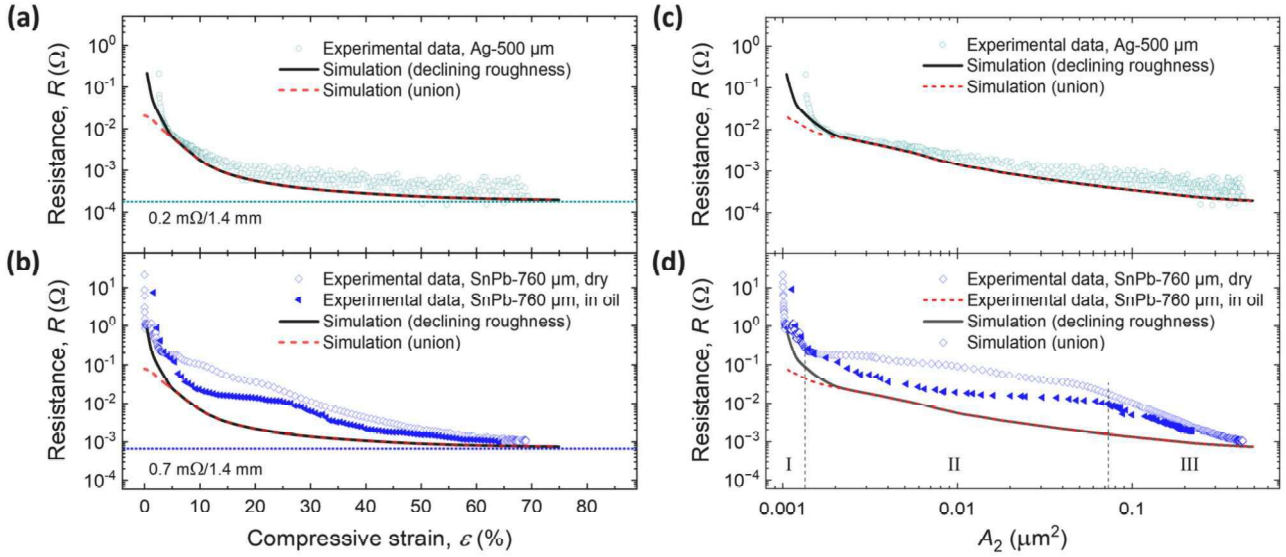

Fig. 9. Resistance R of a deformed chain composed of (**a,c**) 500-μm silver and (**b,d**) 760-μm $Sn_{63}Pb_{37}$ particles as a function of (**a,b**) uniaxial compressive strain ε and (**c,d**) interparticle contact area A_2. The red dashed lines correspond to simulations assuming idealized, fully conductive contacts, while the black lines represent simulations incorporating surface roughness. (For interpretation of the references to colour in this figure legend, the reader is referred to the web version of this article.)

microtracks, it is essential to understand the variation in resistance of particle chains concerning the height-to-width aspect ratio of the conductor. In Fig. 10**a**, we present theoretical results from simulations (without roughness included) that have been normalized by dividing the resistance values by the minimum resistance value, R_{min} (at $\varepsilon = 75\%$). Interestingly, the R/R_{min} ratio drops rapidly, and at a relatively small aspect ratio (1:1.5), the resistance value R is found to be lower than twice R_{min}.

In Fig. 10**b**, we present a plot showing the inverse of the product of the simulated widths (w) of compressed microparticles and the simulated resistance ratios (R/R_{min}) against compressive strain (ε). This analysis helps us determine the optimal strain value (ε) that maximizes conductivity while minimizing shading. Achieving the lowest possible resistance with the narrowest width is essential for applications like incorporating microtracks as fingers and busbars in solar cells. As indicated in Fig. 10**b**, an optimal balance of these parameters is attained at $\varepsilon \sim 48\%$, corresponding to an h:w ratio close to 1:2.5.

3.4. *Effect of chain length, particle misalignment, polydispersity and liquid*

Another important aspect from a practical application perspective is the polydispersity of microparticles. Monodisperse particles are typically more expensive due to either the higher cost of production methods or the additional separation processes required to isolate them from a polydisperse particle distribution. To investigate how particle size polydispersity affects the electrical and mechanical behavior of compressed chains, we conducted additional numerical simulations. In our simulations, we simplified the system to a chain composed of two different microparticle sizes, utilizing symmetry—*i.e.*, larger and smaller particles were arranged alternately within the chain.

Fig. 11**a** presents the $R(\varepsilon)$ relationship for three microparticle size pairs: 760/760 μm (as a reference), 700/760 μm, and 450/760 μm. The corresponding size differences, calculated relative to the reference size of 760 μm, are 0%, 7.9%, and 40.8%, respectively. Interestingly, in the initial strain range, the chain composed of microparticles with the highest polydispersity ($PDI \approx 0.26$) exhibits lower resistance compared to chains with more uniform particle sizes ($PDI \approx 0.04$ and 0), which may seem counterintuitive. This effect can be explained by the way plastic deformation forms at the particle contact points. As shown in Fig. 11**b**, when two identical particles are in contact, they create a macroscopically flat interface. However, in the case of significant size differences, the larger particle undergoes plastic indentation, as depicted in Fig. 11**c**, which is further illustrated in **Movie S9**. This indentation occurs because the volume of the smaller particle near the contact point plastically deforms later in the compression process, due to its higher local hardness and reduced stress concentration compared to the larger particle.

As the strain increases, the resistance of the 760/760 μm chain becomes lower than that of the 700/760 μm chain at $\varepsilon \approx 11\%$ and subsequently lower than the 450/760 μm chain at $\varepsilon \approx 13\%$, remaining the lowest throughout the entire range. The observed reduction in resistance for the monodisperse chain can be directly attributed to the mass of the particles per unit length, which influences the effective conductive cross-section. For large compressive strains approaching 100%, the resistance of the microparticle chains is 0.671 mΩ for the chain composed of 760 μm particles, 0.724 mΩ for the 700/760 μm system, and 0.885 mΩ for the 450/760 μm system, considering a chain length of 1.4 mm, which corresponds to the distance between the electrical pads in the aforementioned experiments.

So far, we have presented results for a linear particle arrangement—perfectly straight in simulations and as close to ideal as possible in experiments. However, in practical applications, deviations from perfect alignment often occur during the deposition of microparticles onto a substrate, leading to slight angular misalignments. To investigate the impact of such deviations on the $R(\varepsilon)$ relationship, we conducted numerical simulations. The simulations were performed for three different zigzag configurations, where the angle between adjacent microparticles, measured as the deviation from a perfectly linear arrangement, was set to 30°, 40°, and 50°, respectively.

The simulation results presented in Fig. 12**a** account for variations in particle arrangement within the chain, affecting the mass per unit length. Since the chain is assumed to be infinitely long with periodic symmetry, we analyze a fixed-length segment that captures its periodicity. As the deviation angle (θ) increases, microparticles become more closely packed along the main axis, increasing the number of microparticles per unit length. This effect is described by:

$$N_\theta = \frac{N}{(N-1)\cdot 2r\cdot\cos(\theta)}$$

where N_θ represents the effective mass per unit length, N is the number of microparticles in the analyzed segment, r is the particle radius, and θ

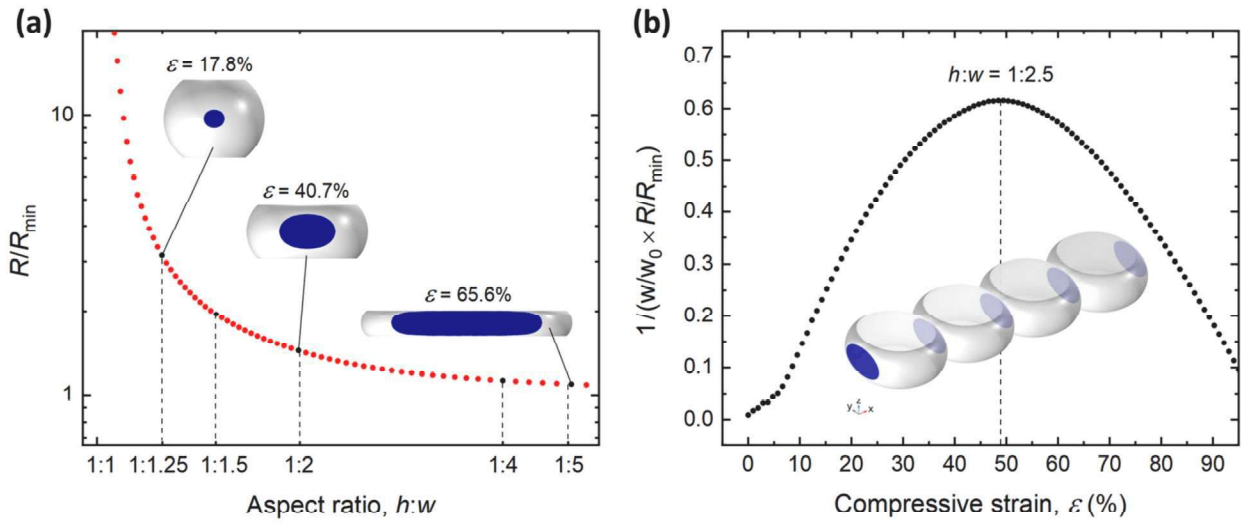

Fig. 10. (**a**) A log–log plot of the normalized resistance, R/R_{min}, as a function of the aspect ratio, $h:w$. (**b**) A plot of the inverse of the product of the simulated widths (w) of compressed microparticles and simulated values R/R_{min} as a function of compressive strain (ε). The plot is instrumental in pinpointing the optimal structural compression for applications like solar cells, where the goal is to maximize conductivity and minimize shading. However, this optimal compression ($\varepsilon = 48\%$) is specific to this use case; other applications might need different compression levels for optimal results.

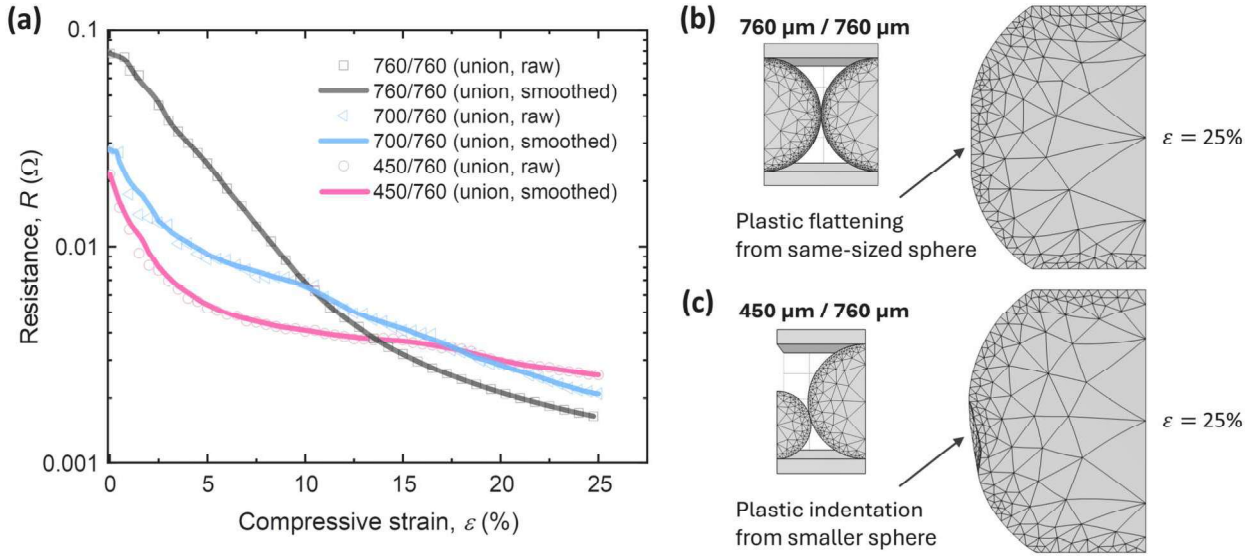

Fig. 11. (**a**) Resistance as a function of compressive strain for microparticle chains with different size ratios: 760/760 μm (reference), 700/760 μm, and 450/760 μm. The resistance is calculated for a chain length of 1.4 mm. (**b**) Plastic flattening at the contact interface for identical particles (760/760 μm) at $\varepsilon =$ 25%. (**c**) Plastic indentation in the larger particle for the 450/760 μm system at $\varepsilon = 25\%$, demonstrating size-dependent deformation mechanisms. See also **Movie S9** for a dynamic visualization.

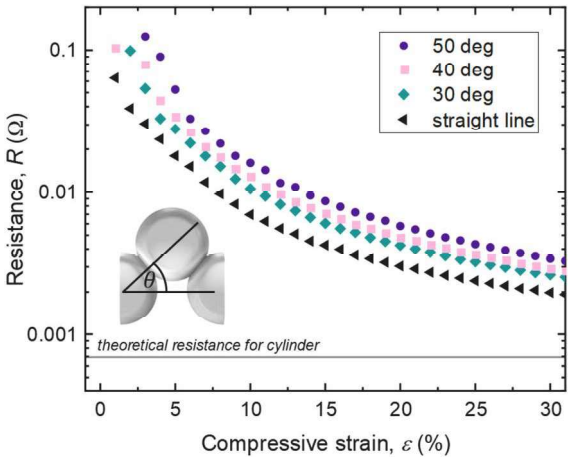

Fig. 12. Simulated resistance as a function of compressive strain for chains with different deviation angles. The resistance is normalized to account for differences in the number of microparticles per unit length. At low strain levels, an increase in the deviation angle results in higher resistance. Inset illustrates the geometric definition of the deviation angle.

is the deviation angle, measured as the angle between the particle alignment and the horizontal axis.

Since the resistance of the chain, measured over a straight-line distance rather than along the chain itself, depends on the mass per unit length, the resistance values in Fig. 12**a** were adjusted to ensure comparability across configurations. Specifically, the raw resistance data for 30°, 40°, and 50° were multiplied by $1/\cos(30) \approx 1.16$, $1/\cos(40) \approx 1.31$, and $1/\cos(50) \approx 1.56$, respectively, to express the resistance in terms of an equivalent linear configuration. For strains approaching 100%, this normalization ensures that a fully flattened structure exhibits the same resistance, as it retains the same mass and volume (assuming that the mechanical compression of chains with different zigzag configurations induces similar volumetric changes). However, at the initial and intermediate strain stages, resistance values differ across the four simulated data series (with angles ranging from 0° to 50°), with the lowest resistance observed for the perfectly linear chain. As the deviation from a linear arrangement increases, the resistance also rises. Representative relative differences in resistance (in percentage) for various zigzag configurations (30°–50°) compared to the resistance of a straight chain are presented in Table 1. As shown, these differences decrease with increasing compressive strain.

3.5. The impact of compressive forces in microtrack formation

As demonstrated in this study, forming conductive paths with microparticles necessitates applying an appropriate mechanical force. The required force magnitude depends on the material properties of the microparticles, as well as on the strain, strain rate, and temperature. In Fig. 13**a**, we present data from an experiment using single solder balls with a diameter of 650 μm, where the strain varied from 0% to 70%. The experiments were conducted at strain rates of 1% per second and 10% per second under two different temperatures: 25 °C and 175 °C.

For malleable materials, higher strain rates can lead to increased resistance to deformation because there is less time for atoms or dislocations in the material to move and adjust to the new structure. Consequently, a higher magnitude of normal force is observed at higher strain rates, as evident in Fig. 13**a**. Specifically, the magnitude of the normal force at a strain of 50% changes from approximately 22 N to 14 N when the rate of sample deformation decreases from 10% to 1% per second. However, a more pronounced change is observed when the temperature is elevated from 25 °C to 175 °C, which is close to the melting point of the material used. In this case, the magnitude of the normal force drops significantly, by more than an order of magnitude, from ~14 N to 0.9 N.

In practical terms, it is crucial to estimate the force due to the strength of the substrate, as excessive pressure on the substrate can lead

Table 1
Calculated relative differences in resistance (in percentage) for various zigzag configurations (30°–50°) compared to the resistance of a straight chain, within the strain range of 5% to 25%.

ε [%]	30°	40°	50°
5	+36%	+47%	+66%
10	+34%	+46%	+57%
15	+30%	+40%	+51%
20	+28%	+37%	+47%
25	+26%	+35%	+45%

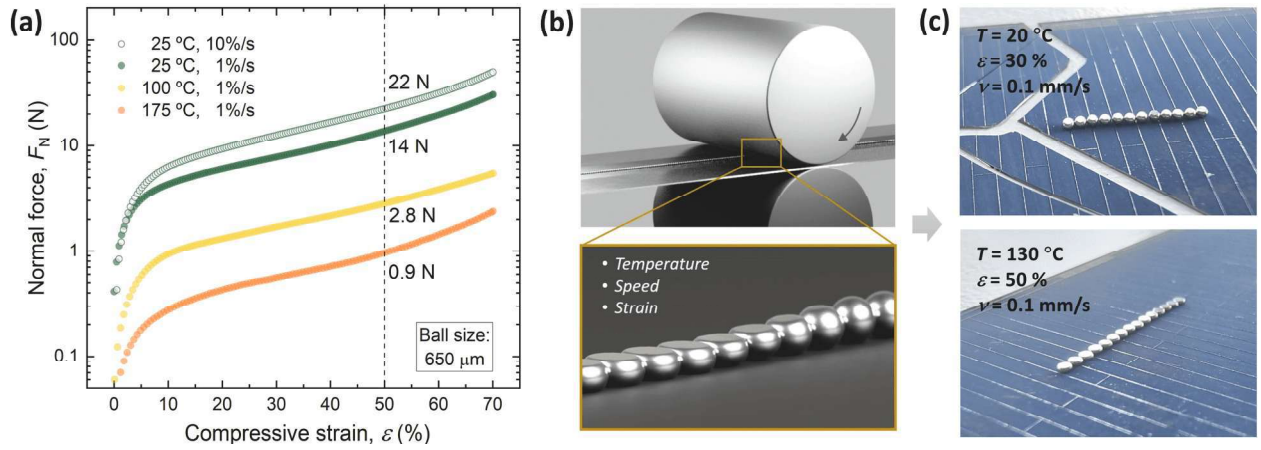

Fig. 13. (**a**) Experimental data of the normal force (F_N) as a function of compressive strain (ε). A single solder particle size 650 μm was pressed with a constant strain rate ($\dot{\varepsilon}$) either 1 s^{-1} or 10 s^{-1}. We also studied the solder particle compression under three different temperatures, 25 °C to 175 °C, at a strain rate of $\dot{\varepsilon} = 1\ s^{-1}$. For the stress–strain studies, we used an MCR300 Anton Paar rheometer with a plate-plate configuration. (**b**) 3D rendering for visualization of the calendaring process. (**c**) Results of calendaring indicate that too rapid calendaring at room temperature causes excessive pressing force on the delicate and brittle silicon wafer of a solar cell (top image). Increasing the temperature effectively eliminates this problem, thereby enabling the creation of a conductive path subjected to compressive strain $\varepsilon =$ 50% (bottom image).

to its damage. We conducted an experiment in which a chain made of 650-μm solder beads was arranged on a 200-μm thick silicon wafer. The bead structure was then subjected to compression using a calendaring device (rollers with a diameter of 10 cm). In the experiments, we varied the roller temperature while maintaining the rolling speed at approximately 0.1 mm/s. When the experiment was conducted at room temperature, the substrate tended to crumble (refer to the top image of Fig. 13**c**). By increasing the temperature to around 130 °C, we enabled the formation of a flattened chain structure without causing damage to the substrate (refer to the bottom image of Fig. 13**d**). Note that in many practical applications, smaller microballs would be used, requiring less compressive force [55], thus allowing an increase in rolling speed. Due to the ease of execution and clarity of the experiment, we used relatively large microballs here. Still, this experiment demonstrates the potential for practical application of our research findings.

4. Discussion and conclusions

This work aimed to understand and explain the impact of uniaxial compression on a chain of malleable microparticles deposited on a substrate, focusing on particle deformation and the resulting alterations in the contact area between neighboring microparticles. This understanding is crucial for grasping the changes in electrical conductivity induced by these alterations. Our findings pave the way for applying particle chain post-processing in developing new conductive structures with optimized electrical conductivity that can be produced through additive processes, such as the electric field-driven particle printing utilized here.

An important contribution of our study is the development of comprehensive numerical simulations, which closely reflect experimental observations of the mechanical deformation of the microparticle chain. This chain, composed of uniformly sized microparticles arranged linearly with initial near-point contacts, was examined in detail first. We showed how alterations in the contact areas due to compression influence electrical conductivity. The initial compression phase, where compressive strain reaches approximately 5%, highlighted the role of contact resistance — affected by the surface roughness of the microparticles — in conductivity. Our simulations that incorporated particle surface roughness provided a more comprehensive understanding of the experimental results.

The conduction mechanisms between compressed metals made of the same material are generally complex, particularly when considering real conditions. Key factors influencing conductivity include changes in pressure at the contact area, the geometry of the compressed elements (*e.g.*, two flat, perpendicular plates versus two spheres), varying surface roughness, the presence of an oxide layer (which is always present in practice, though its thickness depends on the type of material), contaminants, and mechanical imperfections on the surface (*e.g.*, dents or micro-damage). Additionally, the literature describes conduction mechanisms such as tunneling effects, quantum effects, or conduction through microcracks and micro-sparks. In our experiments, however, these mechanisms are not significant, as metallic surfaces contact over relatively large areas, and the compression conditions ensure stable connections between particles. Moreover, we test resistance at a very low voltage (100 mV), which further minimizes the risk of phenomena such as micro-sparks.

Our work does not focus on a detailed description of conduction mechanisms but rather on analyzing resistance changes as a function of mechanical deformation. Nevertheless, we assume that the dominant conduction mechanism is related to the formation of actual conductive contacts. The area of these contacts is always smaller than the mechanical contact area. Even if perfectly smooth surfaces were assumed, this statement still holds true. This occurs because the actual electrical contact area (A_{el}) is proportional to the mechanical contact area (*here* : A_2), with this proportionality depending on local pressure conditions. According to the classical Hertz model for elastic contacts (that assumes perfectly smooth, roughness-free surfaces): $A_{el} \approx A_2 \cdot (P/E^*)^{2/3}$, where P is the local pressure in the contact area, and E^* is the reduced Young's modulus of the material.

For very small strains (below approximately 0.2%), the applied force remains low, resulting in minimal growth of the electrical contact area. In this regime, the electrical contact area is confined to a few points of contact, making conductive pathways sparse and unstable. Once the strain exceeds approximately 0.2% plastic deformation begins and the applied pressure becomes sufficiently high to significantly expand the contact area. This rapid increase arises from the nonlinear dependence of A_{el} on pressure, characteristic of the Hertz model.

Additionally, even for ideally smooth surfaces, thin oxide layers are typically present and can inhibit effective conduction at low contact pressures. As the strain increases and pressure rises, these oxide layers may rupture or become sufficiently thin at the contact points, further enhancing conductivity [56]. In practice, this combination of mechanical deformation, nonlinear contact area growth, and oxide layer disruption explains the observed rapid decrease in resistance once the

strain exceeds approximately 1–2%. We observe in our measurements, particularly for the homogeneous material such as silver, that the resistance decreases rapidly and approaches the theoretical values already at strains of approximately 1%, starting from the first recorded drop in resistance (from an unmeasurable value).

In an industrial context, microparticles often exhibit greater size dispersion and are typically cheaper than monodisperse particles. This raises questions about the impact of polydispersity on the deformation of particles in the chain and their electrical conductivity. Therefore, we also designed studies to determine the effect of particle polydispersity and misalignment from the linear structure.

Our simulations and experimental observations demonstrated that polydispersity does not significantly affect the overall $R(\varepsilon)$ trend. However, an interesting observation emerged: in systems exhibiting polydispersity, the resistance initially decreases faster and reaches lower values than in chains composed of monodisperse particles at low strain levels. This outcome may seem counterintuitive since polydispersity reduces the linear mass of the chain. At high compression levels, approaching the practically unattainable strain of 100%, reduced linear mass naturally leads to higher resistance. Nevertheless, for low strains, polydispersity promotes a faster decrease in resistance. This occurs because the contact area between particles (A_2) increases more rapidly in the early compression stages in polydisperse systems.

Another intriguing finding concerns the presence of liquid surrounding the microparticles. Perhaps counterintuitively, electrically insulating liquids such as silicone oil, glycerin, or ethanol do not adversely affect conductivity; rather, they appear to promote a faster reduction in resistance at low and intermediate strain levels. The underlying mechanism is not yet fully understood; however, our results suggest that liquid presence facilitates a more effective increase in interparticle contact area, thereby improving conductivity in these strain ranges.

It is important to emphasize the high height-to-width (h:w) ratio that can be achieved in the beaded structure. This is particularly crucial for applications such as the production of electrodes in solar panels, as a high aspect ratio yields high conductivity. This occurs because a taller conductive path (relative to its width) has a larger cross-sectional area, which can reduce electrical resistance. In other applications, such as sensors, a higher aspect ratio increases the surface area available for chemical or physical interactions, thereby improving the device's sensitivity or efficiency.

Achieving a high aspect ratio, particularly one as ideal as 1:1, presents significant challenges, especially when working with materials like nanoparticle pastes, including those made of silver. The typical aspect ratio for micropaths created using such pastes or inks usually ranges between 1:20 and 1:5, depending on the process employed. Common issues during critical stages of the fabrication process, such as drying and sintering, include sagging or collapsing of these materials. Advanced fabrication techniques and specialized material formulations are typically required to achieve and maintain such high aspect ratios in practical applications. In this context, very high aspect ratios (*e.g.*, 1:2) can be easily achieved using moderately compressed particle chains, while the structure's conductivity is nearly that of a solid cylindrical wire.

Our research, although fundamental, also holds significant practical relevance. It demonstrates that highly conductive micro-path fabrication can be effectively achieved by aligning microparticles in a 'beaded' structure. This strategy shows considerable advantages over silver nanoparticle pastes for microtracks. As demonstrated here, such paths are characterized by exceptionally high conductivity, comparable to that of solid wire — several times higher than that of typical conductive paths made from silver nanoparticle paste. Moreover, using the patented method of sequential microparticle deposition described in ref. [25], such conductive microparticle paths can be produced efficiently and economically from commonly available and environmentally friendly materials. Notably, compared to the environmental costs of producing silver nanoparticles, commonly used in modern electronics, the environmental cost of producing microparticles is significantly lower.

The knowledge acquired from the experiments presented in the first part of the manuscript — regarding compression parameters such as strain, strain rate, and temperature during the compression process, and their impact on the resistance of a single chain — is directly applicable to the creation of both single-layer and multilayer conductive structures.

The potential practical applications of our findings extend beyond creating highly conductive paths. Unlike solid wires with fixed conductivity, the beaded structures developed in this study offer the unique advantage of adjustable electrical conductivity across a broad range, approaching that of a solid wire. Specifically, the achievable resistance range, where settings are technically optimal and repeatable, spans approximately three orders of magnitude from the minimum value. For structures formed by solder spheres with diameters in the hundreds of micrometers and lengths of several microballs, this corresponds to a resistance range from approximately 1 mΩ to 10 Ω (per 1 mm of length). This capability to finely adjust conductivity enables the use of microparticle chains, for example, as heating elements for various electronic technologies.

Considering certain practical limitations, it should also be noted that when designing particle microtracks, consideration must be given to the final width of the track after appropriate mechanical compression, as this directly impacts the integrated density of wires. The higher the compression level — and thus the greater the track width (w) — the lower the achievable density of wires.

It should also be noted that some materials may be harder to deform than those used in our studies. This is particularly relevant when working with soft or brittle substrates, which may pose a challenge. However, there are ways to address this issue. As demonstrated in the latter part of the manuscript, one solution may involve heating the microparticles to a temperature that allows them to soften and change their rheological properties. This enables compression of the microparticles using significantly reduced force (see also ref. [55]).

At this stage, two important aspects arise: the strength of adhesion to the substrate and the robustness of connections between particles. These factors are currently under investigation (see **Fig. S12a,b**) and will be the focus of future research.

In the spirit of collaborative research and further innovation in materials design and additive manufacturing, we have made all our simulation files available as electronic supplementary material, inviting further analysis and validation by the scientific community.

CRediT authorship contribution statement

Z. Rozynek: Writing – review & editing, Visualization, Validation, Supervision, Resources, Project administration, Methodology, Investigation, Funding acquisition, Data curation, Conceptualization. **Y. Harkavyi:** Writing – original draft, Visualization, Validation, Software, Methodology, Data curation, Conceptualization. **Ø.G. Martinsen:** Writing – review & editing, Resources, Funding acquisition. **K. Giżyński:** Writing – review & editing, Visualization, Validation, Software, Methodology, Funding acquisition, Data curation, Conceptualization.

Declaration of Generative AI and AI-assisted technologies in the writing process

During the preparation of this work, we utilized an AI-powered writing assistant, Grammarly, solely to enhance readability and language clarity. Following the use of this tool, we meticulously reviewed and edited the content. Therefore, we take full responsibility for the content of the publication.

Declaration of competing interest

The authors declare that they have no known competing financial

interests or personal relationships that could have appeared to influence the work reported in this paper.

Acknowledgments

This research was funded by the Polish National Science Centre through OPUS (Grant No. 2019/33/B/ST5/00935) and SONATA (Grant No. 2019/35/D/ST5/03613) programs. We wish to thank CADENAS P. S.A., Poland, for their support in initiating the research, providing access to the company's research infrastructure, and supplying materials. We are thankful to Rafał Zbonikowski for the profilometer measurements. We also extend our gratitude to Marek Woźniak for preparing the 3D rendering that contributed to Fig. 1 and Movie S2.

Appendix A. Supplementary data

Supplementary data to this article can be found online at https://doi.org/10.1016/j.matdes.2025.113985.

Data availability

Data will be made available on request.

References

[1] Y. Khan, A. Thielens, S. Muin, J. Ting, C. Baumbauer, A.C. Arias, A New frontier of printed electronics: flexible hybrid electronics, Adv. Mater. 32 (15) (2020), https://doi.org/10.1002/adma.201905279.
[2] K.T. Fujimoto, J.K. Watkins, T. Phero, D. Litteken, K. Tsai, T. Bingham, K.L. Ranganatha, B.C. Johnson, Z. Deng, B. Jaques, D. Estrada, Aerosol jet printed capacitive strain gauge for soft structural materials, npj Flexible Electronics 4(1) (2020) 32, 10.1038/s41528-020-00095-4.
[3] M.M. Hasan, M.M. Hossain, Nanomaterials-patterned flexible electrodes for wearable health monitoring: a review, J. Mater. Sci. 56 (27) (2021) 14900–14942, https://doi.org/10.1007/s10853-021-06248-8.
[4] H.T. Qin, J.Y. Dong, Y.S. Lee, Fabrication and electrical characterization of multi-layer capacitive touch sensors on flexible substrates by additive e-jet printing, J. Manuf. Process. 28 (2017) 479–485, https://doi.org/10.1016/j.jmapro.2017.04.015.
[5] W. Yang, X. Cheng, Z. Guo, Q. Sun, J. Wang, C. Wang, Design, fabrication and applications of flexible RFID antennas based on printed electronic materials and technologies, J. Mater. Chem. C 11 (2) (2023) 406–425, https://doi.org/10.1039/D2TC03736J.
[6] M. Lee, C. Kim, W. Park, J. Cho, J. Paik, Y. Jeong, Energy harvesting performance of unimorph piezoelectric cantilever generator using interdigitated electrode lead zirconate titanate laminate, Energy 179 (2019) 373–382, https://doi.org/10.1016/j.energy.2019.04.215.
[7] H. Lee, W. Jin, M. Ovhal, N. Kumar, J. Kang, Flexible transparent conducting electrodes based on metal meshes for organic optoelectronic device applications: a review, J. Mater. Chem. C 7 (5) (2019) 1087–1110, https://doi.org/10.1039/C8TC04423F.
[8] S. Tepner, A. Lorenz, Printing technologies for silicon solar cell metallization: A comprehensive review, Prog. Photovolt. Res. Appl. 31 (6) (2023) 557–590, https://doi.org/10.1002/pip.3674.
[9] https://www.silverinstitute.org/category/press-releases/- search for "Global Silver Industrial Demand Forecast to Achieve New High in 2023" [Accessed 7 Jan 2024].
[10] Metals Focus World Silver Survey 2023, The Silver Institute, Washington, D.C. 20005, USA, 2023,.
[11] J.C. Goldschmidt, L. Wagner, R. Pietzcker, L. Friedrich, Technological learning for resource efficient terawatt scale photovoltaics, Energ. Environ. Sci. 14 (10) (2021) 5147–5160, https://doi.org/10.1039/D1EE02497C.
[12] E. Gervais, R. Kleijn, S. Nold, E. van der Voet, Risk-based due diligence in supply chains: The case of silver for photovoltaics, Resour. Conserv. Recycl. 198 (2023) 107148, https://doi.org/10.1016/j.resconrec.2023.107148.
[13] B. Hallam, M. Kim, Y. Zhang, L. Wang, A. Lennon, P. Verlinden, P.P. Altermatt, P. R. Dias, The silver learning curve for photovoltaics and projected silver demand for net-zero emissions by 2050, Prog. Photovolt. Res. Appl. 31 (6) (2023) 598–606, https://doi.org/10.1002/pip.3661.
[14] P.J. Verlinden, Future challenges for photovoltaic manufacturing at the terawatt level, J. Renewable Sustainable Energy 12 (5) (2020), https://doi.org/10.1063/5.0020380.
[15] Y. Zhang, M. Kim, L. Wang, P. Verlinden, B. Hallam, Design considerations for multi-terawatt scale manufacturing of existing and future photovoltaic technologies: challenges and opportunities related to silver, indium and bismuth consumption, Energ. Environ. Sci. 14 (11) (2021) 5587–5610, https://doi.org/10.1039/D1EE01814K.
[16] K.W. Allen, A. Darafsheh, F. Abolmaali, N. Mojaverian, N.I. Limberopoulos, A. Lupu, V.N. Astratov, Microsphere-chain waveguides: Focusing and transport properties, Appl. Phys. Lett. 105 (2) (2014), https://doi.org/10.1063/1.4890595.
[17] T. Mitsui, T. Onodera, Y. Wakayama, T. Hayashi, N. Ikeda, Y. Sugimoto, T. Takamasu, H. Oikawa, Influence of micro-joints formed between spheres in coupled-resonator optical waveguide, Opt. Express 19 (22) (2011) 22258–22267, https://doi.org/10.1364/oe.19.022258.
[18] W. Ahn, X. Zhao, Y. Hong, B.M. Reinhard, Low-Power Light Guiding and Localization in Optoplasmonic Chains Obtained by Directed Self-Assembly, Sci Rep 6 (2016) 22621, https://doi.org/10.1038/srep22621.
[19] M. Gao, M. Kuang, L. Li, M. Liu, L. Wang, Y. Song, Printing 1D Assembly Array of Single Particle Resolution for Magnetosensing, Small 14 (19) (2018) e1800117, https://doi.org/10.1002/smll.201800117.
[20] M. Su, F. Li, S. Chen, Z. Huang, M. Qin, W. Li, X. Zhang, Y. Song, Nanoparticle Based Curve Arrays for Multirecognition Flexible Electronics, Adv. Mater. 28 (7) (2016) 1369–1374, https://doi.org/10.1002/adma.201504759.
[21] S. Zhang, Y. Liu, Y. Qian, W. Li, J. Juvert, P. Tian, J.-C. Navarro, A.W. Clark, E. Gu, M.D. Dawson, J.M. Cooper, S.L. Neale, Manufacturing with light - micro-assembly of opto-electronic microstructures, Opt. Express 25 (23) (2017), https://doi.org/10.1364/oe.25.028838.
[22] S. Zhang, W. Li, M. Elsayed, J. Peng, Y. Chen, Y. Zhang, Y. Zhang, M. Shayegannia, W. Dou, T. Wang, Y. Sun, N.P. Kherani, S.L. Neale, A.R. Wheeler, Integrated Assembly and Photopreservation of Topographical Micropatterns, Small 17 (37) (2021) e2103702, https://doi.org/10.1002/smll.202103702.
[23] Z. Rozynek, M. Han, F. Dutka, P. Garstecki, A. Józefczak, E. Luijten, Formation of printable granular and colloidal chains through capillary effects and dielectrophoresis, Nat. Commun. 8 (2017) 15255, https://doi.org/10.1038/ncomms15255.
[24] Z. Rozynek, Y. Harkavyi, K. Giżyński, Fabrication of 1D particle structures outside a liquid environment using electric and capillary interactions: From fundamentals to applications, Mater. Des. 223 (2022), https://doi.org/10.1016/j.matdes.2022.111233.
[25] Z. Rozynek, A. Magdziarz, Process of fabricating a beaded path on the surface of a substrate, a system for fabricating such a path, use thereof, and a kit. European Patent Office, EP3831171B1, Agnieszka Magdziarz "CADENAS" (2022).
[26] K.S. Tan, K.Y. Cheong, Physical and Electrical Characteristics of Silver-Copper Nanopaste as Alternative Die-Attach, IEEE Trans. Compon. Packag. Manuf. Technol. 4 (1) (2014) 8–15, https://doi.org/10.1109/TCPMT.2013.2285128.
[27] S. Lee, J. Koo, S. Kang, G. Park, Y.J. Lee, Y.-Y. Chen, S.A. Lim, K.M. Lee, J. A. Rogers, Metal microparticle – Polymer composites as printable, bio/ecoresorbable conductive inks, Mater. Today 21 (3) (2018) 207–215, https://doi.org/10.1016/j.mattod.2017.12.005.
[28] S. Feng, S. Cao, Z. Tian, H. Zhu, D. Kong, Maskless Patterning of Biodegradable Conductors by Selective Laser Sintering of Microparticle Inks and Its Application in Flexible Transient Electronics, ACS Appl Mater Interfaces 11 (49) (2019) 45844–45852, https://doi.org/10.1021/acsami.9b14431.
[29] T.B. Holland, U. Anselmi-Tamburini, D.V. Quach, T.B. Tran, A.K. Mukherjee, Effects of local Joule heating during the field assisted sintering of ionic ceramics, J. Eur. Ceram. Soc. 32 (14) (2012) 3667–3674, https://doi.org/10.1016/j.jeurceramsoc.2012.02.033.
[30] N. Haneishi, S. Tsubaki, E. Abe, M.M. Maitani, E. Suzuki, S. Fujii, J. Fukushima, H. Takizawa, Y. Wada, Enhancement of Fixed-bed Flow Reactions under Microwave Irradiation by Local Heating at the Vicinal Contact Points of Catalyst Particles, Sci. Rep. 9 (1) (2019) 222, https://doi.org/10.1038/s41598-018-35988-y.
[31] C. Balemans, N.O. Jaensson, M.A. Hulsen, P.D. Anderson, Temperature-dependent sintering of two viscous particles, Addit. Manuf. 24 (2018) 528–542, https://doi.org/10.1016/j.addma.2018.09.005.
[32] P. Hejmady, L.C.A. van Breemen, P.D. Anderson, R. Cardinaels, Laser sintering of polymer particle pairs studied by in situ visualization, Soft Matter 15 (6) (2019) 1373–1387, https://doi.org/10.1039/C8SM02081G.
[33] J. Nutting, J. Nuttall, The malleability of gold: An explanation of its unique mode of deformation, Gold Bull. 10 (1977) 2–8.
[34] P. Bequin, V. Tournat, Electrical conduction and Joule effect in one-dimensional chains of metallic beads: hysteresis under cycling DC currents and influence of electromagnetic pulses, Granul. Matter 12 (4) (2010) 375–385, https://doi.org/10.1007/s10035-010-0185-8.
[35] H.Y. Bu, Q. Li, S.H. Li, M.N. Li, Comparison of Modified Johnson-Cook Model and Strain-Compensated Arrhenius Constitutive Model for 5CrNiMoV Steel during Compression around Austenitic Temperature, Metals 12 (8) (2022), https://doi.org/10.3390/met12081270.
[36] M. Haustein, A. Gladkyy, R. Schwarze, Discrete element modeling of deformable particles in YADE, SoftwareX 6 (2017) 118–123, https://doi.org/10.1016/j.softx.2017.05.001.
[37] Y. Lin, D.-M. Wang, W.M. Lu, Y.S. Lin, K.-L. Tung, Compression and deformation of soft spherical particles, Chem. Eng. Sci. 63 (1) (2008) 195–203, https://doi.org/10.1016/j.ces.2007.09.028.
[38] L.M. Cox, J.P. Killgore, Z. Li, Z. Zhang, D.C. Hurley, J. Xiao, Y. Ding, Morphing metal-polymer janus particles, Adv Mater 26 (6) (2014) 899–904, https://doi.org/10.1002/adma.201304079.
[39] H.N. Polwaththe-Gallage, C.H. Ooi, J. Jin, E. Sauret, N.T. Nguyen, Z.R. Li, Y.T. Gu, The stress-strain relationship of liquid marbles under compression, Appl. Phys. Lett. 114 (4) (2019), https://doi.org/10.1063/1.5079438.
[40] K. Khobaib, A. Mikkelsen, T. Vincent-Dospital, Z. Rozynek, Electric-field-induced deformation, yielding, and crumpling of jammed particle shells formed on non-

spherical Pickering droplets, Soft Matter 17 (19) (2021) 5006–5017, https://doi.org/10.1039/d1sm00125f.
[41] J.W. Wang, J. Schwenger, A. Strobel, P. Feldner, P. Herre, S. Romeis, W. Peukert, B. Merle, N. Vogel, Mechanics of colloidal supraparticles under compression, Sci. Adv. 7 (42) (2021), https://doi.org/10.1126/sciadv.abj0954.
[42] A.G. Athanassiadis, M.Z. Miskin, P. Kaplan, N. Rodenberg, S.H. Lee, J. Merritt, E. Brown, J. Amend, H. Lipson, H.M. Jaeger, Particle shape effects on the stress response of granular packings, Soft Matter 10 (1) (2014) 48–59, https://doi.org/10.1039/C3SM52047A.
[43] N. Zhang, F. Yang, Y. Shi, F. Guo, Compression creep of 63Sn37Pb solder balls, Acta Mater. 59 (8) (2011) 3156–3163, https://doi.org/10.1016/j.actamat.2011.01.055.
[44] H.C. Lin, C. Kung, R.S. Chen, Evaluations of the BGA solder ball shape by using energy method, CMC-Comput. Mater. Continua 6 (1) (2007) 43–50.
[45] H. Assadi, I. Irkhin, H. Gutzmann, F. Gärtner, M. Schulze, M. Villa Vidaller, T. Klassen, Determination of plastic constitutive properties of microparticles through single particle compression, Advanced Powder Technology 26(6) (2015) 1544-1554, 10.1016/j.apt.2015.08.013.
[46] E. Falcon, B. Castaing, M. Creyssels, Nonlinear electrical conductivity in a 1D granular medium, Eur. Phys. J. B - Condensed Matter Complex Syst. 38 (3) (2004) 475–483, https://doi.org/10.1140/epjb/e2004-00142-9.
[47] C. Zhang, S. Maramizonouz, D. Milledge, S. Nadimi, An electro-mechanical contact model for particulate systems, Powder Technol. 440 (2024) 119759, https://doi.org/10.1016/j.powtec.2024.119759.
[48] E. Falcon, B. Castaing, Electrical conductivity in granular media and Branly's coherer: A simple experiment, Am. J. Phys 73 (4) (2005) 302–307, https://doi.org/10.1119/1.1848114.
[49] K. Bourbatache, M. Guessasma, E. Bellenger, V. Bourny, A. Tekaya, Discrete modelling of electrical transfer in multi-contact systems, Granul. Matter 14 (1) (2012) 1–10, https://doi.org/10.1007/s10035-011-0307-y.
[50] S. Dorbolo, A. Merlen, M. Creyssels, N. Vandewalle, B. Castaing, E. Falcon, Effects of electromagnetic waves on the electrical properties of contacts between grains, Europhys. Lett. 79 (5) (2007) 54001, https://doi.org/10.1209/0295-5075/79/54001.
[51] C. Zhai, Y. Gan, D. Hanaor, G. Proust, Stress-dependent electrical transport and its universal scaling in granular materials, Extreme Mech. Lett. 22 (2018) 83–88, https://doi.org/10.1016/j.eml.2018.05.005.
[52] Silver paste, Loctite ECI 1010, [Accessed: 17.10.2024]. https://dm.henkel-dam.com/is/content/henkel/lt-8159-Product_information_sheet-loctite-eci-1010-1011.
[53] Gold paste, XTPL S.A., [Accessed: 17.11.2024]. https://xtpl.com/product/wp-content/uploads/2024/03/XTPL-Au-Nanopaste-90-TDS.pdf.
[54] https://doc.comsol.com/ - search for "Theory for Electrical Contact" [Accessed on 8 Nov 2023].
[55] Y. Harkavyi, K. Giżyński, Z. Rozynek, Experimental and FEM simulation study of compressive deformation of solder microballs and particle chains, Soft Matter (2025), https://doi.org/10.1039/d4sm01499e.
[56] M.M. Nagl, W.T. Evans, The mechanical failure of oxide scales under tensile or compressive load, J. Mater. Sci. 28 (23) (1993) 6247–6260, https://doi.org/10.1007/BF01352181.

Supporting Information

Fabrication of a new type of electrically conductive micro-tracks formed *via* mechanical compression of beaded structures

Z. Rozynek,[1,2*†] Y. Harkavyi,[2†] Ø. G. Martinsen[3,4] and K. Giżyński[5]

[1]*CADENAS P.S.A., Prof. Sylwestra Kaliskiego 24, 85-796 Bydgoszcz, Poland*

[2]*Faculty of Physics and Astronomy, Adam Mickiewicz University, Uniwersytetu Poznańskiego 2, 61-614 Poznań, Poland*

[3]*Department of Physics, University of Oslo, Sem Sælands vei 24, 0316, Oslo, Norway*

[4]*Department of Clinical and Biomedical Engineering, Oslo University Hospital, Sognsvannsveien 20, 0372 Oslo, Norway*

[5]*Institute of Physical Chemistry, Polish Academy of Sciences, Kasprzaka 44/52, 01-224 Warsaw, Poland*

[†]These authors contributed equally to this work. [*]Corresponding author: zbiroz@amu.edu.pl

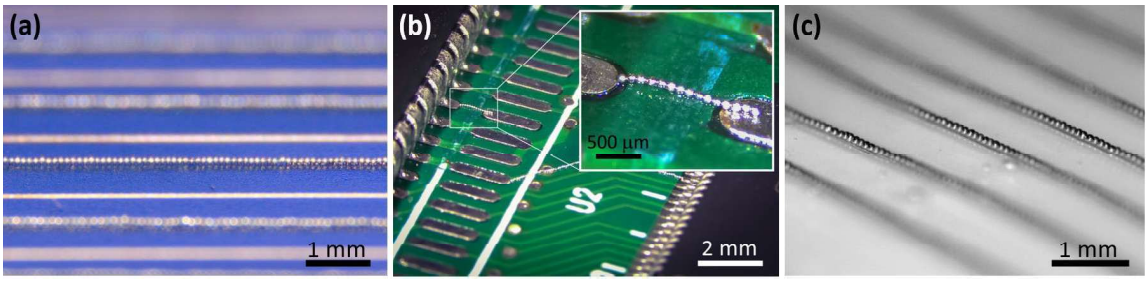

Figure S1. Examples of microparticle patterns created using the method described in ref. [1]. (**a**) Parallel lines of 100-µm aluminum particles formed on a photovoltaic cell. The particle tracks are alternated with conventional "fingers" made of sintered silver nanoparticles deposited on the substrate via screen printing. (**b**) A short path of 100-µm Pb37Sn63 solder balls formed on the surface of the PCB to repair the broken electrical connection. (**c**) Parallel lines of 100-µm unleaded SAC305 solder particles formed on a plexiglass substrate coated with a thin layer of UV-curable resin.

Figure S2. An MFIA impedance spectrometer from Zurich Instruments was used to measure the particle chain resistance. The particle chain was placed on a 2T DUT (device-under-test) carrier with two copper pads, approximately 10 µm thick, and a gap of around 16 mm between them. The carrier was connected to an MFITF Impedance Test Fixture, ensuring high precision in impedance measurements, particularly for low values near the instrument's sensitivity limit (~0.1 mΩ). This experimental setup allowed real-time monitoring of electrical impedance during the compression process of the particle chain. The PCB carrier was selected to minimize parasitic effects and damping by eliminating the need for lead wires, facilitating the study of the electronic properties of particle chains. The equipment was calibrated using an open-circuit test (measurement of a device with infinite impedance) and a short-circuit test (measurement of a device with zero impedance). This setup achieves the measurement accuracy comparable to the four-wire method, as the influence of lead wires is practically eliminated, and the contact resistance is significantly smaller than the resistance of the particle chain (see also **Figure S5**).

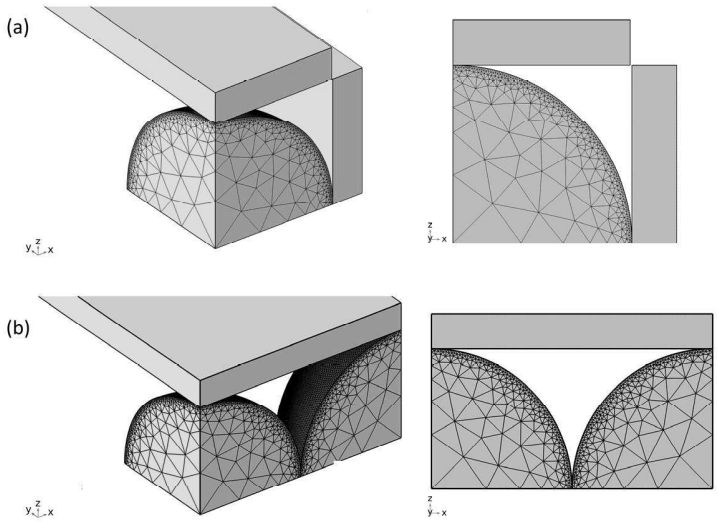

Figure S3. 3D Meshed Geometry of the Simulated Systems Configurations: The image showcases the meshed model used to study compression and electric behavior. (**a**) The final meshed geometry of the model was used for precise particle deformation, representing the simulated system configuration with a 760 µm $Sn_{63}Pb_{37}$ solder particle and two rigid plates (compressive and as a substitute for a neighboring particle). (**b**) Extended mesh geometry of the model used in the Electric Currents interface. The coarsened mesh, used in the current flow model, consists of two contacting 760 µm $Sn_{63}Pb_{37}$ solder particles and a pressing plate, allowing for simulating electrical resistance as a function of compression level.

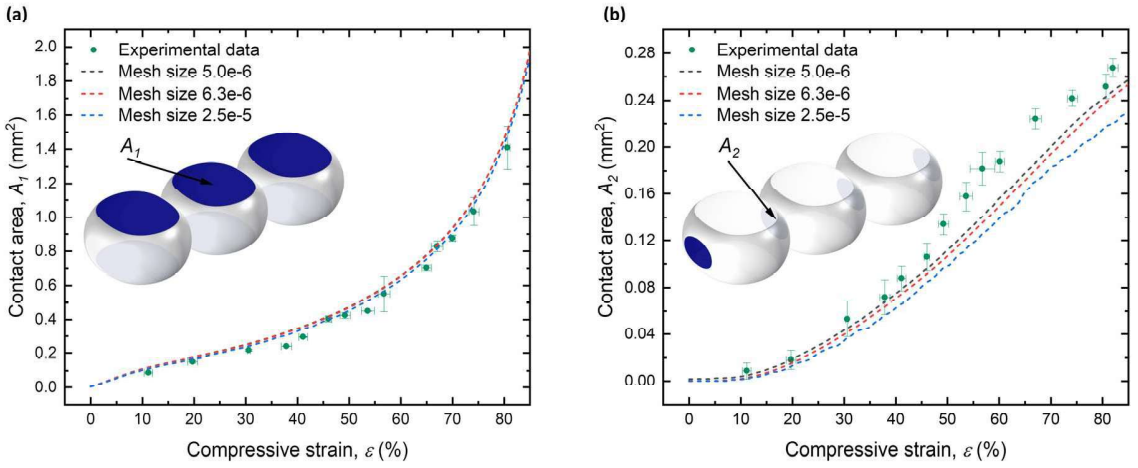

Figure S4. Comparison of measured experimental values and simulated values for contact areas (A_1 and A_2) during compression of 760-µm solder balls. (**a**) Shows the measured experimental values of A_1 (contact area between compression plate and selected ball) along with simulated values using perfectly plastic material model with a different mesh size. (**b**) Depicts the measured experimental values of A_2 (contact area between compressed balls) along with simulated values using the perfectly plastic material model with a different mesh size.

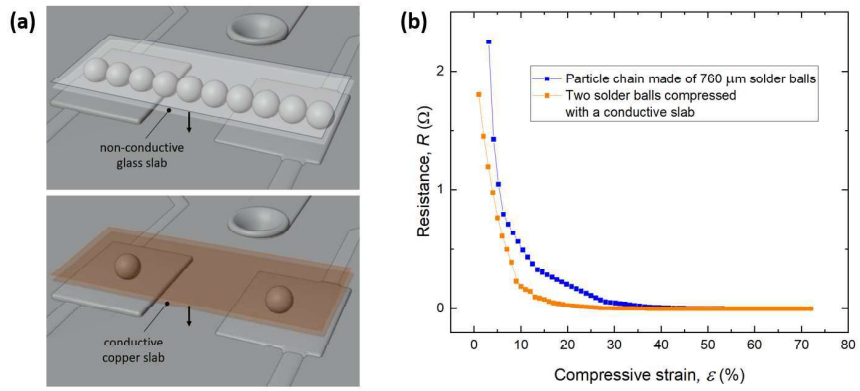

Figure S5. (**a**) The schematic diagrams depict the measurements conducted to validate the significance of ball-pad contact resistance on the overall measured resistance of the chain. The top panel illustrates the measurement of the resistance of the particle chain when compressed with a non-conductive glass slab. In the bottom panel, an experiment is schematically shown where two solder balls are positioned on the Cu pads and pressed from above using an electrically conductive Cu slab. (**b**) The resistance values of a compressed chain consisting of 760-μm solder balls (blue) and the resistance values of two individual balls positioned on Cu pads and compressed by a conductive Al slab (orange). The resistance values are plotted as a function of ε. It is important to note that the data points shown in the figure represent an average of three measurements.

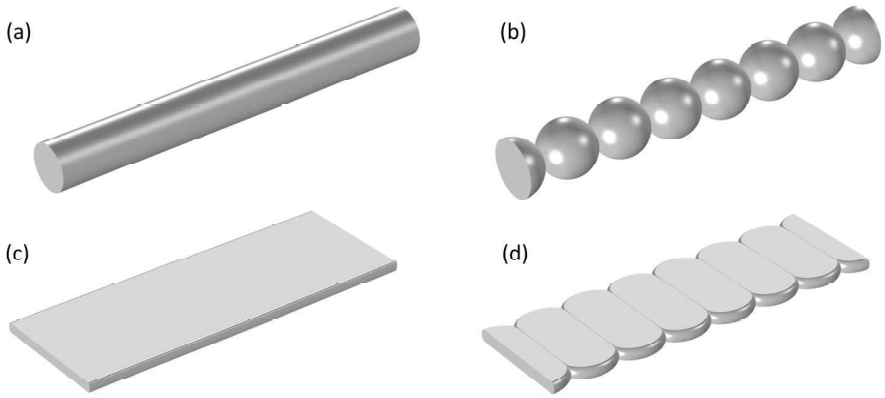

Figure S6. (**a**) A cylinder with the same volume as a chain (**b**) of seven solder balls. (**c-d**) Both structures are compressed from above with ε = 75%. The compressed structures exhibit nearly identical geometry and resistances: $R_{cylinder}$ = 0.01004 Ω and R_{chain} = 0.01054 Ω. These values were simulated using COMSOL, assuming the initial radii of the cylinder and balls to be 81.7 μm and 100 μm, respectively.

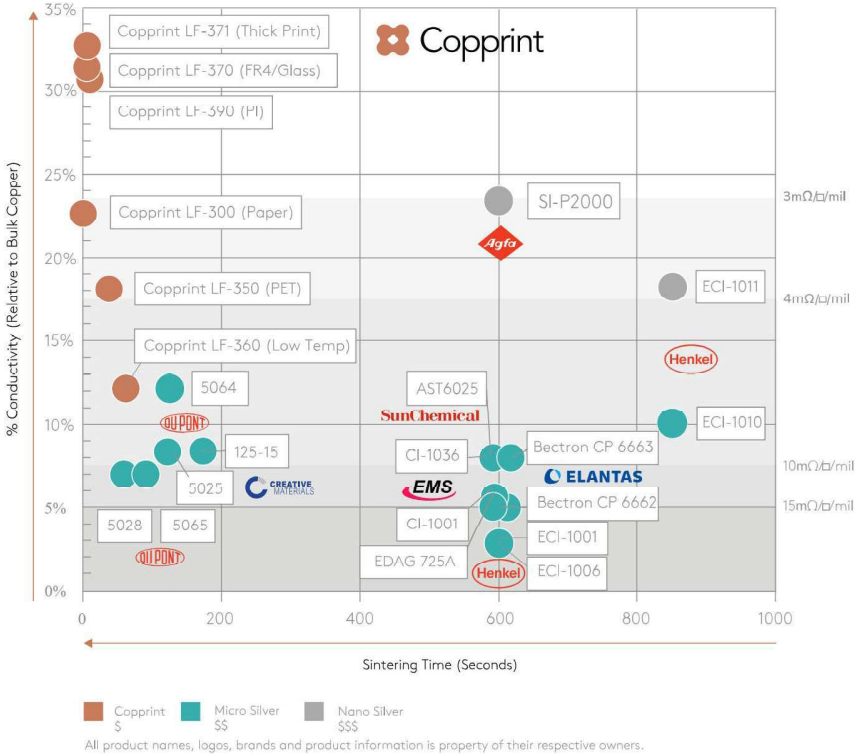

Figure S7. Comparison of the performance of conductive pastes based on various nano- and sub-micro materials, including copper and silver. Illustration adapted from promotional materials by Copprint, available at https://www.copprint.com.

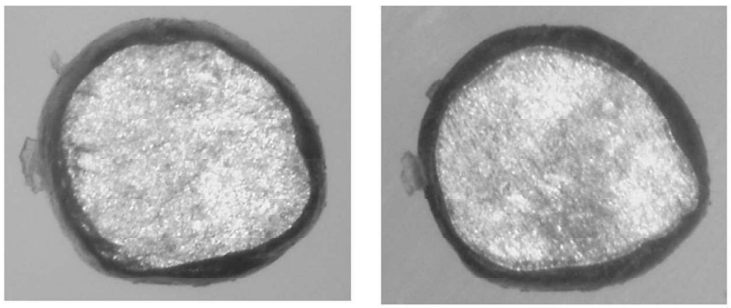

Figure S8. Micrographs of a compressed particle, showing the side deformed upon contact with the glass surface (**left**) and the side deformed upon contact with the copper surface (**right**). To facilitate direct comparison, the right image has been mirrored along the vertical axis.

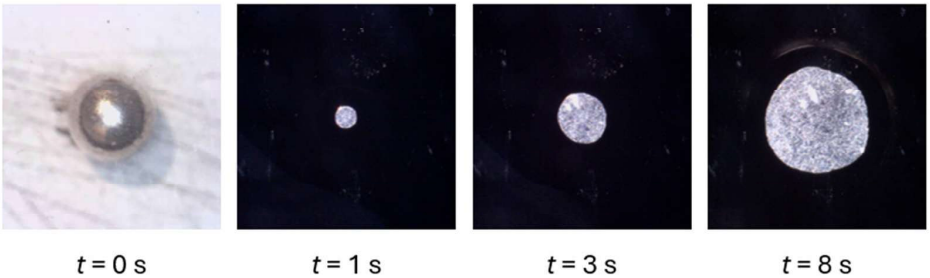

Figure S9. Sequential images showing the compression of a $Sn_{63}Pb_{37}$ solder ball (760 µm) by a glass slab. The first image ($t = 0$ s) presents the solder ball before being immersed in black ink. The subsequent images depict the compression process, observed through the glass in the direction of flattening. As the compression progresses, a new interface (A_1) forms between the glass and the ball. The images demonstrate that the ink is expelled outward rather than remaining trapped between the flattening ball and the glass surface.

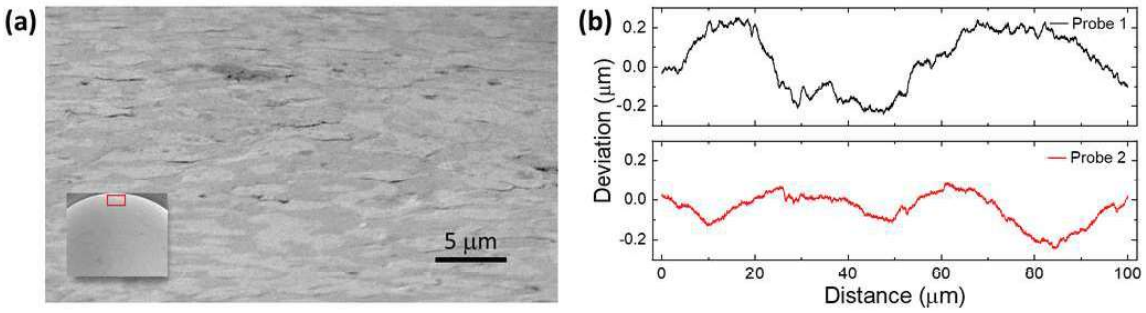

Figure S10. (**a**) SEM image of a 760-µm solder microball captured from a specific perspective. The inset presents a wider view of the microball, with a highlighted area indicating the section that is magnified in the main SEM image. (**b**) Profilometry results from the experiment conducted with a 2.5 µm diameter stylus under a force of 3 mg.

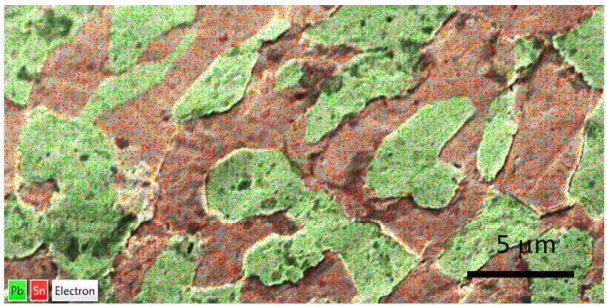

Figure S11. Investigation of the particle's surface by EDS. The red and green areas indicate detected Sn and Pb domains in the binary eutectic alloy of $Sn_{63}Pb_{37}$ solder ball. Visible gray spots within the eutectic colony may be oil residues from the microball production process, suggesting the balls are not perfectly clean.

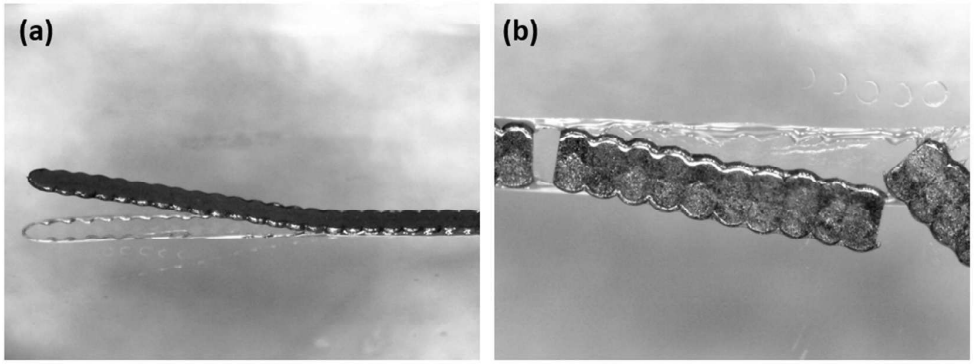

Figure S12. In the context of practical applications and future research, it is interesting to determine the adhesion strength of the micropath to the substrate and the connection strengths between particles, as a function of compressive strain and compression rate. Compressed microparticles of solder with an initial diameter of 400 µm. (**a**) Part of the path has been mechanically lifted (levered with a needle). The path possesses certain elastic properties, and the crushed particles of the chain adhere to each other. (**b**) The path has been broken by mechanically bending it across the path. The breaks occurred along the connections between the balls, indicating that the particles were not fused (no diffusion bonding occurred).

Movie S1. Demonstration of the method for creating a linear beaded structure on a substrate surface according to patents [EP3831171B1, US11856709B2]. In this video, solder microbeads (100 µm) suspended in liquid flux are deposited onto a glass plate surface. An electric voltage of 1 kV is applied to a blunt needle, guiding the arrangement of the beads into a linear structure on the substrate

Movie S2. 3D visualization of the experimental set-up used for resistance measurements of a particle chain under mechanical compression. The set-up includes an impedance analyser impedance analyser (Zurich Instruments) equipped with the impedance test fixture (MFITF), a digital microscope positioned above the particle chain to observe it from the top along the compression direction, translational stages for moving the compression slab; and a device-under-test (DUT) carrier specifically designed for measuring surface-mounted electronic components. The PCB carrier features a line of nearly monodispersed particles deposited on its surface between two copper pads. A thick glass, secured by clamps mounted on the translational stages, serves as the compression slab. Its position can be precisely controlled with sub-micrometre accuracy.

Movie S3. The results of the COMSOL simulations on the compressive deformation of a particle chain. The left panel shows the evolution of particle shapes observed from above (in the direction of compression). Plots illustrate the changes in the contact area values between the compressing wall and the particle chain (A_1), as well as the changes in the elongation of the balls (L), with the top and bottom plots respectively. The simulated balls in the chain initially have a diameter of 760 µm.

Movie S4. The results of COMSOL simulations on the compressive deformation of a particle chain are presented. The left panel displays the evolution of particle shapes and changes in their contact area (highlighted in blue). The accompanying plot illustrates quantitative changes in the contact area between two adjacent microparticles. The simulated balls in the chain initially have a diameter of 760 µm.

Movie S5. Video showcases the results of COMSOL simulations focusing on the compressive deformation of a particle chain. The left panel illustrates the evolution of particle shapes as viewed along the particle chain and the changes in their aspect ratio. The aspect ratio is defined as the ratio between the height (h) and the width (w) of the particle, measured across the structure at the center of the particle. The accompanying plot provides a quantitative analysis of changes in the h:w ratio. The simulated balls in the chain initially have a diameter of 760 µm.

Movie S6. A particle chain consisting of seven 300-µm $Sn_{63}Pb_{37}$ spheres, deposited on the device-under-test (DUT) carrier. The orange areas are two copper electrode pads. The film is recorded from above the compression glass slide, in the direction of compression. On the lower panel, an animation obtained from COMSOL simulations is presented.

Movie S7. Comparison of the compression behavior of individual solder balls: $Sn_{63}Pb_{37}$ and SAC305. The SAC305 solder exhibits a more irregular deformation pattern, with a less spherical contact surface (A_1) between the compressed ball and the glass plate, while the $Sn_{63}Pb_{37}$ solder deforms more uniformly, maintaining a smoother and more symmetric contact area.

Movie S8. Real-time recording of the flattening process of a $Sn_{63}Pb_{37}$ solder ball (760 µm) compressed by a glass slab. The observation is conducted through the glass in the direction of compression. The solder ball is initially immersed in black ink. As the glass slab contacts the ball, a new interface (A_1) forms between them. The experiment demonstrates that the ink is expelled outward rather than being trapped between the glass and the deformed solder ball.

Movie S9. The video presents two COMSOL-based compression simulations of sphere pairs between parallel plates. The visualization shows only the 760 µm spheres, with the other spheres removed to highlight the contact area. On the left, a 450/760 µm pair exhibits localized plastic indentation on the larger sphere due to contact with the smaller one. On the right, a 760/760 µm pair undergoes symmetric compression, resulting in uniform plastic flattening. In the non-symmetric case, the larger sphere wraps around the smaller one, increasing the contact area at small strains (≤15%) compared to the symmetric case.

[1] Z. Rozynek, A. Magdziarz, Process of fabricating a beaded path on the surface of a substrate, a system for fabricating such a path, use thereof, and a kit, in: E.P. Office (Ed.) Agnieszka Magdziarz "CADENAS", 2022.

——Scientific Paper V——

Formation of conductive beaded structures via Joule heating

Harkavyi Y., Solovan M. and Rozynek Z.,

(To be submitted, Fall 2025)

Formation of conductive beaded structures via Joule heating

Y. Harkavyi[1†*], M. Solovan[2], and Z. Rozynek[1†]

[1] *CADENAS P.S.A., Prof. Sylwestra Kaliskiego 24, 85-796 Bydgoszcz, Poland*
[2] *Faculty of Physics and Astronomy, Adam Mickiewicz University, Uniwersytetu Poznańskiego 2, 61-614 Poznań, Poland*

[†]These authors contributed equally to this work. [*]Corresponding author: zbiroz@amu.edu.pl

ABSTRACT: The demand for cost-effective and sustainable methods of fabricating conductive microtracks is steadily increasing, particularly in applications such as printed and flexible electronics, photovoltaics, and micro-interconnects. While nanoparticle-based inks and pastes are widely employed, they are costly, environmentally demanding, and typically yield porous structures with resistivities significantly higher than the bulk material. In contrast, metallic microparticles offer lower material cost, improved sustainability, and the potential to form highly conductive structures when appropriately fused. In this work, we investigate the use of Joule heating for controlled joining of solder microparticles under low-cost laboratory power supplies. The study combines experimental measurements with numerical simulations to the transient thermal and electrical response at particle junctions. Single pairs of solder spheres were rigidly mounted on microdrill electrodes and subjected to applied voltages in the range of 2.5–30 V. Neck formation occurred rapidly after particle contact, with its growth strongly influenced by the applied voltage and transient current overshoots that initiated localized melting. Complementary finite-element simulations captured the interplay between current flow, thermal gradients, and liquid–solid phase transitions, and revealed that the initial size of the electrical contact strongly determines both the maximum temperature achieved and the cooling dynamics of the junction. Overall, this study provides the first demonstration of controlled Joule heating of solder microparticles using an inexpensive DC power supply, supported by direct correlation between experiment and numerical modeling. The results establish a framework for precise design of single-particle-thick conductive tracks, where both geometry and electrical resistance can be tuned through the excitation parameters. The approach offers a promising low-cost, scalable alternative to nanoparticle-based microtracks, and opens pathways for applications ranging from printed and flexible electronics to photovoltaics, bioelectronics, and ordered microsphere-based metamaterials.

KEYWORDS*: 1D structures, beaded structure, microparticles, solder, assembly, Joule heating, fusing, neck formation, electric tension, conductive paths*

1. Introduction

Fabrication approaches for conductive microtracks: Conductive tracks with micrometer-scale widths, fabricated on substrates as functional elements in electronic devices, can be produced using a wide variety of methods ranging from industrially established processes to niche or emerging approaches. These methods can be broadly classified according to the type of building blocks from which the conductive structures are formed. In *top-down methods*, such as photolithography combined with chemical etching, laser ablation, or mechanical milling, tracks are defined by selectively removing material from a continuous metallic layer. In contrast, *bottom-up methods* create conductive paths by assembling matter directly onto the substrate. Within this group, two distinct categories can be distinguished. The first involves *atomic or ionic growth*, where deposition occurs through chemical or electrochemical routes, such as

electroplating [1]. The second relies on *particle-based assembly*, in which nanoparticles or microparticles serve as discrete building blocks, deposited and subsequently sintered or fused to form continuous conductive tracks. This category includes technologies based on nanoparticle pastes and nanoinks, such as screen printing [2], aerosol jet printing [3], inkjet printing, slot-die coating, and flexography [4], as well as various field-assisted methodologies in which microspheres are assembled into conductive chains [5-10].

Comparative assessment of particle-based methods: An interesting perspective in this context is to compare different fabrication approaches in terms of their energy cost, financial cost, and the resulting quality of the structures. As an illustrative example, we consider here several representative bottom-up methods. In **Table 1** we summarize the techniques and materials employed to fabricate a model linear conductive track with a cross-section of about 100 × 100 µm, that is a geometry relevant to many microelectronics applications, positioned in the intermediate size range between few-micrometer-wide lines and sub-millimeter structures. If such tracks were to be produced from, for instance, nanoparticle-based pastes (*e.g.*, silver, copper, or hybrid inks) or microparticle-based dispersions, distinct processing routes would be required. Moreover, the preparation and processing of the starting materials differ substantially between these cases, reflecting both the complexity and sustainability of each approach.

Category	Material form	Example method	Material cost (€/g)	Environmental cost	Ease of 1:1 aspect ratio tracks	Relative conductivity (% of bulk)
Nanoparticles (aerosols)	Ag or Cu (20–100 nm)	Aerosol jet printing	10–50	very high	Difficult (poor vertical build-up)	10–50% (after sintering)
Nanoparticles (pastes/inks)	Ag NP paste (50–500 nm)	Inkjet or screen printing	1–5	very high	Moderate (poor vertical control)	10–50% (after sintering)
Microparticles (agglomerated)	Ag MPs (1–10 µm)	Stencil printing	0.5–1	moderate	Easier than NPs (enables thicker layers)	20–70% (after sintering)
Microparticles (single-particle thick)	Solder MPs (100 µm)	CADENAS assembly	0.05–0.1	Low	Good (near 1:1 ratios)	~100% (metallic bridges)

Table 1. Comparative overview of representative particle-based approaches for fabricating medium-sized model conductive tracks. The table summarizes characteristic material forms, example methods, relative costs, environmental impact, and achievable electrical performance. Microparticle-based chains assembled from single-particle-thick layers stand out for their low material cost, low environmental footprint, and near-bulk conductivity without the need for high-temperature sintering.

A comparison of different particle-based assembly routes (**Table 1**) highlights significant differences in material cost, environmental footprint, processability, and final electrical performance. Nanoparticle-based methods, such as aerosol jet or inkjet printing, enable fine-resolution features but rely on precursors that are extremely expensive (up to tens of thousands of euros per kilogram) and energy-intensive to produce, resulting in high environmental costs. Moreover, achieving high aspect ratio tracks is difficult due to particle redistribution and limited vertical build-up [1], and even after sintering the conductivity typically reaches only a fraction of the bulk metal (see **Figure S1**). Methods that use microparticle-based pastes or inks [11] are less costly and more sustainable, and they facilitate the fabrication of thicker tracks, but still require

post-processing at elevated temperatures to achieve satisfactory conductivity. In striking contrast, chains assembled from simple microparticle dispersions exhibit near-bulk conductivity without the need for extensive oven sintering, while also supporting the formation of mechanically robust bridges. Particularly interesting in this context are conductive tracks composed of single-particle-thick microparticle layers, whose width can be readily tuned by selecting the particle size used to assemble the chains.

Single-particle thick structures of conductive microparticles: Chains of microparticles arranged side by side on a substrate exhibit only limited electrical contact between neighboring spheres [8, 12, 13], and therefore their conductivity is far below that of a solid conductor of the same material and comparable linear mass density, such as a cylindrical wire. To improve conductivity, the contact area between adjacent particles must be enlarged, which can be achieved through various post-processing strategies. These include mechanical methods, where compressive stress is applied to plastically deform malleable metals [14], as well as thermal methods, such as infrared laser treatment [15-17], microwave sintering [18] and Joule heating [19, 20], which promote partial melting, neck growth, and coalescence of particles, thereby increasing interparticle contact and reducing resistance.

Joule heating, in particular, relies on resistive dissipation of electrical energy within the chain, producing localized heating at the junctions between neighboring spheres. At these narrow contacts, current crowding leads to enhanced resistive losses, which makes them the primary sites of temperature rise and subsequent neck growth.

As mentioned above, chains of metallic microparticles, where neighboring spheres touch only over extremely small areas, exhibit resistances several orders of magnitude higher than a solid wire of the same linear mass density [8, 12]. Two important aspects should be emphasized here: (i) Although, in theory, the contact area between two ideal rigid spheres could be treated as zero (a point contact), according to classical Hertzian contact theory, any real contact between bodies under a finite normal load results in a small but finite circular contact area. In practice, particles arranged manually or through field-assisted assembly touch each other with a nonzero normal force even without external pressure, owing to weak adhesive interactions such as van der Waals forces, capillary bridges (if a thin moisture film is present on the particle surfaces), and local micro-deformation induced by slight lateral friction during positioning, which can generate a small effective normal load [21]. Although much weaker than mechanical compression, these interactions are sufficient to create a real physical contact and a finite electrical constriction between adjacent spheres. (ii) However, when particles are only loosely touching, *i.e.* held together primarily by adhesion or weak surface forces rather than by external compression, the electrical contact area is typically much smaller than the mechanical contact area. This is because true conduction occurs only through a few microscopic asperity junctions or by tunneling across nanoscale gaps, leading to an overall resistance significantly higher than would be expected from a simple mechanical contact model [22].

As a result, electrical transport in such particle chains is dominated by constriction resistance at narrow junctions, where current is initially forced to pass through a limited number of microscopic pathways. When the current becomes sufficiently high, the locally dissipated heat can raise the temperature to the point of partial or complete melting of the material. Driven by surface tension, this molten material tends to flow and merge, leading to neck formation and, under excessive heating, even to coalescence of neighboring spheres. However, for the purpose of forming continuous conductive microtracks, complete coalescence is undesirable, as it would produce isolated, irregularly spaced metallic islands along the original beaded path rather than a uniform continuous conductor. Consequently, for example, thermal treatment in a furnace, which heats the entire structure uniformly and uncontrollably, may lead to such disconnection, as demonstrated in **Figure S2**.

In contrast, our hypothesis was that controlled Joule heating, regulated by the current amplitude, pulse duration, waveform, and total power, enables localized neck growth between adjacent particles without inducing full melting. This process effectively reduces resistance toward its theoretical minimum, while simultaneously strengthening and stabilizing the structure mechanically, yet avoiding complete coalescence, which would otherwise lead to fragmentation and loss of electrical continuity.

Joule heating (also known as resistive or Ohmic heating) is a process in which the passage of an electric current through a conductor generates heat, and it has long been employed as a method for joining materials. In the context of microscale joining, Joule heating enables the fusion of metallic microparticles, including solder spheres and other conductive materials, by exploiting localized heating at their junctions. When current flows through two contacting particles, the constricted interface exhibits elevated resistance, leading to current crowding and a rapid temperature rise. This localized heating can cause surface softening, melting, or partial coalescence, thereby establishing a metallurgical bond between the particles. Unlike global heating methods, Joule heating is inherently selective: the regions of highest resistance are preferentially heated, allowing energy to be focused at the junction without excessive heating of the surrounding material.

The electric current can either be induced by electromagnetic excitation from a spark discharge [23] or supplied by a conventional AC/DC power source [22, 24]. Despite extensive research in this field, no studies have demonstrated controlled Joule heating of solder microparticles using a low-cost power supply, combined with a direct correlation between experimental results and numerical simulations. Furthermore, previous work has not addressed the link between mechanical bonding and electrical connectivity, nor provided quantitative resistance estimates for particle pairs with diameters below one millimeter. This study fills this gap and additionally explores the joining of microparticle chains. By integrating experiments with modeling, we demonstrate the feasibility of developing simple yet effective electronic control systems for practical applications in printed and flexible electronics.

2. Methods

2.1. Materials, sample preparation and experimental setup

In this study, we used leaded solder ball microparticles ($Sn_{63}Pb_{37}$) sourced from PMTC, Taiwan, and supplied via Reball, Poland. The particles had a diameter of 760 µm with a tolerance of ±15 µm. These particles exhibit a melting point of 183°C. Their mechanical properties were thoroughly characterized in our previous publication [14].

Relatively large microparticles were deliberately chosen for two reasons. First, their size facilitates direct observation of contact formation between particles using a standard optical microscope. Second, particles of this size (or larger) can be mechanically fixed to electrical leads with only minor effort. For this purpose, microdrills (purchased from Yevhen Lyfar Micro via the Minitool-PL shop on Allegro.pl) were employed. The solder balls were pierced with the tip of the drill bit, while the shank of the microdrill was secured using crocodile clips with strong springs to ensure stable electrical contact. This simple configuration provided both reliable electrical connectivity and straightforward handling during the experiments.

In **Figure 1**, the procedure used to pierce the solder balls with microdrills is shown. In the first step (**Figure 1b**), the rotating drill bit was gradually inserted into the surface of the solder ball until a defined penetration depth L was reached, corresponding to approximately half of the ball diameter (**Figure 1c**). This ensured both mechanical stability and reliable electrical contact between the particle and the drill. For controlled drilling, we used the XYZ motorized platform of a Snapmaker 2.0 equipped with a CNC toolhead. Optical monitoring of the process was performed with digital microscopes (AM7115, Dino-Lite), which provided real-time front and side views of the preparation. The solder ball, firmly attached to the drill bit, could then be lifted from the supporting needle that held it in place during drilling (**Figure 1d**). Afterwards, the drill with the mounted solder ball was fixed in mechanical holders forming part of the experimental setup for particle sintering studies (**Figure 1e**). This approach enabled straightforward and reproducible sample preparation.

For the sintering experiments of particle pairs, the setup included a high-speed camera (Chronos 2.1-HD, Kron Technologies Inc., Canada), strong back illumination, and a voltage supply with current and voltage limiting (KA3005P KORAD). Two crocodile clips were used to secure the drills with solder balls (**Figures 1e–f**). The first holder was attached to an XYZ translation stage, allowing precise positioning of one solder ball relative to the other. The second holder was mounted on one end of a pivoted arm, with the opposite end fixed to a hinge. This arrangement allowed the arm to deflect freely when the translation stage brought the two particles into contact (**Figure 1g**). Consequently, the applied mechanical force at the particle–particle junction depended on the deflection angle of the arm: the larger the deviation from the vertical, the greater the horizontal force component acting at the contact between the two solder balls.

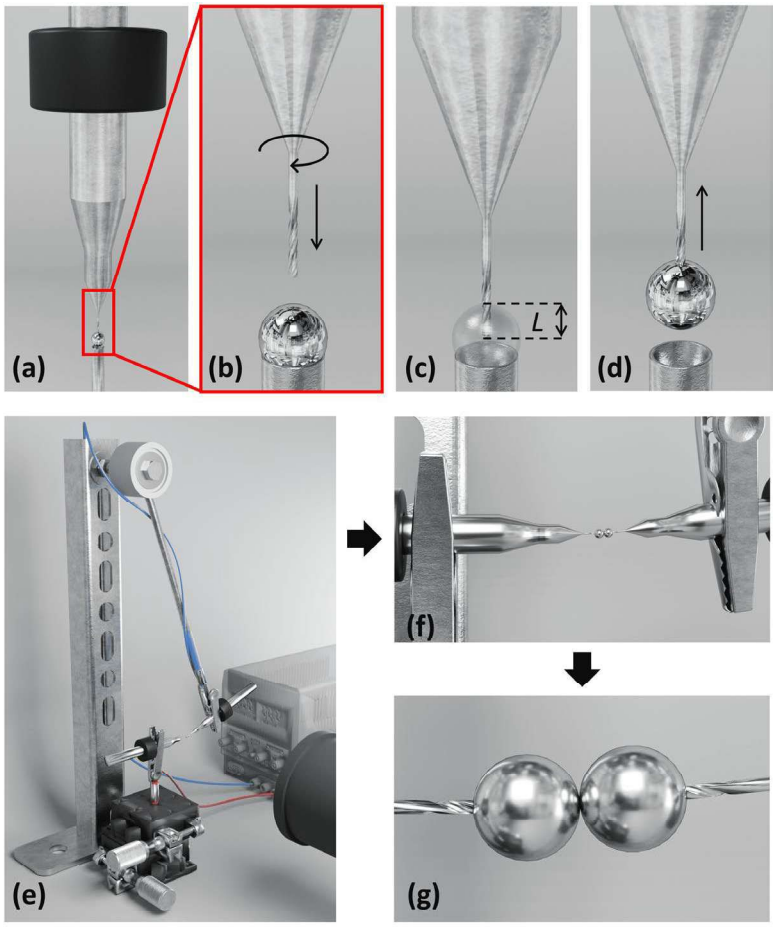

Figure 1. 3D renders presenting schematic illustrations of (**a–d**) the procedure used to mechanically fix solder balls with microdrills and (**e–g**) the experimental setup for sintering studies. (**a**) General view showing the microdrill with its thicker shaft and a solder ball placed on a capillary tube with an inner diameter (700 µm) slightly smaller than the ball diameter (760 µm). The mechanical stress in the direction of the drill motion (which is along the direction of gravity) causes a slight local deformation of the microball at the point of contact with the capillary but does not affect the hemisphere of the ball whose surface center will subsequently be brought into contact with a second ball. (**b**) Close-up showing the insertion process, where the rotating drill bit tip is driven into the solder ball. (**c**) The drill penetrates to a controlled depth (L), ensuring both mechanical stability and electrical contact. (**d**) Finally, the solder ball is firmly attached to the drill shank, enabling its manipulation and connection to the measurement circuit. (**e**) Overview showing solder balls mounted on microdrills clamped in holders and connected to a voltage source, with a high-speed camera used to record shape changes during sintering. (**f**) Close-up of opposing drills with mounted solder balls before contact. (**g**) Two solder balls aligned and brought into contact for sintering experiments.

2.2. Computer simulations

All simulations were performed using COMSOL Multiphysics 6.2. To reduce computational cost while maintaining accuracy, the geometry was simplified by exploiting its radial symmetry and modelled in 2D axisymmetric configuration. The structure consisted of two quarter-spheres, each with a radius of 380 µm, joined at a defined contact region. This initial contact zone was critical to the simulation outcomes and was controlled by the parameter $h/2$, defined as the distance between the symmetry axis and the endpoint of the rounded joint (*i.e.*, half of the neck height). This parameter was subsequently varied to investigate its influence on the thermal distribution and electrical current flow within the structure. The contact between spheres was modelled with a rounded transition whose diameter matched the gap between the opposing surfaces, ensuring smooth geometry and minimizing mesh irregularities. The final geometry used

in simulations is shown in **Figure 2**. The mesh was set to "Extremely Fine" globally, with particular attention paid to the contact region. An edge distribution was imposed on the rounded area, using fixed elements to accurately resolve steep thermal and electrical gradients.

This geometry was the basis for two complementary simulation models: a rigid model without shape changes, serving as a reference for electrical and thermal effects, and a deformable model incorporating material flow and shape evolution during heating. All material properties used in both models were taken from published data and are listed in **Table 2**.

	Property	Value	Unit
Solid phase	Heat capacity at constant pressure	150	$\mathrm{J/kg \cdot K}$
	Density	9000	$\mathrm{kg/m^3}$
	Thermal conductivity	50	$\mathrm{W/m \cdot K}$
	Specific dynamic viscosity	400	$\mathrm{Pa \cdot s}$
Liquid phase	Heat capacity at constant pressure	165	$\mathrm{J/kg \cdot K}$
	Density	8400	$\mathrm{kg/m^3}$
	Thermal conductivity	60	$\mathrm{W/m \cdot K}$
	Specific dynamic viscosity	0.0004	$\mathrm{Pa \cdot s}$
Latent heat from solid to liquid phase		$47 \cdot 10^3$	$\mathrm{J/kg}$
Transition interval between solid to liquid phase		10	K
Phase change temperature between solid and liquid phase		456	K
Electrical conductivity		$6.67 \cdot 10^6$	$\mathrm{S/m}$

Table 2. Material properties of $Sn_{63}Pb_{37}$ used in the rigid and deformable simulation models. The rigid model accounts for electrical and thermal effects without shape evolution, while the deformable model incorporates material flow and geometry changes during heating.

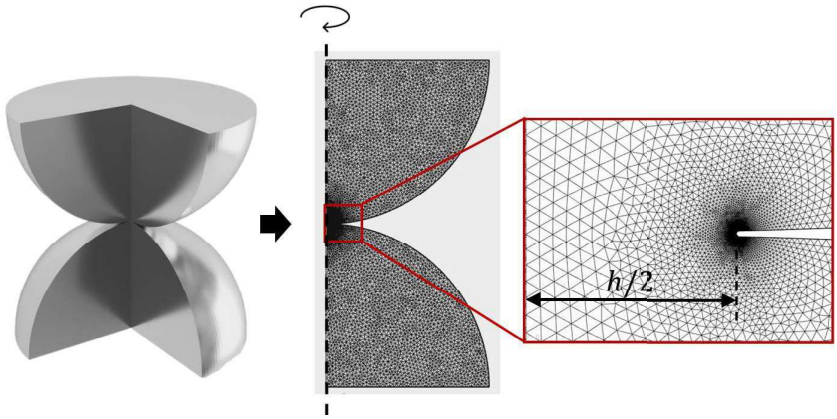

Figure 2. Geometry and meshing procedure used in the simulations. (Left) The simplified quarter-sphere model representing two solder particles in contact. (Middle) Axisymmetric 2D cross-section of the geometry, with mesh refinement applied near the neck region. (Right) Magnified view of the triangular mesh around the particle joint, with $h/2$ defined as the distance between the symmetry axis and the endpoint of the rounded neck.

2.3.1 Simulations without shape changes

In the first model, the geometry was kept rigid and non-deformable. The *Electromagnetic Heating* interface, coupling *Electric Currents* with *Heat Transfer in Solids*, was employed. A current I was applied to one flat surface of the quarter-sphere cross-section, while the opposite surface (mirror-reflected across the interparticle contact) was grounded. Heat exchange with the

surrounding air was modelled using a convective heat flux boundary condition on all external surfaces, assuming zero air velocity to represent natural convection.

Two types of studies were performed. In the first case, the electrical resistance was calculated as a function of the neck height *h*, varied between 1 and 200 µm, using a stationary setup. In the second case, a time-dependent study was conducted from 0 to 1 ms to capture the temperature evolution under a given applied current I for selected neck heights in the range of 1–20 µm. A manual relative tolerance of 1×10^{-4} was used during the transient runs to ensure accuracy during rapid heating phases.

2.3.2 Simulations with shape changes

The second model incorporated shape evolution to mimic the melting behavior observed in experiments. The same base geometry and the *Electromagnetic Heating* interface were employed as in Section 2.3.1, with additional modifications to enable phase transitions and fluid motion.

To capture the phase transition more realistically, the material was defined with two distinct phases. **Phase 1**, representing the molten solder, was assigned a viscosity of 400 µPa·s, while **phase 2**, representing the solid state, was assigned a viscosity of 400 Pa·s. The transition between these phases was governed by Heaviside phase transition function dependent on several key parameters: the melting temperature of $Sn_{63}Pb_{37}$ (183 °C), a finite transition interval, and the latent heat of fusion. In addition, each phase was described by its own set of thermophysical properties, including thermal conductivity, density, specific heat capacity, and ratio of specific heats. This formulation allowed the simulation to account not only for viscosity changes but also for the energy exchange associated with melting/solidification, thereby avoiding the omission of latent heat losses.

To account for geometry deformation, a moving mesh with a deforming domain was implemented. This was combined with the *Non-Isothermal Flow* multiphysics, which integrates *Laminar Flow* with *Heat Transfer in Fluids*. This coupled approach allowed the simulation to capture the interplay between thermal gradients, fluid dynamics, and electromagnetic heating. The study was time-dependent and extended up to several tens of microseconds, corresponding to the experimental timescale of the melting process. This setup enabled the evaluation of geometry evolution, heat dissipation, current redistribution, and the time-dependent resistance of the system.

3. Results and discussion

To investigate the formation of conductive necks between metallic microspheres under electrical excitation, we designed an experimental setup in which two identical solder balls were rigidly mounted on opposing electrodes. The electrodes, made from sharpened microdrills, were screwed into each sphere to approximately half of its diameter, providing both mechanical stability and robust electrical contact. The spheres were gradually brought into contact along a horizontal axis using a precision micromanipulator (see **Figure 1**).

In this initial series of experiments, we employed a standard laboratory DC power supply equipped with overcurrent protection (OCP). The applied DC voltage was varied between 0 and 30 V to examine the conditions for neck formation under different electrical excitation levels. A current limiter was set to 1.0 A to prevent excessive heating. As the spheres approached each other, they remained electrically isolated until direct mechanical contact was established. At the moment of contact, a surge of current flowed through the system, leading to rapid resistive (Joule) heating localized at the interface and initiating partial melting and neck formation. **Figure 3a** illustrates a representative time sequence showing contact and neck formation during such an experiment (see also the corresponding **Movie S1**).

Once the current limit was reached, the power supply's overcurrent protection was activated, immediately halting further energy input. The process was monitored in real time using an optical microscope equipped with a high-speed camera and backlighting to visualize the outlines of the spheres. In this experimental configuration, the precise durations of the thermal transients following contact could not be resolved due to the temporal limitations of the imaging system and the absence of temperature-time measurements during the transient event. Nonetheless, frame-by-frame analysis confirms that neck formation occurred rapidly, typically within a 1 ms window after contact, followed by near-immediate arrest of sintering growth due to power shutdown.

Post-experiment imaging revealed that the extent of neck formation strongly depended on the applied voltage, which, as we demonstrate later, also influenced the shape of the current profile. Representative experiments performed at voltages ranging from 2.5 to 30 V showed a progressive increase in neck height with increasing voltage. Corresponding post-sintering images for selected voltages are shown in **Figure 3b**.

To quantify this trend, we conducted experiments across a broad voltage range, extracting the average neck height h for each applied voltage U. Plotting these data revealed a clear monotonic increase in h with U, though considerable scatter was observed, likely due to variations in contact geometry, surface roughness, impurities, and local heat transfer conditions. **Figure 3c** summarizes these results, presenting the $h(U)$ dependence based on over 60 individual experiments. A log–log representation of the data suggests that the dependence of h on U follows a power-law behaviour. The fitted curve yields a power-law exponent of approximately 0.71. This scaling may reflect a balance between resistive heating and heat dissipation and warrants further theoretical modelling that incorporates the thermal and electrical properties of the solder material, the geometry of the contact, and the transient nature of the energy input.

For applied voltages above 25 V (in the present geometry and contact scale), occasional local disturbances appeared at the contact region, causing abrupt microparticle separation instead of stable neck formation. At voltages exceeding 30 V, the experiment became less repeatable, with frequent contact disruptions and gap formation. These effects resemble those reported for metallic electrical contacts, where a rapid current increase through a small area induces intense local heating, phase transitions, or microplasma formation.

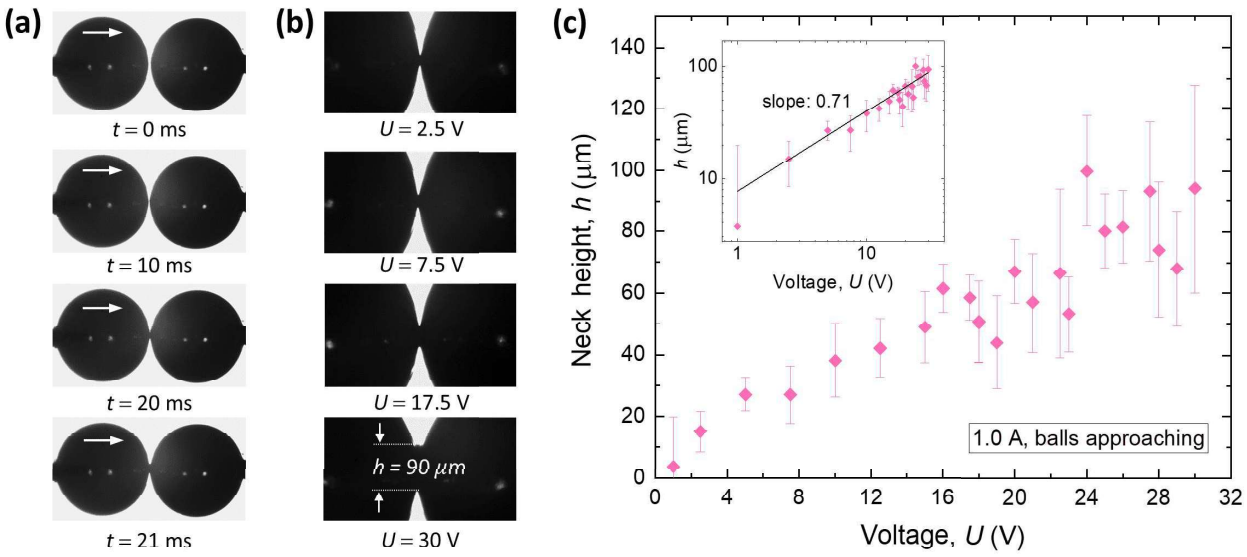

Figure 3. (**a**) Time-resolved optical images of solder spheres during electrically induced neck formation under a constant voltage of 10 V. The spheres, mounted on microdrill-based electrodes, are backlit and observed through a high-speed optical microscope. Contact occurs at ~20 ms, followed by rapid neck formation at ~21 ms due to resistive heating. (**b**) Post-sintering images from four representative experiments conducted at different voltages, showing an increase in neck height (*h*) with increasing applied voltage (*U*). (**c**) Quantitative analysis of the *h(U)* relationship, based on more than 60 experiments. Mean values are shown with standard deviation error bars. The inset presents a log–log plot, and the fitted curve yields a power-law exponent of approximately 0.71.

Sintering of microspheres, which can be applied as a post-processing step for beaded microparticle chains, alters both the mechanical and electrical properties of the structure. Therefore, we first performed simulations to calculate the theoretical maximum resistance for different geometries of microsphere junctions. In these simulations, we assumed ideal physical connections in which the mechanical contact area is identical to the electrical contact area between spheres, neglecting the effects of surface contamination or oxide layers.

The simulation results are presented in **Figure 4a** as the dependence of resistance R on the neck height h. An inset image is included to facilitate visualization of the corresponding geometries. A reference line (independent of h) was also added to represent the case in which two spheres merge to form a cylinder with a length equal to twice the sphere diameter. Such a cylinder, made of leaded solder, would exhibit a resistance of $R = 0.37$ mΩ. In **Figure 4b**, we provide examples of calculated resistances for four different values of neck height, together with color-mapped visualizations of current density distributions within the structures.

The sintered spheres were also characterized experimentally by measuring both the electrical resistance and the mechanical strength of the interparticle junctions. **Figure 4c** presents experimental data together with simulation results as a function of the neck height h. For the experimental data, the values of h were calculated for each applied voltage using the relationship $h(U)$, obtained from the fit of the data points shown in **Figure 3c (inset)**. This enabled the calculated h values to be plotted along the x-axis.

Both datasets show a decrease in resistance with increasing h, although the experimental values remain consistently higher than the simulated predictions. At small neck heights, the experimental resistance values are close to the theoretical curve. As h increases, however, the deviation

becomes more pronounced, with the experimental data lying above the simulated values. These deviations are most likely caused by imperfections not included in the simulations, such as surface contamination, oxide layers, micro-voids at the junction. Another possible factor is the formation of cold joints, which may occur when the particles are insufficiently fused. In such cases, the contact is only partially metallurgical, with residual gaps or weakly bonded regions that increase the effective electrical resistance.

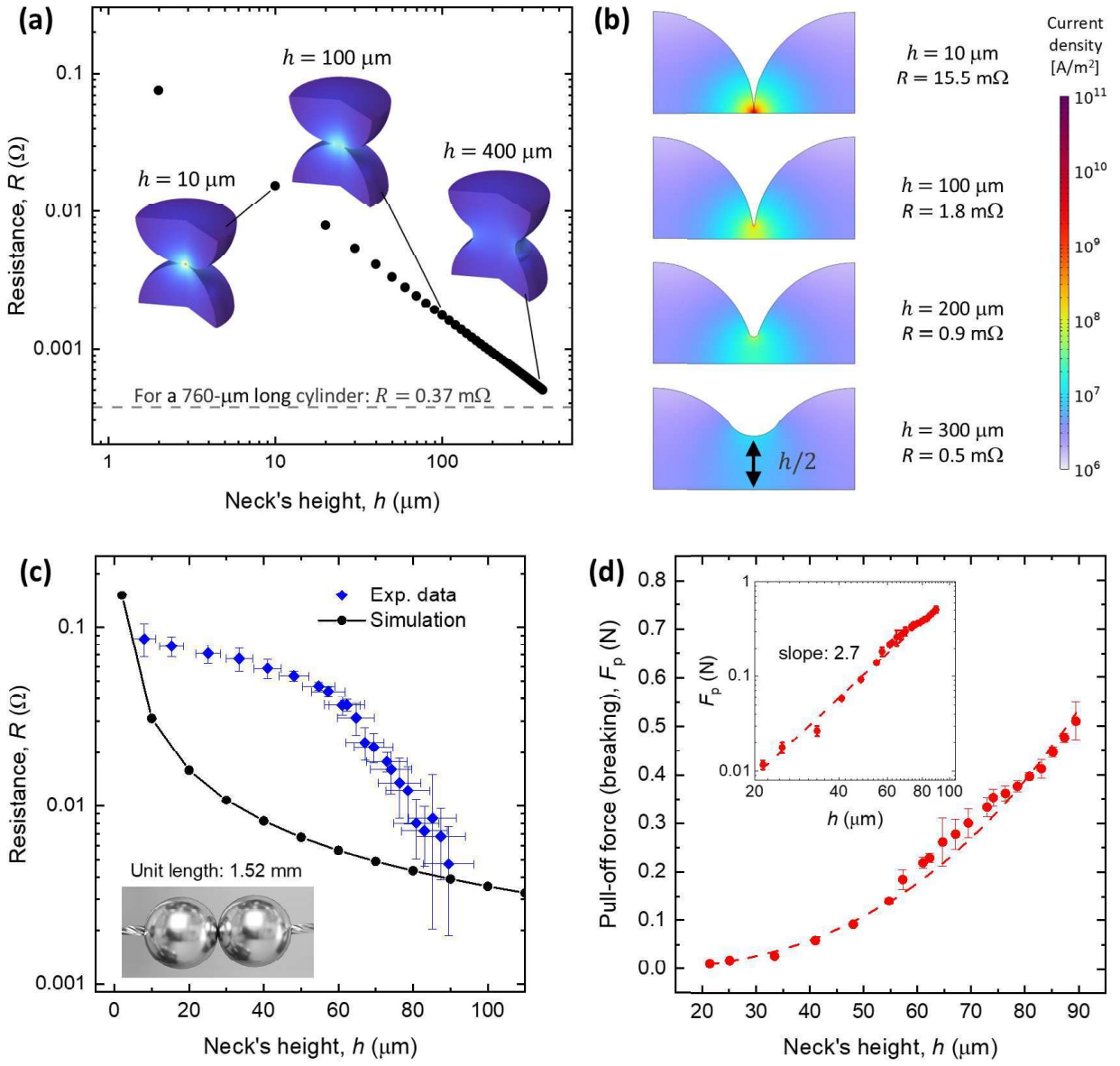

Figure 4. (**a**) Simulated resistance $R(h)$ for different neck heights between two sintered microspheres. Inset images illustrate representative junction geometries. A reference line indicates the resistance of a cylinder with length equal to two sphere diameters (R = 0.37 mΩ). (**b**) Examples of current density distributions for selected neck heights, with corresponding resistance values indicated. (**c**) Experimental $R(h)$ compared with simulation results (red circles). The experimental values remain higher than the simulated ones at small h, but converge toward the theoretical curve for $h \gtrsim 90$ µm. (**d**) Pull-off force F_p versus neck diameter h. The log–log inset yields a slope of ~2.7, indicating additional strengthening at larger neck sizes, consistent with the trend in panel (c).

For larger neck heights (above 60 µm), the discrepancy gradually decreases, and the experimental points converge toward the theoretical prediction for $h \gtrsim 90$ µm. This behavior can be explained by the fact that a sufficiently large contact area makes the current flow dominated by

the overall geometry rather than by local imperfections. As the neck grows, the relative influence of contamination, oxide layers, or partial bonding diminishes, and the electrical path increasingly resembles a continuous metallic cylinder. Moreover, the higher temperatures present at this stage (discussed later) may further improve the quality of the junctions by preventing the formation of cold joints, which otherwise increase resistance.

We also investigated the tensile strength of the junctions. Tensile tests were performed in which the spheres were pulled apart while recording the pulling force required to break the neck. The increase of the tensile force was applied within five seconds, *i.e.*, fast enough to neglect material creep and to examine the mechanical response of the junction as a whole.

The experimental results reveal (see the linear fit in the inset log–log plot) that the pull-off force F_{p} scales with the neck diameter h with an exponent of approximately 2.7. Although the fitted curve does not perfectly follow all data points, the slope clearly exceeds the value of 2. In simple geometric terms, and assuming full metallurgical bonding, one would expect $F_{\mathrm{p}} \propto h^2$, since the load-bearing cross-sectional area at the narrowest part of the junction changes as $A \propto h^2$.

The higher power-law exponent observed here suggests that the scaling cannot be fully explained by geometry alone. At small neck diameters, the effective contact may be limited by incomplete bonding, oxide layers, or micro-defects, resulting in reduced load-bearing capacity. At larger neck diameters, however, once the junction becomes better fused, the effective strength of the contact increases in addition to the cross-sectional area, leading to a steeper dependence. This two-regime behavior could explain why the overall fitted exponent is higher than 2, with the late-stage regime dominating the global trend. Such an interpretation appears consistent with the resistance data in **Figure 4c**, where for small neck diameters ($h < 60$ µm) the measured resistance is significantly higher than the theoretical prediction, which corresponds to a weaker mechanical performance of the junctions in this regime.

To further examine the experimental conditions underlying the sintering process described above, we analyzed the actual current–voltage response during junction formation. As mentioned in the *Methods*, the procedure involved applying a set voltage on the power supply while gradually bringing the microparticles into contact. A current limit (CL) was imposed on the voltage supply, which should, in principle, cut off the voltage once the threshold was reached. However, this cut-off is not instantaneous, and in the case of low-budget power supplies it may last longer and not necessarily occur exactly at the set current limit (here 1 A). It was therefore necessary to verify the true current and voltage signals during such events. For this purpose, the current profile was recorded with an oscilloscope. Representative traces (three series each) for applied voltages of 2.5, 17.5, and 27 V are shown in **Figure 5a**, while the inset of **Figure 5a** plots the maximum current as a function of the applied voltage.

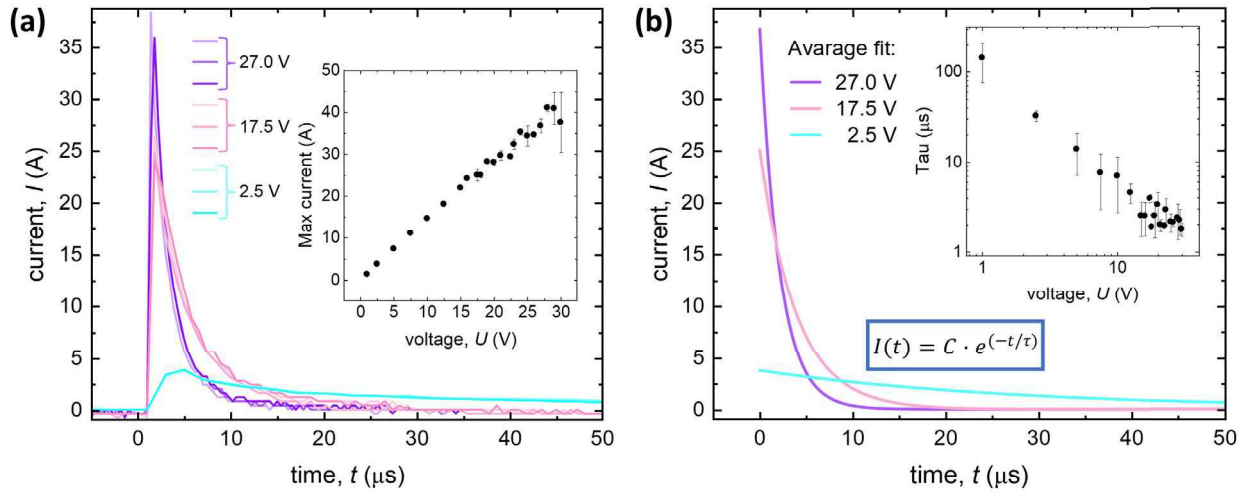

Figure 5. Oscilloscope measurements during sintering experiments with current limiting (CL) in the power supply. (**a**) Representative current traces for three selected voltage settings (2.5, 17.5, and 27.0 V) with the current limit set to 1 A. For each setting, three experiments were performed. All traces exhibit pronounced transient overshoots, with peak currents far exceeding the nominal 1 A limit. The inset shows the averaged maximum current as a function of the applied voltage, highlighting a nearly linear increase up to ~40 A at 30 V. (**b**) Current transients fitted with a first-order exponential decay function, $I(t) = C \cdot e^{(-t/\tau)}$. The averaged fits for the three voltage settings are shown. The inset presents the extracted relaxation time τ as a function of the applied voltage.

These measurements revealed that the nominal CL of 1 A was not reliably maintained by the voltage supply. Instead, sharp transient overshoots occurred, with peak currents reaching tens of amperes before decaying toward lower values. This behavior is typical for many inexpensive voltage sources: once the current approaches the CL threshold, the system attempts to switch off the voltage and reduce the current, but a significant overshoot and delay are introduced. As a result, the junction is briefly exposed to very high current densities, which may induce intense local heating, partial melting leading to micro-fusing at the point of contact, thereby strongly influencing the dynamics of neck formation and contributing to the variability in electrical and mechanical properties observed in the sintered junctions.

To initiate simulations of heat evolution in the solder material under realistic conditions, the electrical signal was modeled based on the oscilloscope data. **Figure 5b** shows representative current decay curves reconstructed by fitting the experimental traces to an exponential function $I(t) = C \cdot e^{(-t/\tau)}$. This functional form reflects the discharge-like behavior of the circuit, where the constant τ characterizes the relaxation dynamics. The inset presents the dependence of τ on the applied voltage, revealing systematically shorter relaxation times at higher voltages. This behavior suggests that higher voltages induce larger transient currents with shorter decay times, producing sharper thermal transients within the junction. These conditions likely enhance localized heat generation and influence the kinetics of neck growth during sintering.

We initiated the thermal simulations by considering the highest applied voltage used in the experiments, *i.e.*, 30 V with the current limit (CL) set to 1 A. Under these conditions, the current signal reached a peak of nearly 44 A within 10^{-8} s and subsequently decayed to zero in less than 10 μs (**Figure 6a**). The rate of temperature increase, and the maximum temperatures attained are expected to depend on the initial contact size between the spheres, which in practice is nonzero.

Therefore, for spheres with a diameter of 760 µm, we simulated initial neck sizes ranging from 4 to 40 µm. It should be noted that in the simulations the area of mechanical contact was assumed to be equal to the area of electrical contact. Importantly, these simulations did not account for morphological changes caused by melting; the structure's geometry was kept fixed, and the shape remained stable over the entire simulated time range (see section 2.3.1).

Figure 6b presents the results of the thermal simulations. It is immediately apparent how rapidly the temperature rises for the smallest initial neck height of 4 µm. To properly capture this effect, the simulations were initialized with a time resolution fine enough that the steep rise began within the first 10^{-15} s, and the same approach was applied to the other cases. The calculated peak temperature for h = 4 µm exceeds 20 thousand °C. This value is clearly unphysical, as solder would vaporize at such temperatures. Instead, it reflects the assumption of a vanishingly small contact area, which yields unrealistically high current densities and excessive Joule heating. In reality, melting occurs at much lower temperatures, where the effective contact area rapidly increases and limits the current density (as discussed later).

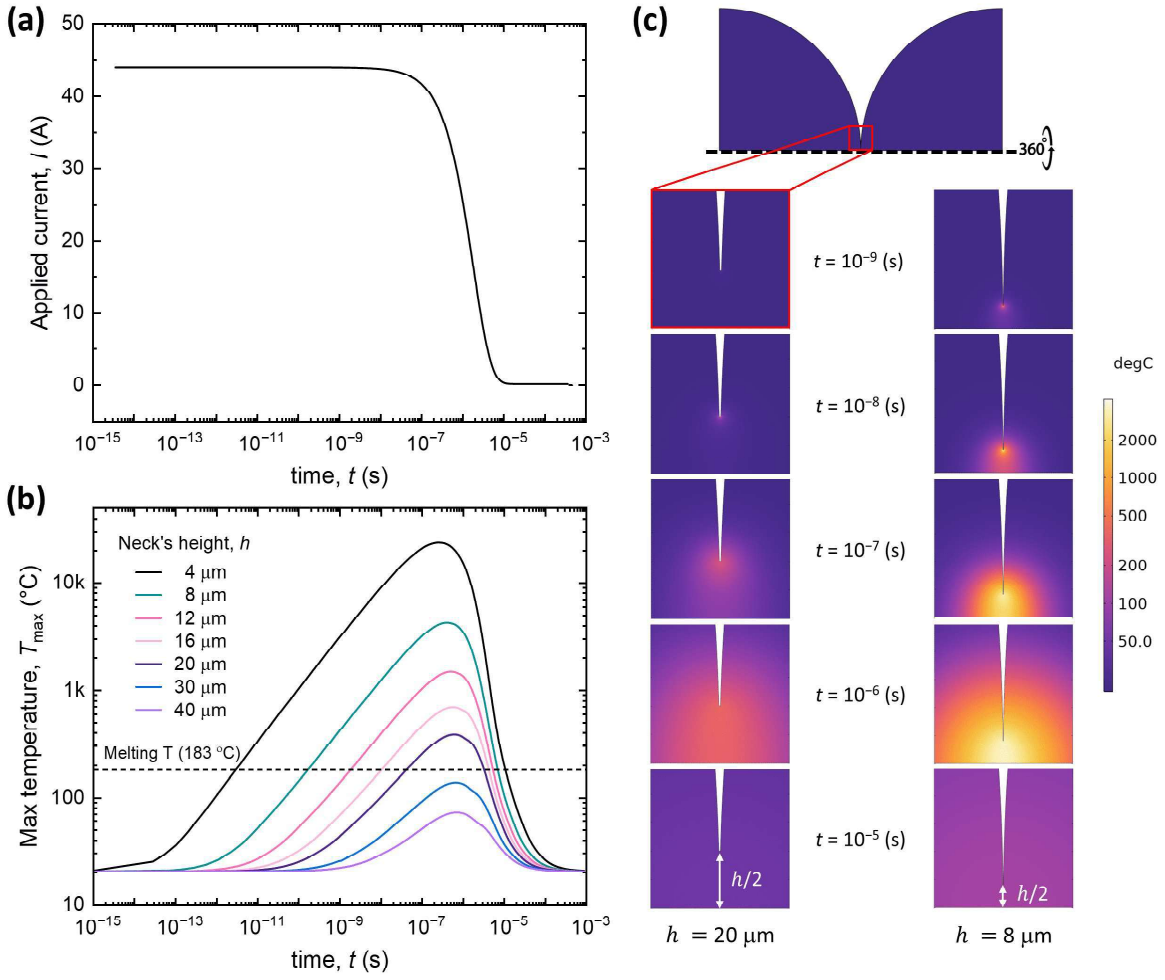

Figure 6. Thermal simulations of solder microsphere junctions under transient current excitation. (**a**) Applied current pulse corresponding to 30 V with a 1 A current limit, peaking near 44 A at 10^{-8} s and decaying to zero within ~10 µs. (**b**) Simulated maximum temperature $T_{\max}(t)$ for neck heights 4–40 µm. Smaller necks give sharp, high peaks (unphysical for h = 4 µm due to excessive current density), while for $h \gtrsim 30$ µm the temperature remains below the solder melting point (183 °C). (**c**) Spatial temperature maps for two neck sizes (h = 20 µm and h = 8 µm). Early times (10^{-9} – 10^{-7} s) show localized heating at the junction, stronger for the smaller neck, whereas later times (10^{-6} – 10^{-5} s) reveal saturation and heat redistribution throughout the spheres.

In **Figure 6c** we compare the spatial temperature evolution for two representative initial neck heights, $h = 20$ µm and $h = 8$ µm. The snapshots illustrate how the temperature field develops during the first microseconds after current application. In both cases, the earliest frames ($t = 10^{-9}$–10^{-7} s) show highly localized heating at the narrowest part of the junction, with considerably stronger hot spots for the smaller neck. At later times ($t = 10^{-6}$–10^{-5} s), the temperature rise saturates, and heat is redistributed throughout the entire particle volume, indicating the onset of cooling and thermal relaxation. These simulations show that smaller necks yield higher peaks with stronger heat localization, while larger necks enable more uniform dissipation.

As the initial neck size increases, both the rate of local heat generation and the maximum temperature decrease. For neck heights $h \gtrsim 30$ µm, the simulated temperature no longer exceeds the melting point of the solder (183 °C). To verify this prediction, we performed experiments in which two spheres were first pressed gently together with a controlled force and subsequently subjected to 30 V with the same current limit (CL) of 1 A as used in the previous experiments. Pressing the spheres together served to create a larger contact area between them.

Figure 7 shows the measured relation between the applied force (F_c) and the resulting contact diameter. The contact area was determined by observing the imprint under an optical microscope after separating the spheres and calculating h as the diameter of the circular mark. In this way, the mechanical contact could be systematically controlled.

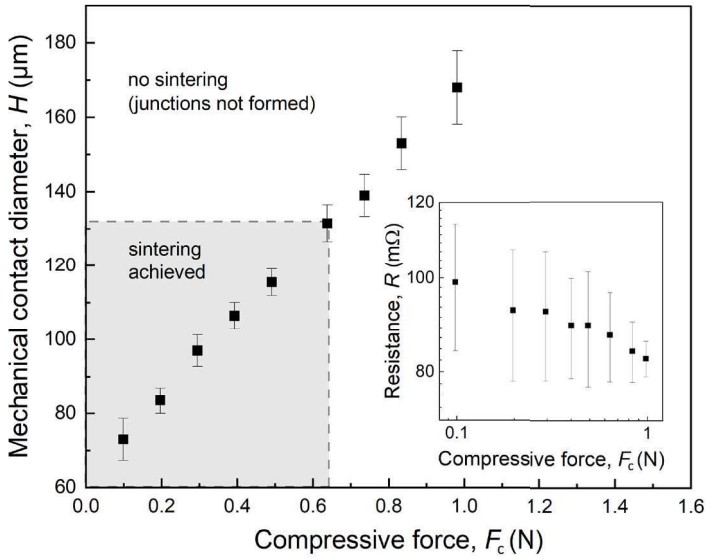

Figure 7. Measured mechanical contact diameter $\boldsymbol{H}$ between solder microspheres as a function of applied compressive force $\boldsymbol{F_c}$ in the absence of electrical excitation. Each point represents the mean value with standard deviation error bars. The shaded region ($\boldsymbol{F_c} \lesssim 0.65$ N, $\boldsymbol{H} \lesssim 130$ µm) corresponds to conditions where sintering was achieved; above this threshold, junctions were not formed. The increase in contact size with load follows the expected trend of elastic–plastic contact mechanics. Inset: Electrical resistance $\boldsymbol{R}$ of mechanically pressed (non-sintered) spheres decreases with increasing force, reflecting improved contact, but remains about an order of magnitude higher than after sintering.

It should be noted, however, that in the simulations the mechanical contact area was assumed to be equal to the electrical contact area, since an ideal metallurgical junction was modeled. In reality, as shown in earlier studies [8, 25], the electrical contact area at low compressive forces (pressures) is significantly smaller than the mechanical contact area, and only at higher pressures

do the two become comparable. Therefore, in the experimental force range of 0.1–1 N, the effective electrical contact area can be assumed to be at least about two times smaller than the measured mechanical contact area. Pressing with an adequate force also resulted in a reduction of resistance (see the inset figure), whose value (before sintering) remained about one order of magnitude higher than that measured after sintering.

Next, an experiment was performed in which, immediately after applying the force (while still maintaining it) and thereby increasing the contact area (results shown in **Figure 7**), a voltage was applied to generate a current pulse. It was observed that for forces below 0.65 N, corresponding to a mechanical contact diameter denoted here as $H \approx 120$ µm (and likely several times smaller for the electrical contact), sintering occurred. For forces above this threshold, however, sintering did not take place, as confirmed by the fact that the spheres could be separated without requiring any measurable pull-off force. In **Figure 7**, two regions are highlighted, indicating the ranges of applied force, mechanical contact diameter H, and initial resistance for which sintering was or was not achieved.

The heating, joining, and solidification of the microparticles is a very rapid process, occurring in less than 1 ms, as mentioned earlier in the description of the results shown in **Figure 2**. This is also confirmed by the simulation data, which indicate that the heating phase itself lasts only a fraction of a millisecond. However, the simulations presented in **Figure 7** concern only heating and heat dissipation, without accounting for phase change, mass transport of the material, or the growth of a larger neck between the spheres.

We next simulated the transient thermal response and neck evolution at the particle junction. **Figure 8a** shows representative snapshots at selected time steps, illustrating the spatial temperature distribution and the region where the temperature exceeds the melting point (outlined in red), indicating the presence of the liquid phase inside the contour. Due to the symmetry of the model, only half of the neck height is shown and marked as $h/2$. The current pulse used in the simulation has the same amplitude and duration as the one shown in **Figure 6a**. As the current pulse is applied, rapid Joule heating leads to localized melting at the contact region within sub-microsecond timescales. The corresponding movie is provided in the Supplementary Information (**Movie S2**).

Figure 8b presents the temporal evolution of the maximum temperature $T_{\max}(t)$ within the junction. After an initial rise, the temperature reaches a peak and then decreases as the input pulse decays and heat dissipates into the surrounding material. Heat dissipation occurs more slowly than the initial heating, since it relies solely on thermal conduction after the current pulse ends. **Figure 8c** shows the time evolution of the neck height $h(t)$. Initially, the neck size is 20 µm and remains unchanged. As heating progresses, localized melting leads to rapid neck growth, reaching a final size of about 25 µm. After the input pulse decays and the temperature drops, the molten region solidifies, and the neck height stabilizes. Further growth is arrested due to the lack of continued energy input.

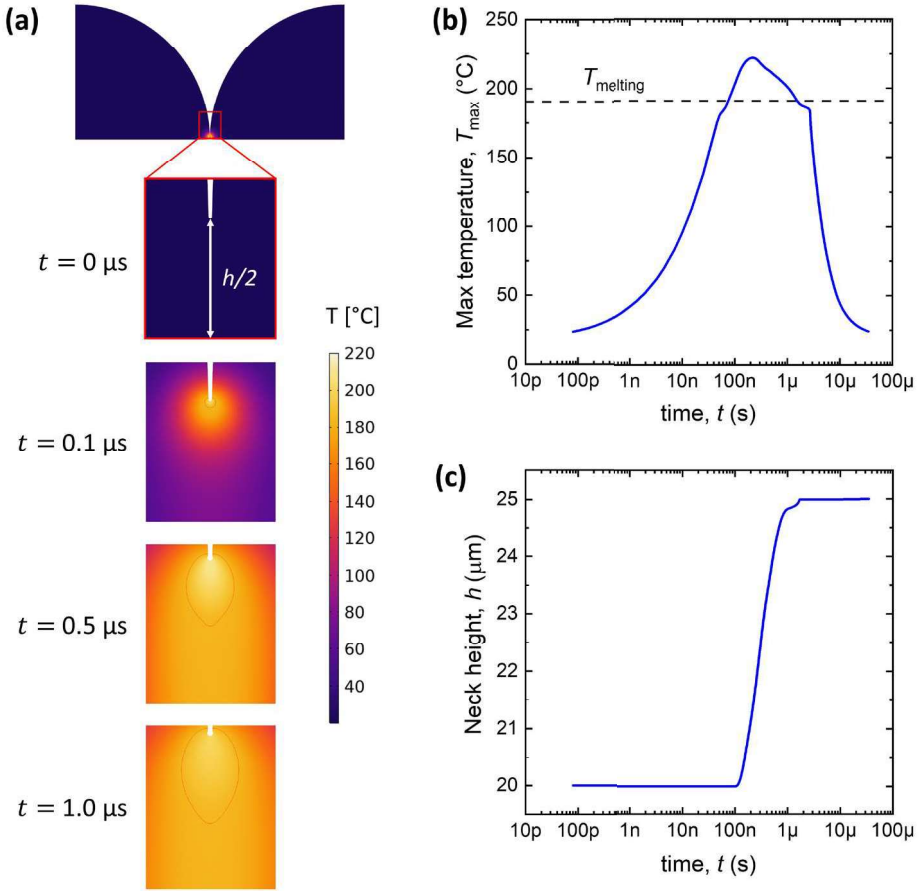

Figure 8. Simulation of transient heating and neck growth under a current pulse. (**a**) Temperature maps and liquid phase formation (inside the red contour) at selected time steps. See also the corresponding **Movie S2**. (**b**) Maximum temperature $T_{\max}(t)$ in the junction as a function of time. (**c**) Evolution of neck height $h(t)$; the initial value of h =20 µm increases to approximately 25 µm before stabilizing. The applied current pulse corresponds to that shown in Figure 6a.

Let us note that the neck height increased by just under 5 µm, reaching approximately 25 µm. This is significantly less than what was observed in experiments using a similar current pulse, where for an applied voltage of $U = 30$ V and peak currents reaching 44 A, the neck height grew to approximately 100 µm. This discrepancy can be explained by the fact that, in the experiment involving the approach of two solder spheres, the initial electrical contact area is extremely small. Therefore, the initial neck height is expected to be no more than a few micrometers. As a result, when analyzing the data in **Figure 6b**, particularly for the smallest initial contact size, it becomes evident that the temperature rises more rapidly and to higher values, but most importantly, it remains above the solder's melting point for nearly three times longer (approximately up to 10 µs) compared to the case where the initial contact area is 20 µm. This longer heating duration, combined with the melting of a larger portion of the contacting spheres, facilitates the formation of a more substantial volume of liquid phase and thus enables the formation of a much larger neck.

Following this reasoning, we performed additional simulations in which a constant current of 44 A was maintained (instead of a decaying pulse), as well as simulations with a fixed power input of 7.65 W, corresponding to the initial power generated by a 44 A current through the contact resistance of the spheres for $h = 20$ µm.

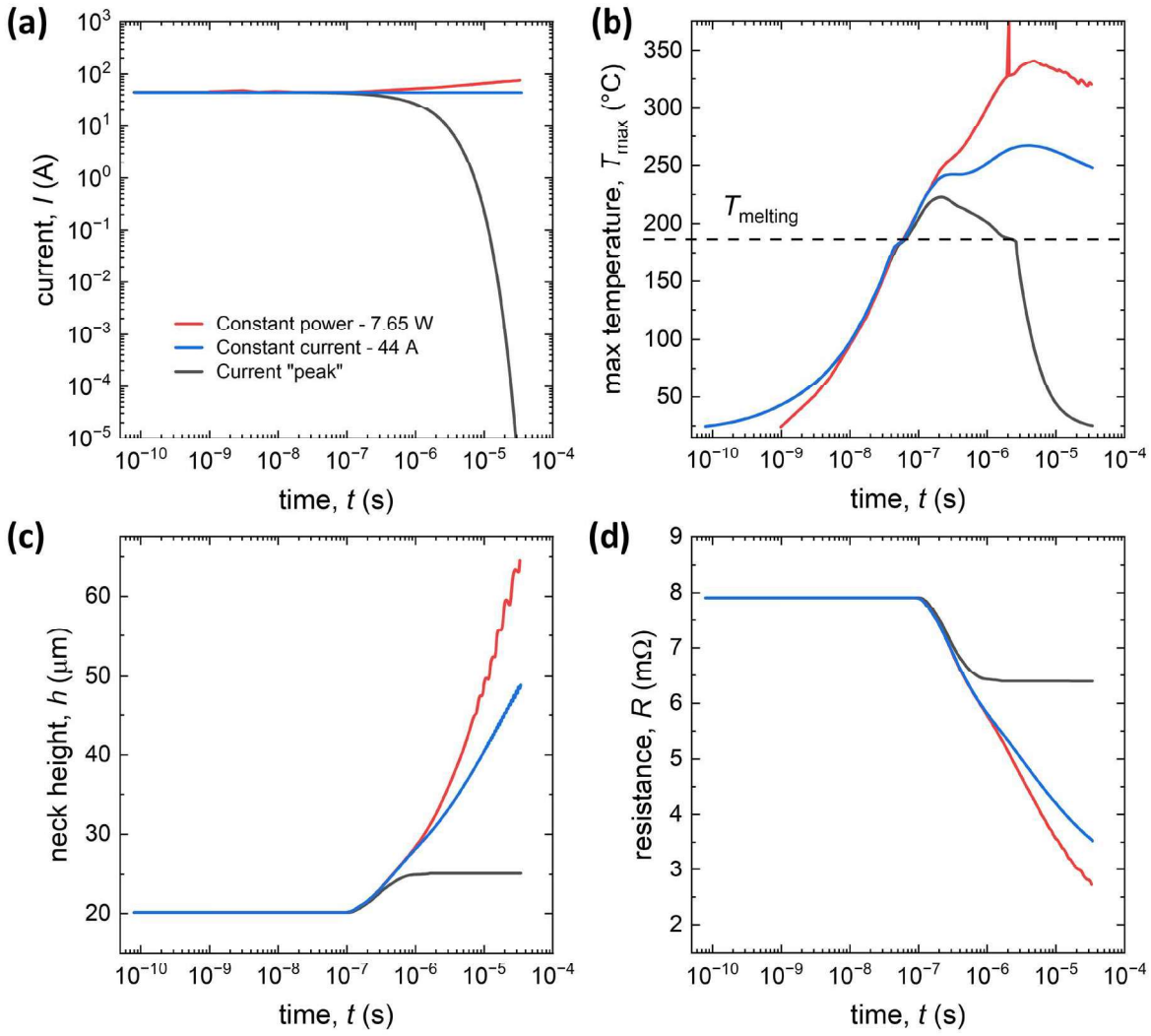

Figure 9. Simulation results for three electrical excitation scenarios: constant power input of 7.65 W (red), constant current of 44 A (blue), and experimentally measured current pulse (black). (**a**) Input current waveforms. (**b**) Evolution of the maximum temperature at the particle junction, with the dashed line indicating the melting point of the solder. (**c**) Time-dependent neck height $h(t)$; the highest neck growth is observed for the constant power case due to increasing current. (**d**) Evolution of electrical resistance $R(t)$; both constant current and constant power lead to continuous resistance reduction, with the steepest decrease observed under constant power conditions.

Figure 9a shows the current waveforms used in the simulations: the experimentally measured transient current (black), a constant current of 44 A (blue), and a constant power input of 7.6498 W (red), corresponding to the initial power in the experimental case. These different excitation modes lead to significantly different thermal responses, particularly in terms of maximum temperature and heat accumulation near the particle junction, as shown in **Figure 9b**. Notably, both constant current and constant power inputs result in higher peak temperatures and longer dwell times above the melting point compared to the experimental pulse.

Figure 9c presents the evolution of the neck size (radial joint growth) over time for the three cases. In the experimental scenario (black curve), neck growth slows down significantly around 1 µs and eventually stabilizes at approximately 25 µm. In contrast, under constant current, the neck continues to grow beyond this point, although the growth rate gradually decreases. For the constant power case, the neck grows most rapidly and continues to increase even at later times.

This is attributed to the increasing current resulting from decreasing resistance as the molten bridge between the particles improves electrical contact.

Figure 9d shows the time-dependent evolution of electrical resistance between the spheres. In the experimental case, resistance initially drops and then levels off. In the constant current and constant power simulations, the resistance continues to decrease throughout the simulation, with the power-controlled case showing the steepest drop, reflecting the strong feedback between improved conduction and sustained energy input.

These results suggest that, with a more advanced electronic control system capable of regulating either current or power, it is possible to deliver a signal of sufficient duration to achieve a desired bridge size, and thus a target resistance value, while also ensuring adequate mechanical stability of the structure (see also **Figure 4d**).

Figure 10 presents the evolution and scaling behavior of the neck height h as under constant power input. Panel (a) shows the temporal evolution of h for a range of power levels (1–7 W), with dashed lines indicating selected time points in range 0.3–10 µs. As the power increases, the neck grows more rapidly and reaches greater heights within the same time window. Panel (b) summarizes these results by showing the increase in neck heightΔh (measured from the initial value of $h = 20$ µm) at different times, plotted as a function of power. The observed relationship highlights the high sensitivity of early-stage neck growth to power input.

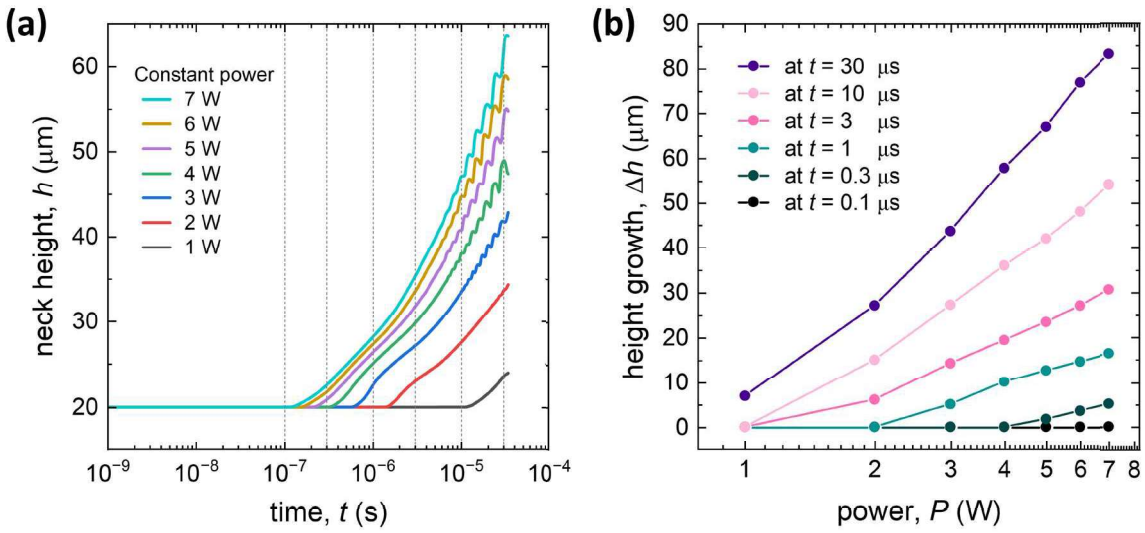

Figure 10. Evolution and scaling of neck height h under constant power input. (**a**) Temporal evolution of h for various power levels (1–7 W); vertical dashed lines indicate selected time points used for comparison in panel (b). (**b**) Neck height increase Δh (measured from the initial value of 20 µm) as a function of power, shown for multiple time points (0.1–30 µs). The results highlight the nonlinear dependence of neck growth on both power and time.

The results presented in **Figure 10b** indicate the possibility of relatively precise control over the connection between a pair of solder microparticles. However, it should be noted that the evolution of the junction is also strongly influenced by the initial mechanical (and thus also electrical) contact between the spheres. This raises the question of whether similar connections between particles would form in the same manner in a chain composed of more than two microparticles.

We conducted experimental studies in which five solder microparticles were arranged in a linear configuration. Four particles were placed in direct contact with each other to form a static chain, while the fifth particle, mounted on a microdrill, was gradually approached the particle chain from a side at a speed of several micrometers per second. A voltage of 30 V with a CL of 1 A was applied to the outermost microparticles. Upon approach, localized heating occurred at the contact points, leading to the formation of a conductive and mechanically stabilized chain.

The top image in **Figure 11** shows the structure shortly after sintering, which lasted only a few microseconds. We then carried out a complementary experiment in which microparticles of different sizes (760 µm and 400 µm in diameter) were used. Despite the size mismatch, stable sintering bridges formed between all adjacent particles, as shown in the bottom panel of **Figure 11**. These results demonstrate that the sintering process is robust against moderate geometric irregularities and confirm that conductive bridges can be simultaneously formed across multiple contacts, enabling the creation of extended, electrically continuous chains of microparticles.

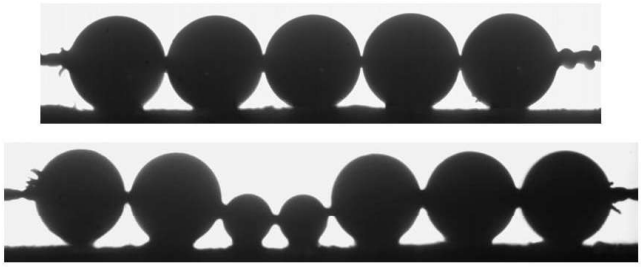

Figure 11. Formation of conductive chains of solder microparticles under an applied voltage of 30 V with Cl of 1 A. (**Top**) Chain of five identical microparticles (760 µm), sintered within a few microseconds after contact of the approaching particle. (**Bottom**) Chain composed of large (760 µm) and small (400 µm) microparticles, showing stable sintering bridges despite the size mismatch. The solder balls were placed on Scotch tape to facilitate their alignment.

4. Conclusions

In this study, we investigated the formation and evolution of conductive junctions between solder microparticles under electrical excitation using a combination of experiments and numerical simulations. The results demonstrate that Joule heating at the particle junction leads to rapid local melting and the development of stable sintering bridges within microsecond timescales. By varying the applied voltage, current, and power profiles, we showed that both the rate and the extent of neck growth can be tuned, with constant power control providing the most pronounced and sustained neck formation.

The simulations captured the transient interplay between thermal gradients, current flow, and liquid–solid phase transitions, reproducing the experimentally observed growth trends and highlighting the sensitivity of neck formation to both power input and initial contact geometry. Experimental results with chains of multiple microparticles further confirmed that conductive bridges can form simultaneously across several junctions, yielding mechanically robust and electrically continuous structures even when the particles differ in size.

An interesting observation is that the system exhibits a degree of self-regulation: under appropriately chosen electrical parameters, localized melting and neck growth reduce the junction resistance, which in turn lowers the Joule heating within the chain. As a result, the temperature can drop below the melting point, effectively halting further neck expansion.

Overall, these findings demonstrate the feasibility of controlling microscale sintering by tailoring electrical excitation parameters. This opens pathways for designing advanced electronic control systems capable of regulating current or power to achieve precise junction geometry, desired electrical resistance, and mechanical stability in particle-based conductive microstructures.

This work can be further extended by addressing several open questions. One important direction is to investigate in more detail the influence of particle polydispersity, as well as the effect of particle arrangement, including non-linear and irregular structures, on the stability and reproducibility of neck formation. Another aspect is to determine the lower size limit of solder microparticles that still allows for effective control of the process.

Future studies may also explore other materials, including different solder alloys and metallic microparticles such as silver, copper, and related systems, which are among the most widely used metals in printed and flexible electronics. Such extensions would be directly relevant to metallization strategies in silicon-based solar cells, as well as other emerging applications across different fields. Examples include stretchable interconnects, wearable electronics in the area of flexible systems; plasmonic and photonic structures where periodicity and controlled height-to-width ratios determine optical properties; catalytic architectures with enhanced surface-to-volume ratios; acoustic metamaterials exploiting ordered microsphere arrangements; and bioelectronics, where engineered particle chains could be used as structured, conductive, and mechanically compliant interfaces.

Statement

During the preparation of this work, we utilized an AI-powered writing assistant, Grammarly, solely to enhance readability and language clarity. Following the use of this tool, we meticulously reviewed and edited the content. Therefore, we take full responsibility for the content of the publication.

Conflicts of interest

There are no conflicts of interest to declare.

Author contributions

Z. Rozynek initiated the project at CADENAS p.s.a, Poland, co-designed all experiments, and performed the experiments with results presented in Fig. 3. Y. Harkavyi developed methodology for preparing solder balls on microdrills, co-designed and performed experiments with results shown in Fig. 4a–c, Fig. 5b, Fig 6, Figs 8–10, and Movie S2. M. Solovan co-design and performed experiments with results shown in Fig. 4d, Fig. 5, Fig. 7 and Fig. 11. Harkavyi wrote the first version of the manuscript. All authors took part in discussions toward the finalization of the manuscript.

Acknowledgments:

We wish to acknowledge CADENAS P.S.A. (Poland) for initiating the project, providing the preliminary data that formed the basis of this study, and supporting the research through access to infrastructure and materials. Part of this work (M. Solovan) was supported by the Polish National Science Centre under the OPUS call (Grant No. 2022/45/B/ST5/03529). We thank the Department of Physics and Astronomy at Adam Mickiewicz University for providing access to their high-performance computing facilities used for the simulations. We are grateful to Hryhorii Parkhomenko for his assistance with the experimental work, and to Dr. Konrad Giżyński for his valuable guidance and insightful suggestions that contributed to the numerical simulations.

References:

[1] B. Grübel, G. Cimiotti, C. Schmiga, et al., Progress of plated metallization for industrial bifacial TOPCon silicon solar cells, Progress in Photovoltaics: Research and Applications 30(6) (2022) 615-621.
[2] M. Hendrichs, M. Padilla, J. Walter, et al., Screen-Printed Metallization Concepts for Large-Area Back-Contact Back-Junction Silicon Solar Cells, IEEE Journal of Photovoltaics 6 (2015) 1-10.
[3] K.T. Fujimoto, J.K. Watkins, T. Phero, et al., Aerosol jet printed capacitive strain gauge for soft structural materials, npj Flexible Electronics 4(1) (2020) 32.
[4] S. Khan, S. Ali, A. Bermak, Smart Manufacturing Technologies for Printed Electronics, in: R. Vargas-Bernal, P. He, S. Zhang (Eds.), Hybrid Nanomaterials - Flexible Electronics Materials, IntechOpen, London, 2019.
[5] Z. Rozynek, A. Magdziarz, Process of fabricating a beaded path on the surface of a substrate, a system for fabricating such a path, use thereof, and a kit (EP3831171B1), in: E.P. Office (Ed.) CADENAS p.s.a., Poland, 2022.
[6] Z. Rozynek, A. Magdziarz, U.S. Patent No. 11,856,709, CADENAS p.s.a., Poland, Washington, DC, 2023.
[7] Z. Rozynek, Y. Harkavyi, K. Giżyński, Fabrication of 1D particle structures outside a liquid environment using electric and capillary interactions: From fundamentals to applications, Materials & Design 223 (2022).
[8] Z. Rozynek, Y. Harkavyi, Ø.G. Martinsen, et al., Fabrication of a new type of electrically conductive micro-tracks via mechanical compression of beaded structures, Materials & Design 253 (2025) 113985.
[9] R.R. Collino, T.R. Ray, R.C. Fleming, et al., Acoustic field controlled patterning and assembly of anisotropic particles, Extreme Mechanics Letters 5 (2015) 37-46.
[10] F. Dutka, Z. Rozynek, M. Napiorkowski, Continuous and discontinuous transitions between two types of capillary bridges on a beaded chain pulled out from a liquid, Soft Matter 13(27) (2017) 4698-4708.
[11] S. Feng, S. Cao, Z. Tian, et al., Maskless Patterning of Biodegradable Conductors by Selective Laser Sintering of Microparticle Inks and Its Application in Flexible Transient Electronics, ACS Appl Mater Interfaces 11(49) (2019) 45844-45852.
[12] S. Zhang, Y. Liu, Y. Qian, et al., Manufacturing with light - micro-assembly of opto-electronic microstructures, Optics Express 25(23) (2017) 28838.
[13] C. Stephenson, A. Hubler, Stability and conductivity of self assembled wires in a transverse electric field, Scientific Reports 5 (2015).
[14] Y. Harkavyi, K. Giżyński, Z. Rozynek, Experimental and FEM simulation study of compressive deformation of solder microballs and particle chains, Soft Matter 21(22) (2025) 4393-4406.
[15] C. Balemans, N.O. Jaensson, M.A. Hulsen, et al., Temperature-dependent sintering of two viscous particles, Additive Manufacturing 24 (2018) 528-542.
[16] P. Hejmady, L.C.A. van Breemen, P.D. Anderson, et al., Laser sintering of polymer particle pairs studied by in situ visualization, Soft Matter 15(6) (2019) 1373-1387.

[17] F. Klocke, C. Wagner, Coalescence behaviour of two metallic particles as base mechanism of selective laser sintering, CIRP Annals 52(1) (2003) 177-180.
[18] L. Shen, Y. Wang, J. Cheng, et al., Origin of micro-scale local hotspots during the microwave processing of the YBCO conductive ceramics, Scripta Materialia 216 (2022).
[19] T.B. Holland, U. Anselmi-Tamburini, D.V. Quach, et al., Effects of local Joule heating during the field assisted sintering of ionic ceramics, Journal of the European Ceramic Society 32(14) (2012) 3667-3674.
[20] A.S. Rogachev, S.G. Vadchenko, V.A. Kudryashov, et al., Direct Observation of Processes at Particle-to-Particle Contacts during Electric Pulse Consolidation of a Titanium Powder, Doklady Physical Chemistry 488(2) (2019) 151-153.
[21] W. Ren, C. Zhang, X. Sun, Electrical Contact Resistance of Contact Bodies With Cambered Surface, IEEE Access 8 (2020) 93857-93867.
[22] E. Falcon, B. Castaing, M. Creyssels, Nonlinear electrical conductivity in a 1D granular medium, The European Physical Journal B - Condensed Matter and Complex Systems 38(3) (2004) 475-483.
[23] S. Dorbolo, A. Merlen, M. Creyssels, et al., Effects of electromagnetic waves on the electrical properties of contacts between grains, Europhysics Letters 79(5) (2007) 54001.
[24] J.A. Greenwood, J.B.P. Williamson, Electrical conduction in solids II. Theory of temperature-dependent conductors, Proceedings of the Royal Society of London. Series A. Mathematical and Physical Sciences 246(1244) (1958) 13-31.
[25] C. Zhang, W. Ren, X. Liao, On the Relationship between Contact Resistance and Load Force for Electrode Materials with Rough Surfaces, Materials (Basel) 15(16) (2022).

Formation of conductive beaded structures via Joule heating

Harkavyi[1†*], M. Solovan[2], and Z. Rozynek[1†]

[1] *CADENAS P.S.A., Prof. Sylwestra Kaliskiego 24, 85-796 Bydgoszcz, Poland*
[2] *Faculty of Physics and Astronomy, Adam Mickiewicz University, Uniwersytetu Poznańskiego 2, 61-614 Poznań, Poland*

[†]These authors contributed equally to this work. [*]Corresponding author: zbiroz@amu.edu.pl

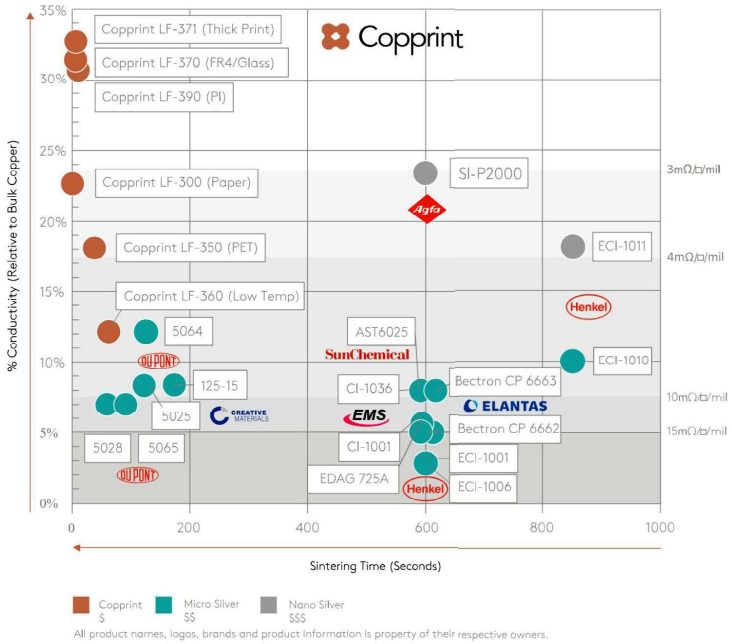

Figure S1. Comparison of the performance of conductive pastes based on various nano- and sub-micro materials, including copper and silver. Illustration adapted from promotional materials by Copprint, available at https://www.copprint.com.

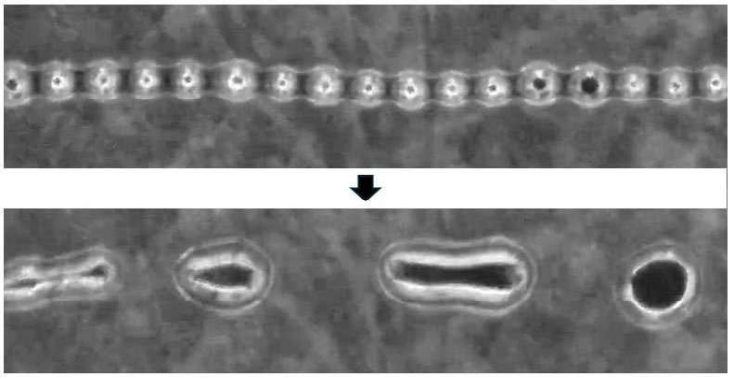

Figure S2. Top-view image (taken along the gravity direction) showing structural disruption in a chain of 200 µm solder microparticles after uniform thermal treatment on a hot plate (~300 °C). The excessive and homogeneous heating caused complete coalescence of neighboring spheres, resulting in isolated metallic islands and loss of electrical continuity along the original beaded path.

Movie S1. Connection through the approach of spheres under voltage: Formation of a conductive neck between two solder microspheres under electrical excitation (30V DC, 1A current limit). The spheres are rigidly mounted on microdrill-based electrodes and gradually brought into contact. The neck forms within ~1 ms after contact due to localized resistive heating. The process is captured using high-speed optical microscopy with backlighting.

Movie S2. Simulation results illustrating the growth of the neck between the spheres: Simulation of temperature evolution and conductive neck formation between two solder microspheres under a defined transient current, $I(t) = I_o e^{-t/\tau}$, with $I_o = 44$ A and $\tau = 1.95$ µs. The spheres are initialized with a contact radius corresponding to $h/2 = 10$ µm.

8. Statements of co-authors

Dr. hab. Zbigniew Rozynek
zbiroz@amu.edu.pl

29-09-2025

Co-author statement

I hereby declare that I contributed to the following publications:

- **Fabrication of 1D particle structures outside a liquid environment using electric and capillary interactions: From fundamentals to applications**, *Materials & Design* **223**, 111233 (2022) by formulating the scientific hypotheses, co-designing all experiments, and performing the experiments with results presented in Figs. 3a,d,e,h, Figs. 4a,c, Fig. 5, Fig. 6, Figs. 7a–e,g, Fig. S1a, Fig. S1b, Fig. S2, Fig. S3 and Fig. S5;
- **Fabrication of a new type of electrically conductive micro-tracks via mechanical compression of beaded structures**, *Materials & Design* **253**, 113985 (2025) by initiating the project, formulating the scientific hypotheses, co-designing all experiments, performing the experiments with results presented in Fig.4-9, Fig.11, Fig.13, Fig.S5, Fig.S7, Fig.S10-S12, and Movies S7-9, and administering the submission and the review process. Z. Rozynek and Y. Harkavyi contributed equally to this work;
- **Experimental and FEM simulation study of compressive deformation of solder microballs and particle chains**, *Soft Matter* **21**, 4393–4406 (2025) by co-designing, performing experiments with results shown in Figs. 2-4, 7-9, and taking part in discussions toward the finalization of the manuscript;
- **Single-particle-thick microstructures fabricated through controlled withdrawal of particles from a dispersion meniscus,** *Materials & Design* **255,** 114160 (2025) by co-designing all experiments, performing the experiments presented in Figs. 4c, 9b, 12–16, and S3, as well as in Movies 1 and 8–11, and co-performing with Y. Harkavyi the experiments shown in Figs. 2 and 6;

and to the following manuscript draft by Y. Harkavyi, M. Solovan M. and Z. Rozynek with its current title: **Formation of conductive beaded structures via Joule heating** by co-designing all experiments and performing the experiments with results presented in Fig. 3.

Sincerely yours

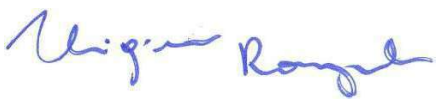

Zbigniew Rozynek

Signature valid
Dokument podpisany przez Zbigniew Jerzy Rozynek
Data: 2025.09.29 00:34:14 CEST

UNIVERSITY
OF OSLO

To whom it may concern

Date: 29.09.2025

Co-author Statement

I hereby declare that I am a co-author of the following publication:

Rozynek Z., Harkavyi Y., Martinsen Ø.G., Giżyński K., Fabrication of a new type of electrically conductive micro-tracks via mechanical compression of beaded structures. Materials & Design, Volume 253, May 2025, 113985

My contribution consisted of provision of equipment, discussions, reviewing and editing of the manuscript.

Yours sincerely,

Ørjan G. Martinsen
Professor, Dr. Scient.

Faculty of Mathematics and Natural Sciences
Department of Physics
Electronics Section

Postal address:
P.O. Box 1048 Blindern
N-0316 Oslo
Norway

Visiting address:
Sem Sælands vei 24
N-0371 Oslo
Norway

Phone: +47 22856474
Fax/Mobile: +47 91103411
E-mail: ogm@fys.uio.no
Web: www.bioimpedance.org

Dr. Konrad Gizynski

kgizynski@ichf.edu.pl

29-09-2025

Co-author Statement

I hereby declare that I contributed to the following publications:

- **Fabrication of 1D particle structures outside a liquid environment using electric and capillary interactions: From fundamentals to applications**, *Materials & Design* **223**, 111233 (2022) by co-designing and performing the experiments with results presented in Fig. 8c,d and taking part in discussions toward the finalization of the manuscript;

- **Fabrication of a new type of electrically conductive micro-tracks via mechanical compression of beaded structures**, *Materials & Design* **253**, 113985 (2025) by co-designing and performing the experiments with results presented in Figs.2-3, Fig.5, Fig.9, Figs.11-12, Fig.S3-S4, Fig.S6, and Movies S3-6 and S9, and taking part in discussions toward the finalization of the manuscript;

- **Experimental and FEM simulation study of compressive deformation of solder microballs and particle chains**, *Soft Matter* **21**, 4393–4406 (2025) by co-designing, performing experiments with results shown in Figs. 4–10 and taking part in discussions toward the finalization of the manuscript;

Sincerely Yours,

Signed by / Podpisano przez:
KONRAD GIŻYŃSKI
Date / Data: 2025-09-29 12:34

Konrad Giżyński

Co-author Statement

I hereby declare that I am a co-author of the following manuscript draft:

Y. Harkavyi, M. Solovan and Z. Rozynek. Formation of conductive beaded structures via Joule heating.

My contribution consisted of supporting selected experimental measurements, co-designing and performing experiments with results shown in Fig. 4d, Fig. 5, Fig. 7, and Fig. 11, assisting in data discussion, and providing comments during the manuscript preparation.

Sincerely Yours,

Mykhailo Solovan

Signed by /
Podpisano przez:

Mykhailo Solovan

Date / Data:
2025-09-28 18:21

Co-author Statement

I hereby declare that I am a co-author of the following publication:

Y. Harkavyi, G. Tiwari, Z. Rozynek, Single-particle-thick microstructures fabricated through controlled withdrawal of particles from a dispersion meniscus.
Materials & Design, Volume 255, 2025, 114160.

My contribution consisted of writing – review & editing, visualization and investigation.

Sincerely Yours,

Gunjan Tiwari

Appendix A: G-code for performing experiments of pulling chain

It should be noted that this script was specifically developed and validated for our modified 3D printer; since G-code implementations may differ between machines, adjustments could be required for other hardware platforms.

Macro Commands	Action	Experimental process step
M3 P5	Spindle on (clockwise), low speed	Spin-up before embedding
G4 P500	Dwell 0.5 s	RPM stabilization
G0 Z-0.5 F30	Lower tool toward sphere at controlled feed	Controlled insertion toward midpoint
M5	Spindle off	Stop after reaching target depth
G4 P1000	Dwell 1 s	Settle before retract
G0 Z0.5 F100	Small retract	Release pressure
G4 P2000	Dwell 2 s	Confirm release
G0 Z40 F1000	Retract to safe height	Clear for bit detachment and next sample

Note for Reproducibility

Before running this G-code sequence, the following setup steps are required:

- **Particle installation:** Place the solder particle into the holder (support tube) so it is stable.
- **Drill bit preparation:** Install the drill bit into the CNC toolhead and tighten it securely.
- **Positioning:** Set the machine's coordinate system so that the drill bit is aligned directly above the sphere, with the tip facing its center at the surface level.

This ensures that the automated sequence embeds the drill bit properly into the particle without misalignment or unintended damage.

Appendix B: Automated electro-thermal simulations in COMSOL

Paste this script (Java) in **COMSOL → Developer → Application Builder → New Method**, then run it. **Before run, do one manual solve** to verify the physics and to create the result objects the code expects (*e.g.*, gloR, maxT, tblR, tblT). After that, the script will batch-run all ~80 compression states so you don't repeat the steps manually.

Update these to match your model:

- **Paths & filenames** (imported geometries), number of states.
- **IDs**: study (std1/stat), geometry import (imp1), mesh (mesh1).
- **Inputs**: contact-load parameter name (*e.g.*, p_contact).
- **Results**: expressions for resistance (*e.g.*, ec.R or V/I) and temperature (T), plus any selections.

```
// --- Batch electro-thermal run across many compression states ---
// Adjust these to your model before running:
int N = 80;                                                    // <TOTAL_NUMBER_OF_STATES>
int startIndex = 1;                                            // <FIRST_STATE_INDEX>
String BASE_DIR = "<PATH_TO_YOUR_FILES>/";                     // e.g., "D:/exports/"
String NAME_FMT = "<FILENAME_PATTERN_WITH_%d>.mphbin";         // e.g., "760um_1.mphbin"

// electrical contact pressure parameter, set it here per state.
double[] pContact = new double[] {
 /* <PUT_YOUR_PER_STATE_CONTACT_PRESSURES_HERE_IN_PA> */
 // e.g., 1.0e5, 1.1e5, 1.2e5, ...
};

boolean first = true;                          // first iteration writes new rows; next ones append

for (int k = 0; k < N; k++) {
 int j = startIndex + k;

 try {
  // ---- 1) Import geometry for state j and remesh ----
  String filePath = BASE_DIR + String.format(NAME_FMT, j);   // <- <PATH> + formatted filename
  model.component("comp1").geom("geom1").feature("imp1").set("filename", filePath);
  model.component("comp1").geom("geom1").feature("imp1").importData();
  model.component("comp1").geom("geom1").run();              // rebuild geometry
  model.component("comp1").mesh("mesh1").run();              // rebuild mesh
```

```
    // ---- 2) Apply contact pressure (if used in your BC) ----
    // Comment out if not applicable in your model
    if (pContact.length > 0) {
      model.param().set("p_contact", Double.toString(pContact[k])); // <RENAME_IF_NEEDED>
    }

    // ---- 3) Run the coupled electro-thermal study ----
    // Ensure your study "std1" has a stationary step "stat" that solves EC + HT (+ Joule heating).
    model.study("std1").run();

    // ---- 4) Save resistance & max temperature to tables ----
    // Pre-create numerical evaluations in the model:
    //   "gloR" -> Global Evaluation of resistance (e.g., ec.R or V/I)
    //   "maxT" -> Maximum of T (limit to solids via a selection if needed)
    // Tables will be created automatically on first pass.
    if (first) {
      // Create result tables and write first row
      model.result().table().create("tblR", "Table");
      model.result().table("tblR").label("Resistance vs Compression");
      model.result().numerical("gloR").set("table", "tblR");
      model.result().numerical("gloR").setResult();

      model.result().table().create("tblT", "Table");
      model.result().table("tblT").label("Tmax vs Compression");
      model.result().numerical("maxT").set("table", "tblT");
      model.result().numerical("maxT").setResult();

      first = false;
    } else {
      model.result().numerical("gloR").set("table", "tblR");
      model.result().numerical("gloR").appendResult();
      model.result().numerical("maxT").set("table", "tblT");
      model.result().numerical("maxT").appendResult();
    }

    // (Optional) Update a plot if you have one, e.g., "pg1"
    // model.result("pg1").run();

  } catch (Exception e) {
    // Continue even if one state fails
    debugLog("Error at state j = " + j + " : " + e.toString());
  }
}
```